The Pennsylvania State University
The Graduate School
Department of Electrical Engineering

ELECTRO-OPTICS AND NONLINEAR OPTICS OF LIQUID CRYSTAL-PLASMONIC MATERIALS AND STRUCTURES

A Dissertation in
Electrical Engineering

by

Yi Ma

Submitted in Partial Fulfillment
of the Requirements
for the Degree of

Doctor of Philosophy

May 2013

The dissertation of Yi Ma was reviewed and approved* by the following:

Iam-Choon Khoo
William E. Leonhard Professor of Electrical Engineering
Dissertation Advisor
Chair of Committee

Tim Kane
Professor of Electrical Engineering

Zhiwen Liu
Associate Professor of Electrical Engineering

Tom Mallouk
Evan Pugh Professor of Material Chemistry and Physics

Kultegin Aydin
Professor of Electrical Engineering
Head of the Department of Electrical Engineering

* Signatures are on file in the Graduate School

Abstract

The electro-optics and nonlinear optics effects of liquid crystals have already been intensively studied. Many people have invented a wide range of applications based on these properties, such as the liquid crystal display using the electro-optics effect, and the all-optical liquid crystal switching using the nonlinear optics effects. There continues to be interest in the liquid crystal research field.

Plasmonics is one of the research “hotspots” recently; especially in the last ten years. Basically, plasmonics or surface plasmon is a research field of sub-wavelength optics. It is always involved with nano-sized particles or structures. Theories about the surface plasmon polariton and localized surface plasmon resonance have been developed.

The combination of liquid crystal-plasmonic materials and structures has attracted my interest. The unique property of liquid crystal provides tunability to the plasmonic structures, while the near field electrical/optical field enhancement produced by nanoparticles influences the liquid crystal composite. In this dissertation, by using the required knowledge and concepts, the interaction effects between liquid crystal and plasmonics are discussed. Certain useful application designs and future work are also proposed.

Chapters 2 and 3 contain the fundamental knowledge base of the dissertation. Chapter 4 is focused on the effect of nanoparticles on the liquid crystal and nonlinear liquid. The material of nano-sized metal particle dispersed liquid crystal with tunable refractive index is also introduced. In addition, the nonlinear absorption enhancement is also studied. Chapter 5 is about the liquid crystal-plasmonic nanostructures. Most of the content focuses on the tuning of the localized surface plasmon resonance peak position, and some other applications are mentioned as well. Chapter 6 contains the summary and a discussion of possible future work.

TABLE OF CONTENTS

LIST OF FIGURES vii

LIST OF TABLES xii

Chapter 1 Introduction 1

Chapter 2 Liquid Crystal Electro-Optics and Nonlinear Optics Properties 3

2.1 Liquid Crystal Phases 3

2.2 Optical Anisotropy 7

2.3 Liquid Crystal Electro-Optics 10

2.3.1 Overview 10

2.3.2 Freedericksz Transition Introduction 11

2.3.3 Field Induced Phase Shift 13

2.4 Basic Idea of Liquid Crystal Nonlinear Optics 15

Chapter 3 Fundamentals of Plasmonics 18

3.1 Historical Review of Surface Plasmon 18

3.2 Surface Plasmon Related Concepts and Physical Properties 21

3.2.1 Surface Plasmon Polariton 21

3.2.2 Localized Surface Plasmon Resonance 25

3.2.3 Geometric Resonance 35

3.3 Methods to Study Surface Plasmon 36

Chapter 4 Nanoparticle Dispersed Liquid Crystal or Nonlinear Liquid 40

4.1 Fundamental Concepts 40

4.1.1 Effective Medium Theory 40

4.1.2 Material Models 43

4.1.3 Electron-Free Path 46

4.2 Dispersion of Nanoparticles in Nematic Liquid Crystal 47

4.2.1 Model Selection 47

4.2.2 Solid Spheres 49

4.2.3 Coated Nanoshells 51
4.3 Dispersion of Nanoparticles in Nonlinear Liquid 54
4.4 Conclusion 62
Chapter 5 Liquid Crystal Modulated Surface Plasmon Effect 63
5.1 Introduction and Literature Review 63
5.2 FDTD Simulation of Silver Nanocuboid Pairs Embedded in Liquid Crystal 65
5.2.1 Two- Particle System Model 65
5.2.2 Description of the Method and Material Model 67
5.2.3 Results and Discussion 69
5.3 Liquid Crystal- SPP applications 79
5.4 Conclusion 89
Chapter 6 Future Work and Summary 90
6.1 Future Work 90
6.1.1 Nanoparticle + Nonlinear liquid 90
6.1.2 Further Notes about Geometric Resonance 91
6.2 Summary 92
Reference 93

LIST OF FIGURES

Figure 2.1: Nematic, Smectic and Cholesteric liquid crystals 4

Figure 2.2: BP I and BP II structures: Blue phase liquid crystals are structured by intersecting double twist cylinders. In BP I, the cylinders pack into a face-centered cubic structure (left), whilst in BP II, the cylinders pack into a simple cubic structure (right) 5

Figure 2.3: Platelet texture of the Blue Phase 6

Figure 2.4: The refractive index ellipsoid of a uniaxial liquid crystal phase with the optic axis parallel to the x axis. The refractive index n_o of the ordinary ray is independent of propagation. The refractive index n_e of the extraordinary ray is larger than n_o for a liquid crystalline material of positive birefringence 8

Figure 2.5: The dependence of the refractive indices n_o and n_e of the ordinary and extraordinary waves, respectively, on the temperature T for a typical nematic liquid crystal. n_i denotes as the refractive index of the isotropic phase. 9

Figure 2.6 Elastic distortions of a nematic liquid crystal: (a) splay (b) twist (c) bend 11

Figure 2.7: Director axis profile in a nematic liquid crystal cell at various external voltages above the transition voltage 14

Figure 3.1: Propagation wave and Evanescent wave 22

Figure 3.2: An incident wave EM wave onto the dielectric/metal surface 22

Figure 3.3: Radiation pattern of a dipole 27

Figure 3.4: (a) Real and imaginary part of silver dielectric constants as function of wavelength. (b) Extinction efficiency as obtained from quasistatic theory for a 30nm radius silver sphere (c) The extinction efficiency for a 60 nm radius sliver sphere. In b and c, the exact Mie theory result is also plotted. ... 30

Figure 3.5: Surface plasmon resonances of gold, silver and copper with a different radius of nanospheres 31

Figure 3.6: E-field near field enhancement calculation of a 5:1 ellipsoid in a vacuum based calculation at 775 nm. Plane chosen perpendicular to the k direction. 32

Figure 3.7: Extinction spectra of silver spheroids, the ratio of major to minor axis is, from left to right, r = 1, 3.33, 5, and 10 32

Figure 3.8: Plasmon resonances of a 120-nm-diameter silica core coated with varying thicknesses of a gold shell. As the size of the gold layer increases from 5 nm to 20 nm, the plasmon resonance is blue shifted.....33

Figure 3.9: Surface plasmon resonance peak position shifts of a nanoshell's resonance with surrounding medium's refractive indices varying from 1.00 to 1.63. 34

Figure 3.10: Surface plasmon resonance peak position shifts of a copper nanosphere. 34

Figure 3.11: Extinction efficiency spectra for a 400 nanosphere one dimensional array with different inter-particle spacing. The radius of the nanosphere is 50nm. 35

Figure 3.12: Extinction efficiency spectra from experimental result for a two-dimensional nano-spheroid array with different pitch/ inter-particle spacing. 36

Figure 3.13: Illustration of the Yee cell with the FDTD method 38

Figure 4.1: Coated spheres with surrounding medium liquid crystal 42

Figure 4.2: Comparison of the LD model and the BB model. Left: Real and imaginary parts of the optical dielectric function of Ag., the solid curve is the calculated value using the BB model,the dashed curve the LD model; Right: Real and imaginary parts of the optical dielectric function of Au., the solid curve is the calculated value using the BB model, the dashed curve the LD model. 45

Figure 4.3: Comparison of the models: Top two, permittivity of the host medium, $\varepsilon_{host} = 2.0$ nanoparticle: solid gold, filling fraction of the nanosphere is 0.25, using four different combinations: Curve (1): the BB model for gold and using the Clausius-Mossotti equation to calculate the effective permittivity. Curve (2): the BB model for gold and using the Maxell-Garnett mixing rule to calculate the effective permittivity. Curve (3): the LD model for gold and using the Clausius-Mossotti equation to calculate the effective permittivity. Curve (4): the LD model for gold and using the Maxell-Garnett mixing rule to calculate the effective permittivity. .47

Figure 4.4(a) Comparison of experimentally measured and theoretically calculated refractive indices of pure dodecane and gold nanoparticles dispersed in dodecane at a volume fraction of 1.0%. Solid line: calculated results using LD model for Au, a constant value of A=1.4; markers: experimental results 48

Figure 4.4(b) Comparison of theoretically calculated refractive indices between different models (LD and BB), configuration same as 4.4(a).....49

Figure 4.5: Calculation of the real (n) and imaginary (k) parts of the refractive index for 2nm radius gold nanoparticle dispersed in NLC, when relative permittivity ε_{host} varies between 2.0 and 4.0 in steps of 0.5. 50

Figure 4.6: Calculation of the real (n) and imaginary (k) parts of the refractive index for 2nm radius silver nanoparticle dispersed in NLC when relative permittivity ε_{host} varies between 2.0 and 4.0 in steps of 0.5. 50

Figure 4.7: Calculation of the real part (n) and the imaginary part (k) of the refractive index for silica-gold core-shell nanospheres dispersed in a NLC. The radius for the silica core is 10nm with a permittivity of 3.8, and the thickness for the shell (gold) is 5nm. The filling fraction is 0.25. The permittivity of the host medium (NLC) varies from 2.0 to 4.0 52

Figure 4.8: Calculation of the real part (n) and the imaginary part (k) of the refractive index for silica-silver core-shell nanospheres dispersed in a NLC. The radius for the silica core is 10nm with a permittivity of 3.8, and the thickness for the shell (silver) is 5nm. The filling fraction is 0.25. The permittivity of the host medium (NLC) varies from 2.0 to 4.0.....52

Figure 4.9: Absorbance spectrum of L34.....55

Figure 4.10: Pico-second z-scan experimental results of the real part of the L34's nonlinear refractive index. 56

Figure 4.11: Simulation and experimental results for effective nonlinear absorption coefficient. The experiments were done by 460nm 83 ps laser. Cell thickness: 0.1 mm; laser focused beam waist: 10 m; Au nano-spheres diameter: 4 nm. 57

Figure 4.12: 140fs z-scan experimental results of the real part of the L34's nonlinear refractive index. Different wavelengths were examined. 58

Figure 4.13: the analyzed result of effective nonlinear absorption coefficient for each wavelength from figure 4.12. 59

Figure 4.14: The new calculation result for effective nonlinear absorption coefficient for 10nm diameter silver nanoparticle in L34 based on the real experimental intrinsic TPA absorption coefficient value. Filling fraction is 0.5%. 60

Figure 4.15: The exponential curve fitted simulation result for: L34 (red line) , L34+ 2nm radius gold nanoparticle (green dotted line), L34+ 5nm radius gold nanoparticle (green line), L34+ 2nm radius silver nanoparticle (blue dotted line), and L34+ 5nm radius silver nanoparticle (blue line) with filling fraction 0.5%. 61

Figure 5.1: Illustration of a plasmonic nanocuboid pair embedded in nematic liquid crystal.....69

Figure 5.2: Spatial Distribution of the E-field near field enhancement of the nanocuboid pair.....69

Figure 5.3: Horizontal cut of the calculated E-field Enhancement factor along Z= 0 such that the value along the X axis (axis connecting the two nanocuboids) is displayed.....70

Figure 5.4: Change of the electrical field strength at the middle point of the gap due to the difference of the liquid crystal's thickness.....71

Figure 5.5 (a): Change of electrical field strength at the middle point of the gap due to the difference of the separation distance.....72

Figure 5.5 (b): Near field enhancement change due to the difference of the separation distance.....73

Figure 5.6: Exponential fit of the resonance peak position (Top) and the $\Delta\lambda$ (Bottom) vs. the separation distance of the nanocuboid pair.....74

Figure 5.7: Change of the electrical field strength at the middle point of the gap due to the difference of the aspect ratio.....75

Figure 5.8: Top, linear curve fit of the sensitivity change vs aspect ratio. Bottom, linear curve fit of the resonance peak position change vs aspect ratio.....76

Figure 5.9: Linear curve fit of the sensitivity change vs aspect ratio and change of size.....78

Figure 5.10: Field intensity plots for 1-groove, 1-slit device in the (Top) ON state and (Bottom) OFF state. The relative magnitude of the Poynting vector is shown against the two-dimensional geometry of the device.....80

Figure 5.11: Field intensity plots for 2-grooves, 1-slit device in the (Top) ON state and (Bottom) OFF state. The relative magnitude of the Poynting vector is shown against the two-dimensional geometry of the device.....81

Figure 5.12: Intensity contrast for 1-groove and 2-groove devices. The contrast of the 2-groove device is ~15 dB whereas the 1-groove device exhibits contrast of ~8.1 dB.....82

Figure 5.13: Schematic of light-driven tunable plasmonic absorber. Light-sensitive liquid crystals on top of the absorber can be modulated with light.....82

Figure 5.14: (a) FDTD-simulated results of the performance of the Liquid crystal-plasmonic absorber. Around 30 nm shift can be observed. (b) Measured absorption band shifts with the pumping light turning ON and OFF. (c) Zoom-in view of the left absorption dip. The shift is around 25 nm. (d) Zoom-in view of the second absorption dip. The shift is around 20 nm....83

Figure 5.15: Illustration of a one dimensional periodic array of gold nanoparticles embedded in a nematic liquid crystal.....84

Figure 5.16: FDTD calculation of a periodic array of gold nanoparticles embedded in LC. The radius of the nanoparticle R=50nm; inter-particle spacing d=520nm. 85

Figure 5.17: (a) Extinction spectra of the periodic arrays of gold nanoparticles embedded in LC. (b) The dots are GR wavelengths extracted from (a). The curves are the analytical models of the GR wavelengths. 87

Figure 5.18: FDTD calculation of a periodic array of silver nanoparticles embedded in LC. The radius of the nanoparticle R=50nm; inter-particle spacing d=520nm. 88

Figure 6.1: Laser parameters: λ= 532 nm, pulse duration: 1 ns; focused spot diameter: 0.5mm. Sample: 1 mm thick cell filled with 70 % linear transmission nm-Au doped L34 and toluene, pure toluene and L34. 90

LIST OF TABLES

Table 5-1: Effect of the thickness of LC on the LSPR resonance peak position and sensitivity 71

Table 5-2: Effect of the different seperation distance on the LSPR resonance peak position and sensitivity 73

Table 5-3: Effects of the different Aspect Ratios on the LSPR resonance peak position and sensitivity 77

Table 5-4: Effects of the different cross sections on the LSPR resonance peak position and sensitivity 77

Table 5-5: GR resonance peak position vs. Rotation degrees of liquid crystal 86

Chapter 1 Introduction

The surface plasmon resonance is a resonant interaction that is due to the collective oscillations of the electrons near the surface of metal nanoparticles interacting with light [1]. This has attracted much research interest in recent years, especially resulting from the ability to modify the nanostructure to the application of many fields, such as: nanophotonic devices [2], chemical and biological sensing [3,4], and so on. In a sub-wavelength metallic structure, the surface plasmon resonances can be excited, accompanied by the enhancement of the optical near field. This excited absorption peak has been extensively studied [5-7]. Many results show that the peak position of the resonance depends on the size and the shape of the metallic structure, and is also affected by the surrounding dielectric environment [8-11].

One of the most effective ways to manipulate the medium refractive index is to use an anisotropic medium, such as liquid crystal (LC), to be the surrounding medium. This is because their optical properties can be switched by the use of an applied external field, or by a “pump beam”, or even by the change of temperature [12].

It is believed that in 1888, Friedrich Reintzer [13] first observed that cholesteryl benzoate seems to have two different transition points when it changes from crystal into liquid. His discovery opened the door to a new type of material. This material, which has physical properties between solids and liquids, is a new phase of matter called liquid crystal nowadays. Liquid crystals are fluid. They flow as ordinary liquids, and their molecules lack positional order. But they are also like crystals, where the molecules strongly interact with each other and express a certain orientational order of arrangement in large scale. As a result, liquid crystal has anisotropy in electromagnetic and optical properties. This anisotropy of electrical properties is fundamental for liquid crystal’s electro-optical effects. Under the

influence of an external e-field, the liquid crystal molecules are aligned along a preferred direction, which is called the reorientation of the director axis. The optical properties of the liquid crystal medium are changed as a result of this reorientation effect.

Liquid crystals have uncountable industrial and every-day applications. The Liquid Crystal Displays (LCDs) are the most commonly used displays in laptops, cell-phones, and TVs. In addition to the wide application of liquid crystal's electro-optical property, in research, liquid crystals are also viewed as optically nonlinear materials. The nonlinear light scattering phenomenon in LC (especially nematic liquid crystal, or NLC) has been extensively studied over the last 20 years. [14] The mechanism of the nonlinear optical effect is usually characterized by the optical index change coefficient n_2 (n_2 is defined as $n_2 = \Delta n / I$, where I is the input optical intensity, and Δn is the optical induced index change due to I) [15, 16]. In this case, a larger effective birefringence of the index n corresponds to a larger nonlinear effect.

Thus, the interaction between the surface plasmon resonance effect and liquid crystal material has attracted many researchers' attention. On the one hand, the near field enhancement caused by the nanoparticles could have some interesting effects on liquid crystals. In this dissertation, I am going to deal with the dispersion of nanoparticles in nematic liquid crystals, which is an efficient way to realize a tunable optical meta-material. The material can respond from visible wavelengths to the far infrared. Basically, two kinds of effects are expected by this nanoparticle dispersed liquid crystal: the effect of the nanoparticles onto the effective refractive index of the bulk medium, and the modification of liquid crystal's nonlinearity.

On the other hand, the surface plasmon resonance peak position is monitored by changing the surrounding medium's refractive index, which is the modification of the optical director axis of the liquid crystal. To utilize this liquid crystal's electro-optics effect onto plasmonics, several application designs will be mentioned.

Chapter 2 Liquid Crystal Electro-Optics and Nonlinear Optics Properties

Beginning with an overview of the different phases of liquid crystal, a definition of the order parameter and liquid crystal's optical anisotropy will be introduced in order to better understand the electro-optical effect of liquid crystal. A brief introduction about liquid crystal nonlinear optics is also included toward the end of the chapter.

2.1 Liquid Crystal Phases

In general, one can define liquid crystals based on the physical parameters, which include three different types: lyotropic liquid crystal, polymeric liquid crystal and thermotropic liquid crystal. [17]

The most widely used is the thermotropic liquid crystals, which exhibit liquid crystalline phases as a function of temperature. In this class, the molecular structures are usually expressed as "rigid rods". Depending on the ordered structures on the large scale, there are three main types of thermotropic liquid crystals: nematic, smectic and cholesteric.

Nematic liquid crystal is a common type of liquid crystal which can be found inside the extensively used liquid crystal display. In general, nematic liquid crystal is directionally correlated; the molecules have a preferred alignment direction. They are centro-symmetric, which means that their physical properties are the same in the $+\hat{n}$ or $-\hat{n}$ directions. So, in most cases, people use only $\hat{n}$ to denote its director axis.

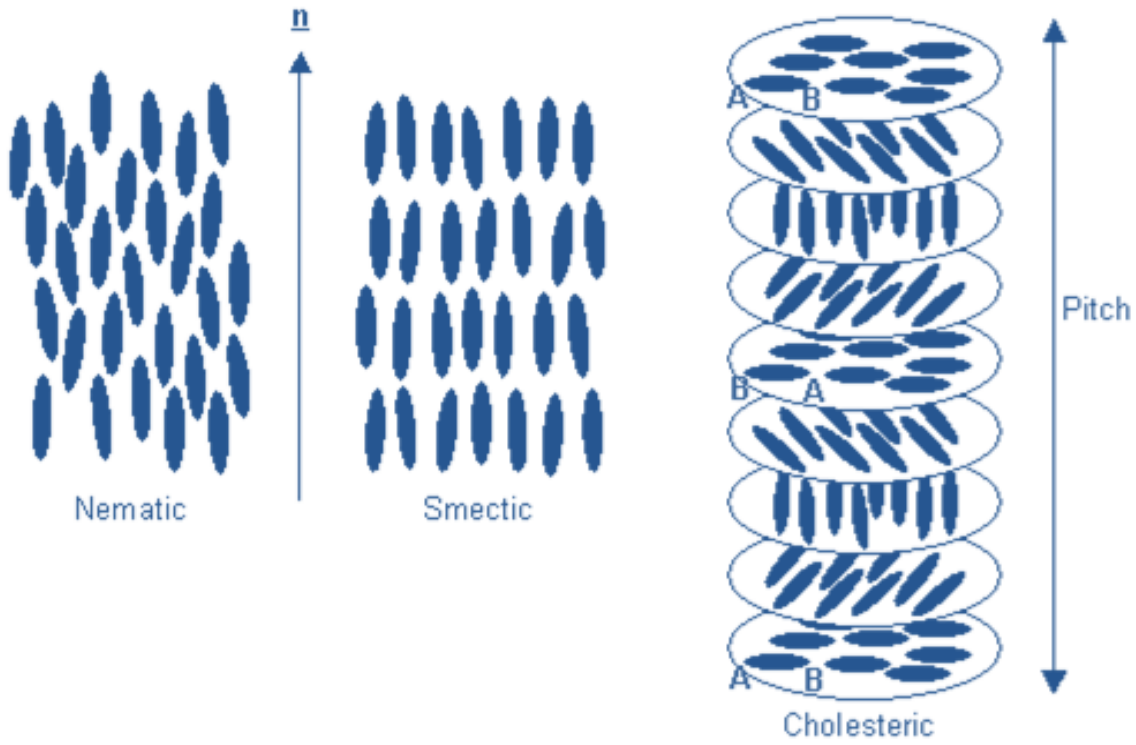

Figure 2.1: Nematic, Smectic and Cholesteric liquid crystals [18]

Smectic liquid crystals have positional order; their molecules are arranged in many different layers and create ordered patterns. Smectic liquid crystal has several sub-phases, e.g. smectic-A or smectic-C. From the thermotropic liquid crystal aspect, the sub-phases are different from the temperature scale. Usually, the smectic-C phase is located at a lower temperature than the smectic-A phase. Regarding the optics, the smectic-C's molecules form a certain angle with each layer's normal direction [18]. The smectic-A phase is more or less like the nematic one; uniaxial with the optical axis direction corresponding with the director axis direction [18].

Cholesteric liquid crystal was the first discovered liquid crystal type [13]. The molecules of cholesteric liquid crystals are chiral, so this phase sometimes is also called chiral liquid crystal or chiral nematic liquid crystal. As in figure (2.1), the director profile of the molecules shows a twisted configuration throughout the medium. Similar to the nematic liquid crystal, there are not layered structures of cholesteric liquid crystals. To define the length of the phase, people always use the

pitch, which is the distance for the director axis of the molecules to rotate through an angle of 2π. (Although in the figure, the molecules have A, B polar for better illustration. In fact, the cholesteric liquid crystals are non-polar. And the periodicity in this phase is actually only half of the pitch.) Like nematics, the cholesterics are uniaxial as well. Due to the special chiral configurations, this type of liquid crystal possesses a number of useful optical properties that are not found in other phases. Moreover, the cholesterics are photonic band gap materials [20, 21]. When the pitch length is of the same order of magnitude as the light's wavelength, selective reflection of the light will occur. Because of this, cholesteric liquid crystals are fundamental to the so-called liquid crystal laser [22, 23].

A special case of a high chirality liquid crystal material is a three dimensional spiral, called "Blue Phase" liquid crystal. Blue Phases sit between the cholesteric phase and the isotropic liquid phase. They usually only exist over a narrow temperature range (e.g. a few degrees C). Inside the range, the Blue Phases (BP) can be further separated into three classes: BP I, BP II and BP III. They are not only different in temperature, but they also have different molecular structures. For example, the molecular structures of BP I and BP II are shown in Figure 2.2:

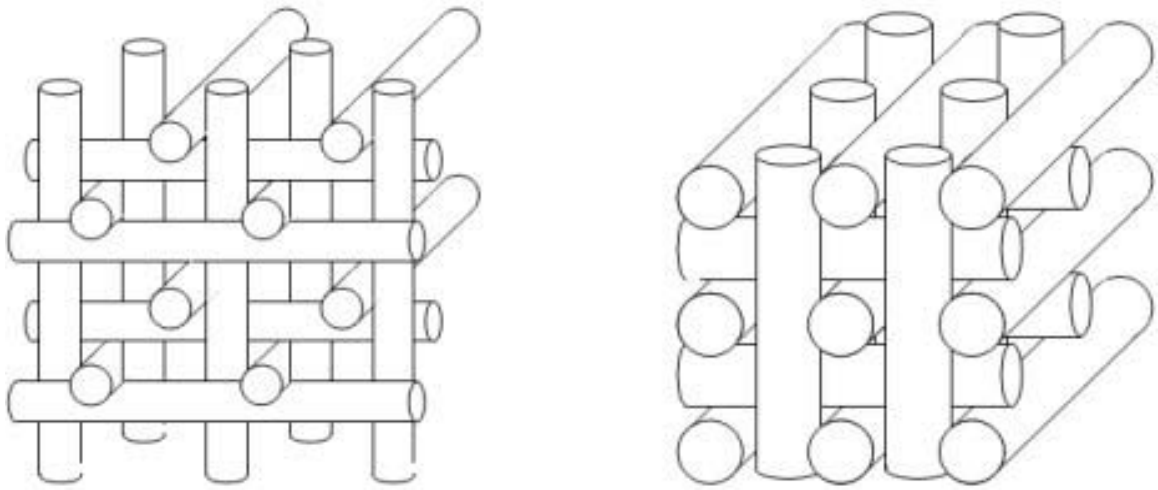

Figure 2.2: BP I and BP II structures: Blue phase liquid crystals are structured by intersecting double twist cylinders. In BP I, the cylinders pack into a face-centered cubic structure (left), whilst in BP II, the cylinders pack into a simple cubic structure (right).[24]

Due to the selective reflection, even though they are called Blue Phases, different colors may be observed as well. Below is an example of Blue Phase textures viewed under a microscope:

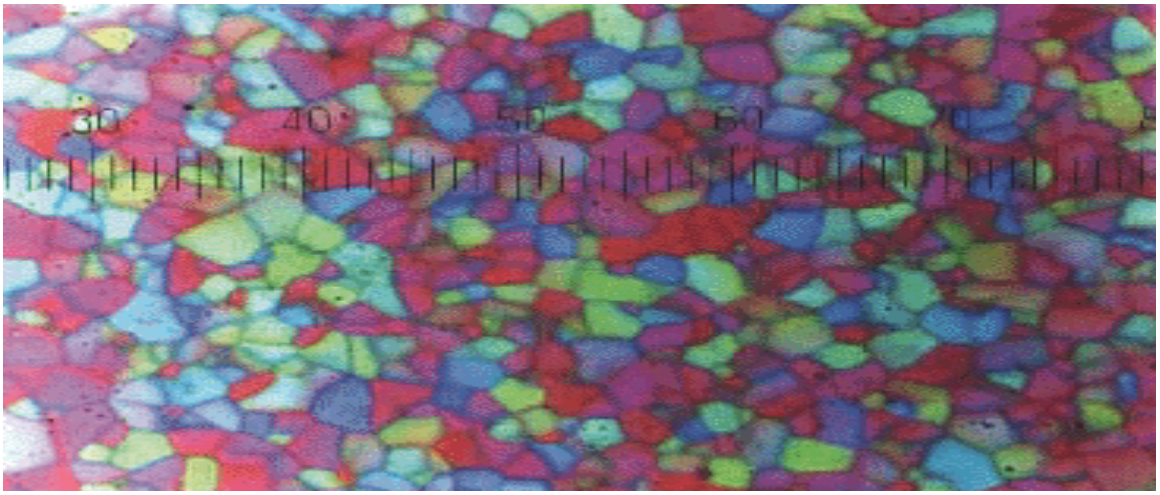

Figure 2.3: Platelet texture of the Blue Phase [25]

A theoretical way to characterize different phases of liquid crystals is to use the so-called Order Parameter. The definition of the order parameter is:

$$S = \frac{1}{2} < 3\cos^2\theta - 1 > \tag{2.1}$$

where θ is the angle between the axis of the molecular axis and the director axis, and the average<> is taken over the whole ensemble. [17]

This order parameter S is the parameter to characterize a long range orientation order and the random disposition of the centers of gravity individual liquid crystal molecule. [26] The value of S is usually from 0 to 1. When S=0, the liquid crystal is in the isotropic phase (liquid phase); S=1 corresponds to a perfect crystal. In other phases, e.g. nematic liquid crystals, the bulk material order parameter S is around 0.65 [27, 28].

2.2 Optical Anisotropy

Liquid crystal is a material with birefringence. Consider this uniaxial material in the molecular axis system with this form of refractive index:

$$n = \begin{pmatrix} n_{\perp} & 0 & 0 \\ 0 & n_{\perp} & 0 \\ 0 & 0 & n_{\parallel} \end{pmatrix} \tag{2.2}$$

There are two principle components: $n_{\perp}, n_{\parallel}$, and the optical anisotropy is $\Delta n = n_{\parallel} - n_{\perp}$. Here the parallel and perpendicular sign means that the molecular axis is parallel or perpendicular to the director axis. In most cases, $n_{\perp}$ is expressed as $n_{o,}$ and $n_{\parallel}$ as n_e, which correspond to the ordinary refractive index and extraordinary refractive index. In general, when an incident light comes into a birefringent medium such as liquid crystal, the electric vector can split into two mutually perpendicular components: ordinary (o) and extraordinary (e) waves. The o-wave is always perpendicular to the optic axis, so the refractive index displayed by the o-wave is ordinary refractive index $n_{o.}$ The electric field of the e-wave's propagation direction has an angle θ respective to the optic axis. From the refractive index ellipsoid, the refractive index of this extraordinary e-wave $n_e(\theta)$ is expressed as:

$$n_e(\theta)^2 = \left(\frac{\cos^2\theta}{n_o^2} + \frac{\sin^2\theta}{n_e^2}\right)^{-1} \tag{2.3}$$

The refractive index ellipsoid is shown in Figure 2.4.

In this case, the birefringence or the optical anisotropy of the medium, $\Delta n(\theta)$ in general case is defined as:

$$\Delta n(\theta) = n_e(\theta) - n_o \tag{2.4}$$

So, if the angle θ changes from 0 to 90 degrees, the optical anisotropy change continues from 0 to Δn.

Most nematic liquid crystals have positive birefringence ($\Delta n > 0$), which means that when passing through the material the extraordinary wave is delayed respective to the ordinary wave. An important thing to note is that the anisotropy Δn is a function of the temperature T, and this temperature variation is related to the order parameter change as a function of temperature S (T) [17].

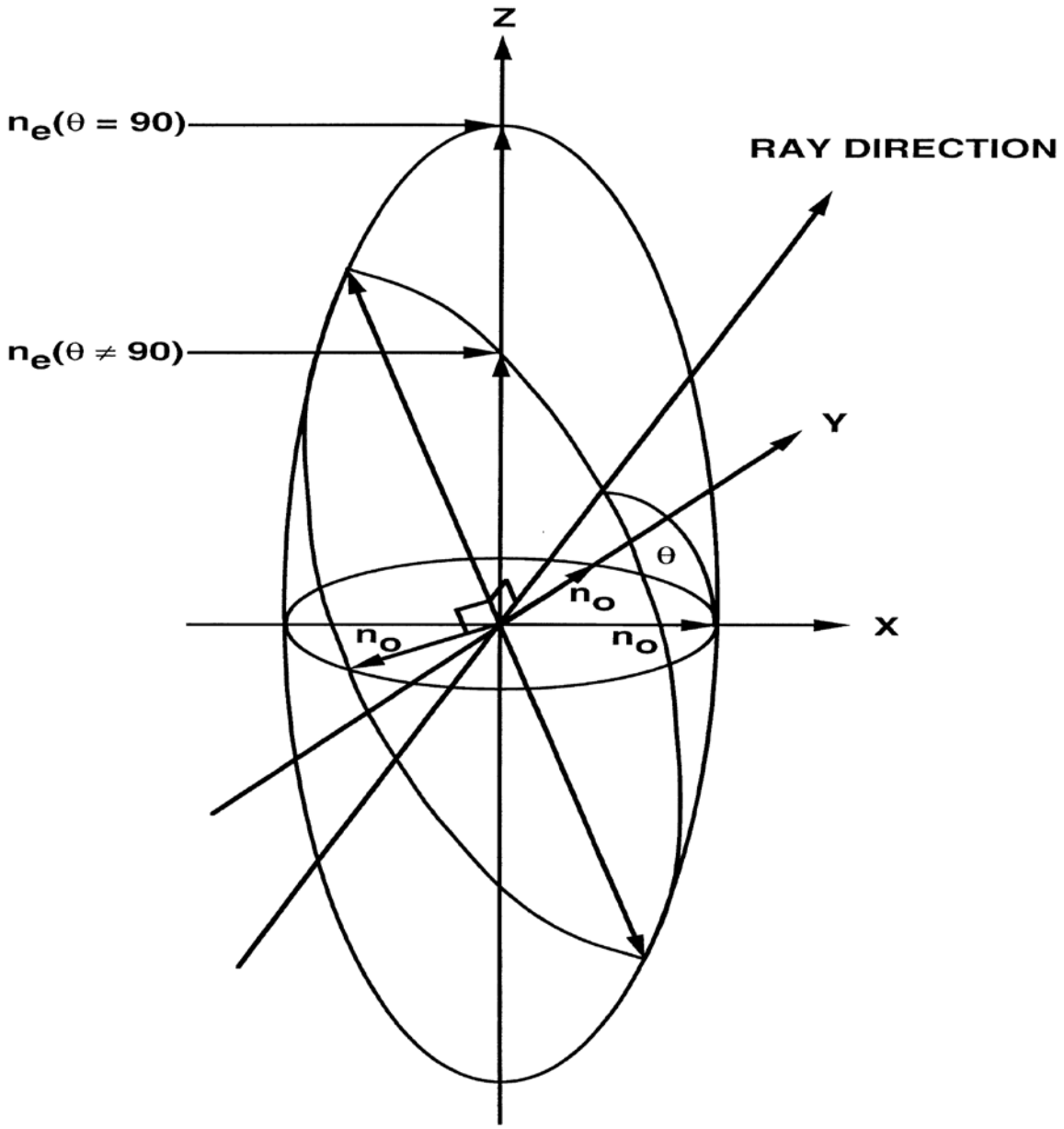

Figure 2.4: The refractive index ellipsoid of a uniaxial liquid crystal phase with the optic axis parallel to the x axis. The refractive index n_o of the ordinary ray is independent of propagation. The refractive index n_e of the extraordinary ray is larger than n_o for a liquid crystalline material of positive birefringence.[29]

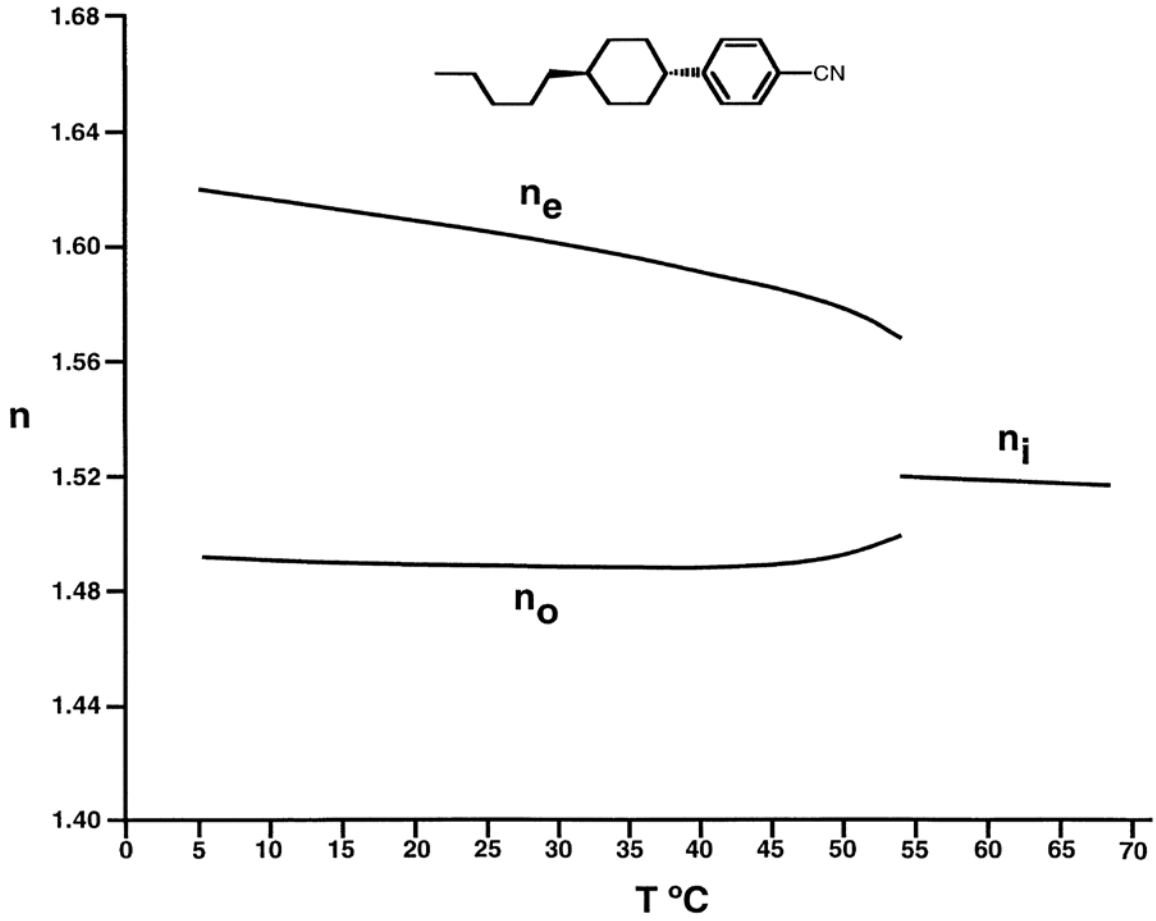

Figure 2.5: The dependence of the refractive indices n_o and n_e of the ordinary and extraordinary waves, respectively, on the temperature T for a typical nematic liquid crystal. n_i denotes as the refractive index of the isotropic phase. [29]

In figure 2.5 the nematic liquid crystal's permittivity is changed from about 2 to 4, which is the typical range of the liquid crystal permittivity's birefringence. In this figure, the $\Delta\varepsilon$ is approximately 2; but after some chemical compound replacement, this $\Delta\varepsilon$ may be around 5~10. [30]

Similarly, by suitable chemical compound replacement, it is possible to obtain a nematic liquid crystal with negative birefringence, which is called negative liquid crystal. Negative liquid crystals are commonly used in the vertical alignment (VA) technique for the liquid crystal display (LCD) industry. Compared to the positive liquid crystal, the birefringence of the negative liquid crystal is lower. When the birefringence is increased, the viscosity of this liquid will also increase unfavorably

[30].

Dual frequency liquid crystal (DFLC) is a unique type of liquid crystal. This kind of liquid crystal has positive permittivity anisotropy at low frequency. When an electrical field is applied onto the DFLC with high frequency, the anisotropy will change to negative [17]. The frequency when $\Delta\varepsilon$ =0 is called crossover frequency. In practical manufacturing, the DFLC is a mixture composed of positive and negative anisotropy liquid crystal compounds, [30] and its crossover frequency is around a few kilohertz, which depends on the molecular structures and compositions.

2.3 Liquid Crystal Electro-Optics

2.3.1 Overview

It is known that an external electric field can be used to change the orientational order of liquid crystal molecules. Thus, the change of the orientational order of the molecule, or the angle between the molecule axis and the director axis, will result in a change of the refractive index anisotropy according to the equation (2.4). This is the basic idea of the electro-optical property of liquid crystal Kerr effect [31] (The nematic liquid crystal's e-o effect in which the reorientation of the molecule axis is a Kerr-like effect). In general, this electric field induced reorientation of the liquid crystals is called the Freedericksz Transition [32-34]. Basically, the material molecules tend to be at the state where the total free energy is at a minimum. So, when the permittivity anisotropy is positive, liquid crystal molecules are preferred to align along the direction of the applied external electric field; when the permittivity anisotropy is negative, liquid crystal molecules tend to align perpendicular to the direction of the applied external electric field. Especially for DFLC, the two alignment states can be switched by the external electric field's frequency.

2.3.2 Freedericksz Transition Introduction

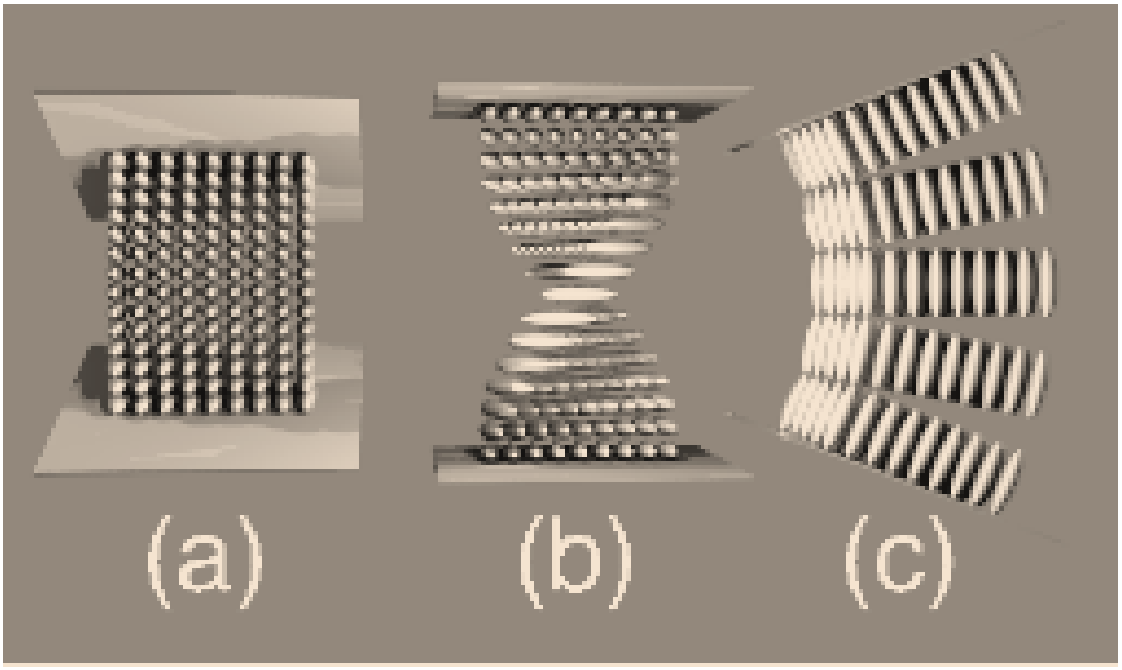

Figure 2.6 Elastic distortions of a nematic liquid crystal: (a) splay (b) twist (c) bend [35]

As shown in Fig.2.6, a nematic liquid crystal cell has three typical deformation structures: Splay, Twist and Bend. Considering the elastic constant of every form, strictly speaking, only the twist deformation involves the elastic constant $K_{22,}$ whereas the other two (splay and bend) involve the combination of K_{11} and K_{33}. Pure splay and bend deformations only occur for small reorientation [17].

Now, consider each case separately for the Freedericksz Transition condition. More detailed derivation of the equations can be found at ref. 30.

Case 1, Splay:

When θ is small, the elastic free energy density of the splay deformation is given by: [30]

$$f_1 = \frac{1}{2}(K_{11}\cos^2\theta + K_{33}\sin^2\theta)\theta' - \frac{1}{2}\varepsilon_0\Delta\varepsilon E^2\sin^2\theta \qquad (2.5)$$

Using the Euler-Lagrange method to minimize free energy:

$$-\varepsilon_0 \Delta\varepsilon E^2 \sin\theta\cos\theta - (K_{33} - K_{11})\sin\theta\cos\theta\theta'^2 - (K_{11}\cos^2\theta + K_{33}\sin^2\theta)\theta'' = 0 \quad (2.6)$$

Since θ is small, then $\sin\theta = \theta$, $\cos\theta = 1$. Neglecting second order terms, then:

$$-\varepsilon_0 \Delta\varepsilon E^2 \theta - K_{11}\theta'' = 0 \quad (2.7)$$

Furthermore, consider the boundary conditions, and set the cell thickness to be h, then there is an electric field threshold E_f which is given as:

$$E_f = \frac{\pi}{h}\sqrt{\frac{K_{11}}{\varepsilon_0 \Delta\varepsilon}} \quad (2.8)$$

Thus, the threshold voltage is:

$$V_f = hE_f = \pi\sqrt{\frac{K_{11}}{\varepsilon_0 \Delta\varepsilon}} \quad (2.9)$$

The voltage is independent of the cell thickness. This is the so-called Freedericksz transition voltage. For an external electric field voltage lower than the transition threshold voltage, the electric energy cannot compensate the elastic energy. In that case, the free energy of the distorted state is positive and therefore the transition will not occur. When applied voltage is higher than the threshold, the free energy of the system decreases and the transition happens. Further, when the external voltage is much higher than the transition voltage, then the change of the angle θ is not small. Set the maximum tilt angle at the middle to be θ_m, then: (assume $K_{11}=K_{33}$) [30]

$$\sin\theta_m \approx 2\sqrt{(E - E_f)/E_f} \quad (2.10)$$

Case 2, Bend:

When θ is small, the elastic free energy density of the bend deformation is shown as: [30]

$$f_2 = \frac{1}{2}(K_{11}\sin^2\theta + K_{33}\cos^2\theta)\theta' - \frac{1}{2}\varepsilon_0 \Delta\varepsilon E^2 \sin^2\theta \quad (2.11)$$

Similar to Case 1, the Freedericksz transition threshold is:

$$E_f = \frac{\pi}{h}\sqrt{\frac{K_{33}}{\varepsilon_0 \Delta\varepsilon}} \tag{2.12}$$

Case 3, Twist:

When θ is small, the elastic free energy density of the twist deformation is found as: [30]

$$f_3 = \frac{1}{2}K_{22}\theta'^2 - \frac{1}{2}\varepsilon_0 \Delta\varepsilon E^2 \sin^2\theta \tag{2.13}$$

Finally, the Freedericksz transition threshold of the twist case is given by:

$$E_f = \frac{\pi}{h}\sqrt{\frac{K_{22}}{\varepsilon_0 \Delta\varepsilon}} \tag{2.14}$$

Notice: although the deformation structures are different for the three cases, if one considers the one elastic constant approximation [17] and lets the three elastic constants $K_{11}=K_{22}=K_{33}=K$, then the Freedericksz transition voltage threshold could be given by the same form:

$$V_f = \pi\sqrt{\frac{K}{\varepsilon_0 \Delta\varepsilon}} \tag{2.15}$$

2.3.3 Field Induced Phase Shift

Following the previous discussions, when an external electric field voltage is higher than the transition threshold, the nematic liquid crystal molecules will be induced to have a reorientation of the director axis. As shown in Figure 2.7, the maximum orientation angle will occur at the center of the cell.

Thus, a polarized incoming extraordinary wave going through the liquid crystal cell will experience an extraordinary refractive index and phase shifts. The refractive index can be calculated using the equation (2.3). And the phase shift is given by: [17]

$$\Delta\phi = \int_0^h \frac{2\pi}{\lambda}(n_e(\theta) - n_0)dz \tag{2.16}$$

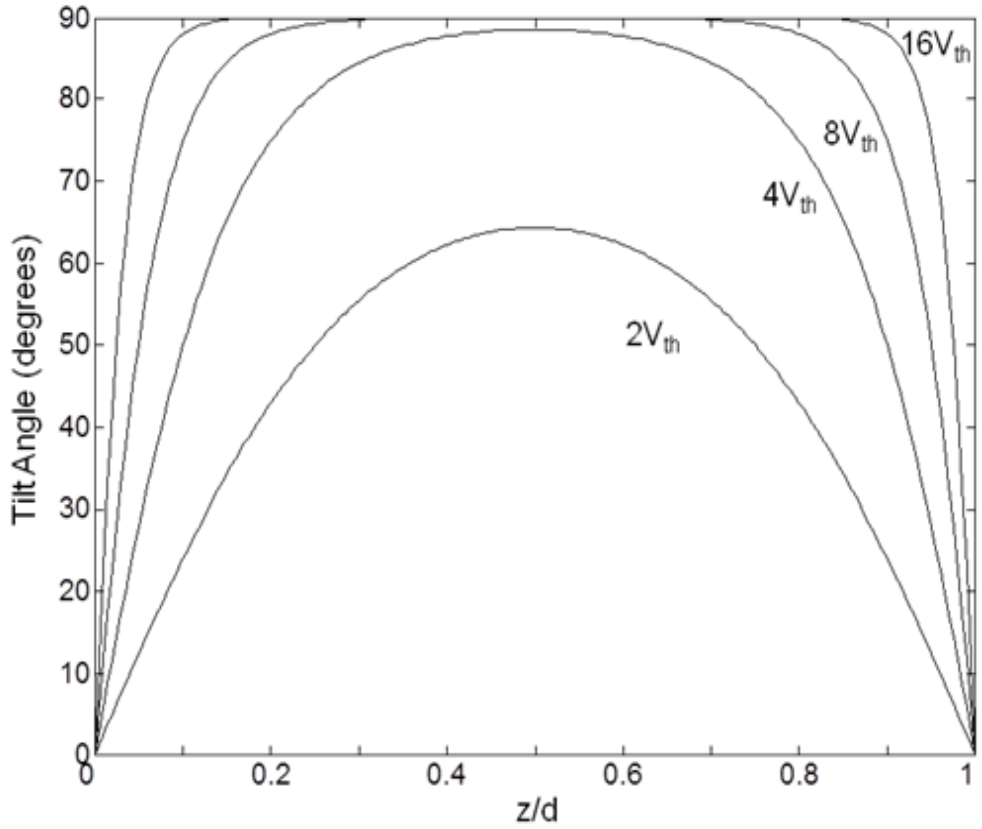

Figure 2.7: Director axis profile in a nematic liquid crystal cell at various external voltages above the transition voltage.[17]

To simplify, the hard boundary condition is employed, which means that at the boundary surfaces $\theta = 0$. Then the angle between the two boundary surfaces can be approximated as: [17]

$$\theta = \theta_0 \sin(\frac{\pi z}{h}) \tag{2.17}$$

However, in actual device applications the phase shift has to be calculated by quantitative numerical simulations. Some liquid crystal modeling software is available online. [36]

2.4 Basic Idea of Liquid Crystal Nonlinear Optics

Nonlinear optics is a branch of optics with about 50 years of history. Typically, before the invention of lasers, the light intensity is insufficient to modify the optical properties of any material. The discovery of the second-harmonic generation in 1961 is the first work in the field of nonlinear optics. [37] In the following 50 years, nonlinear optics became one of the hottest research fields to draw great attention [38-45].

Extremely nonlinear optical responses are found in nematic liquid crystals [42, 46-59]. Compared to other solid crystals, liquid crystal has one of the smallest elastic constants and the largest optical birefringence. These properties make liquid crystal a natural nonlinear optical material. Moreover, the nonlinearity can be further enhanced by doping some dyes or nanoparticles [52, 54, 55, 57]. As this dissertation is not focused on any specific nonlinear optical effect in liquid crystal, a general overview of nonlinear optics will be introduced in the following paragraphs. More detailed expressions of the nonlinear optical phenomena in liquid crystal are described in ref. 17 or 42.

The total polarization equation is:

$$P = P_L + P_{NL}\,. \tag{2.18}$$

Here, P_L is the linear polarization and P_{NL} is the nonlinear polarization. The wave equation in nonlinear optical mediums has the form: [17]

$$\nabla^2 E - \mu\varepsilon \frac{\partial^2 E}{\partial t^2} = \mu_0 \frac{\partial^2 P_{NL}}{\partial t^2} \tag{2.19}$$

From here, one can derive the very basic function in nonlinear optics, which is the intensity-dependent refractive index function as shown below: [17, 60]

$$n = n_0 + n_2 I \tag{2.20}$$

n_0 is the linear refractive index and n_2 is the nonlinear refractive index. So $n_2 = \frac{n - n_0}{I} = \frac{\Delta n}{I}$, which means that the nonlinear refractive index is proportional to the intensity induced optical anisotropy.

Next, consider the intensity propagation function, which is: [60]

$$\frac{dI}{dz} = -\alpha I - \beta I^2 \tag{2.21}$$

α is the linear absorption coefficient and β is the nonlinear absorption coefficient for two photon absorption. The higher order of nonlinear absorption, which includes three photon absorption or more, is ignored.

In order to get the relationship between the nonlinear absorption coefficient β and the nonlinear refractive index, the complex form of the refractive index should be used. So let $n = n'' + in''$ and $n_2 = n_2' + in_2''$, then from ref. 61, the complete expressions of the nonlinear refractive index and absorption as a function of third-order susceptibility are calculated: ($\chi^{(3)} = \chi_R^{(3)} + i\chi_I^{(3)}$)

$$n_2' = \frac{3}{4\varepsilon_0 c(n_0'^2 + n_0''^2)}(\chi_R^{(3)} + \frac{n_0''}{n_0'}\chi_I^{(3)}) \tag{2.22}$$

$$n_2'' = \frac{3}{4\varepsilon_0 c(n_0'^2 + n_0''^2)}(\chi_I^{(3)} - \frac{n_0''}{n_0'}\chi_R^{(3)}) \tag{2.23}$$

$$\beta = \frac{3\pi}{\lambda\varepsilon_0 c(n_0'^2 + n_0''^2)}(\chi_R^{(3)} + \frac{n_0''}{n_0'}\chi_I^{(3)}) \tag{2.24}$$

Notice, in liquid crystals, two photon absorption is the dominating nonlinear effect. So in this dissertation, the nonlinear optical effect in liquid crystal refers as third-order susceptibility $\chi^{(3)}$ effect. Furthermore, from equation (2.22) and (2.24):

$$\beta = \frac{4\pi}{\lambda} n_2'' \tag{2.25}$$

As a result, nonlinear absorption is proportional to the imaginary part of the

nonlinear refractive index. This expression has the same format as the linear absorption relationship where the linear absorption coefficient is shown as:

$$\alpha = \frac{4\pi}{\lambda} n_0'' \tag{2.26}$$

If a nonlinear optical medium has a very small, negligible linear absorption, then from equation (2.22) to (2.24) one can easily see that the real part of the nonlinear refractive index is proportional to the real part of the third-order susceptibility, and the nonlinear absorption coefficient is also proportional to the imaginary part of the third-order susceptibility.

To deal with the nonlinear optic effects in later chapters, I will focus on the changing of the nonlinear absorption coefficient β. This is the base of any $\chi^{(3)}$ nonlinear optic effect in liquid crystals.

Chapter 3 Fundamentals of Plasmonics

Surface plasmon optics is an important field under nano-optics. It is a research field about the optical properties of metal / dielectric interfaces or nano-sized metal particles. As mentioned in chapter 1, the surface plasmon effect is generated by the coupling between incident light and the collective oscillations of the electrons in metal. Because the generated electromagnetic field is in the scale of sub-wavelength, this effect breaks the diffraction limit and gives a very promising future to many surface plasmon based applications.

In this chapter the history and milestones of surface plasmon research is reviewed, which gives an overview of this field. Some important concepts, such as surface plasmon polariton (SPP), localized surface plasmon resonance (LSPR), and geometric resonance (GR) are defined. Following these, a brief introduction of certain theoretical research methods, e.g. the Mie scattering theory and the Finite-Difference Time-Domain (FDTD) simulation method are introduced.

3.1 Historical Review of Surface Plasmon

The surface plasmonic effect is sometimes called surface plasmon polariton or SPP. The concept of SPP is expressed as “a trapped surface mode which has electromagnetic fields decaying into both media but which, tied to the oscillatory surface charge density, and propagates along the surface” [62]. Basically, the SPP mentioned above is the original research concept, which is viewed as a propagation wave mode. Due to the development of nano technology, the surface plasmon excitation includes both the localized plasmon effect from metallic nanoparticles and the interface plasmon effect at metal/dielectric boundaries [63]. So for now, the SPP not only means the propagation wave but also includes the localized surface plasmon resonance (LSPR). In this dissertation, to be general, I use the concept of SPP to stand

for most of the surface plasmon effects. However, for the localized resonance caused by the nanoparticles, I use LSPR to specify this category. Some detailed explanations of both concepts are listed in section 3.2.

The famous Wood's anomalies [64] are often viewed as the starting point of SPP research, when Wood found an uneven distribution of light in the diffraction from metal gratings in 1902. Then in 1908, starting from the Maxwell equation, Mie [65] developed an analytical solution to the interaction problem between nanoparticles and incident light, which is the so-called Mie theory nowadays. This theory opens the possibility to quantitatively calculate a nano-sized small particle. Also, in 1907 and 1909, both Zenneck [66] and Sommerfeld [67] theoretically proved that there is a surface electromagnetic wave at radio frequency which occurs at the boundary of two mediums, when one of the mediums is a lossy medium (dielectric or metal) and the other one is a loss-free medium. Later, in 1941, Fano [68] was the first to explain the Wood's anomalies. He pointed out that the surface electromagnetic wave (the Sommerfeld wave) is responsible for the effect from metallic gratings. He suggested that surface electromagnetic waves are evanescent waves at the boundary of metal and air. This Sommerfeld wave, which occurs at the lossy dielectric –air interface, is at radio frequency, while the surface waves at the metal-air interface results in the optical frequency region. Fano also predicted that they "represent for media of different electrical properties the same singular case defined by the same mathematical equation". In 1957, Ritchie [69] was the first to theoretically demonstrate the existence of a surface plasma excitation at the surface of metal, i.e. surface plasmon. Meanwhile, Stern [70, 71] derived the mathematical equation that Fano pointed out; the dispersion relationship for surface electromagnetic waves at metal surfaces. Also around the same time, Powell and Swan [72] experimentally observed the excitation of the surface plasmon at the metal surface by using electrons to excite it. Then, in 1968, Otto [73] proposed the ATR (attenuated total reflection) method for prism coupling of bulk electromagnetic / optical waves onto surface electromagnetic waves. Based on Otto's design, in 1971, Kretschmann [74] further

modified the design and made it more practical. Nowadays, the Kretschmann configuration is the most commonly used geometry to excite the surface plasmon for any device applications.

The real breakthrough of surface plasmon photonic research is due to Thomas Ebbesen's work. In 1998, Ebbesen and his co-workers [75] observed an extraordinary optical transmission through an array of sub-wavelength holes. They explained that this effect was caused by the incident light and the surface plasmon. This is the first demonstration of the surface plasmon effect of sub-wavelength, which is believed to be the starting point of present SPP research. After that, the SPP related research dramatically increased over the past 10-15 years. Roughly, these studies can be divided into two categories. One is related to the synthesis of nanoparticles. By controlling the size, shape, and structure of metal nanoparticles, there is a way to tailor the plasmonic properties of these nanoparticles [76]. Further, researchers found a more efficient method which involves monitoring the surrounding medium. That is why the liquid crystal related nanophotonic research has been more recognized. The other category is surface plasmon related modern optical devices. For example, the first optical imaging below the diffraction limit was realized by Xiang Zhang's group in 2005 [77]. They called it the "Super Lens". This "lens" has a resolution of about only 60nm, which is 1/6 of the wavelength of light. Others, e.g. resonant optical antennas [78], channel SPP waveguide [79], hyper-lens magnifying of sub-diffraction limit objects [80], optical recording by surface plasmon resonance [81], core-shell nanostructure spaser- based nano laser [82], and nano-spaser based on hybrid waveguide [83] have been designed, demonstrated and developed. In all, to get the appropriate SPP effect or modification has become one of the most important factors of all the device applications. In this case, the tuning ability that liquid crystal provides to SPP related devices has created many useful ideas and designs. More work is expected in the future.

3.2 Surface Plasmon Related Concepts and Physical Properties

In the following section 3.2.1, I will begin with the general expression of surface plasmon polariton (SPP). Because SPP is the basis of surface plasmon, and the Mie theory is fundamental to localized surface plasmon resonance (LSPR), in section 3.2.2 the Mie theory and LSPR concept will be introduced. Section 3.2.3 includes a brief study of a special LSPR effect called geometric resonance (GR).

3.2.1. Surface Plasmon Polariton

To start with, the Drude model for metals should be introduced: [84]

$$\varepsilon_m(\omega) = \varepsilon_m(\infty)[1 - \frac{\omega_p^2}{\omega^2 + i\omega\gamma}] \tag{3.1}$$

Here the ω_p is the plasma frequency of the metal, and the coefficient γ is called the damping constant. Notice, compared with the standard free electron Drude model, an additional coefficient $\varepsilon_m(\infty)$ is in front. This is because for surface plasmon related effects, the electrons are mostly confined around the boundary of the two mediums.

Assume an incident wave with the form $E = E_0 e^{ik_z z + i\omega t}$. With the relationship $D = \varepsilon_m(\omega)E$ and the wave propagation equation $\frac{\partial^2 D}{\partial t^2} = c^2 \nabla^2 E$, the dispersion relationship for metals could be derived as:

$$\varepsilon(\infty)[\omega^2 - \omega_p^2] = ck_z^2 \tag{3.2}$$

k_z is the propagation constant for the propagation direction. When the propagation constant k_z only has the real part, $\omega^2 - \omega_p^2 > 0$, then $\varepsilon_m > 0$, the wave can propagate through the medium; when k_z is complex then $\omega^2 - \omega_p^2 < 0$, and $\varepsilon_m < 0$, the wave

cannot propagate through the medium; this wave is the so-called evanescent wave.

See figure 3.1 for an illustration from the reference:

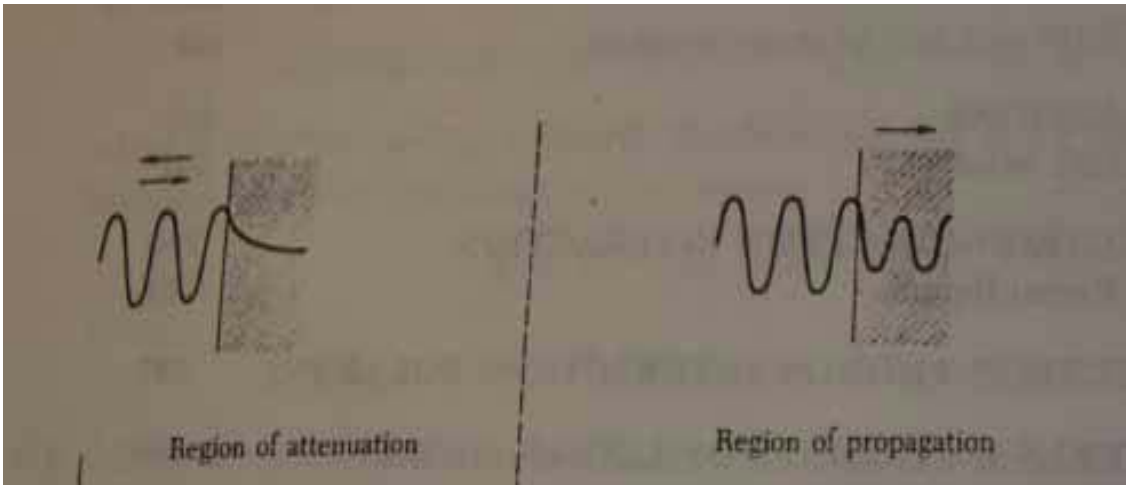

Figure 3.1: Propagation wave and Evanescent wave [84]

Based on this concept, the physical properties of the evanescent wave SPP can be concluded. As shown in Figure 3.2, consider an incident P-polarized electromagnetic (EM) wave that hits onto the boundary of dielectric and metal with the angle θ : (+y direction is off the paper)

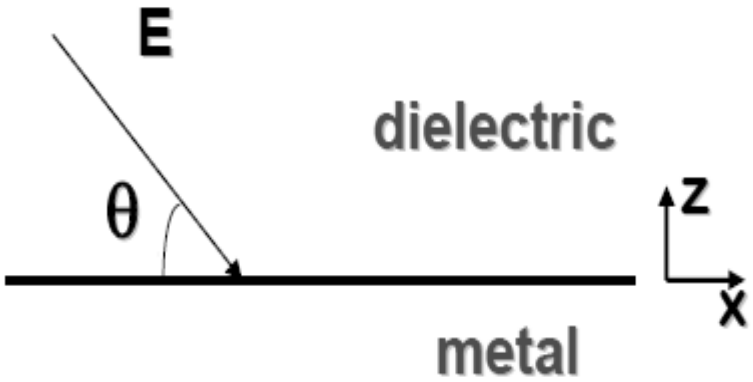

Figure 3.2: An incident wave EM wave onto the dielectric/metal surface

Assume that the permittivity of metal is ε_1 and the permittivity of dielectric

is ε_2 , then the electric field can be expressed as: [85,86]

For the region in the metal (z<0):

$$H_1 = (0, H_{y1}, 0)e^{i(k_{x1}x - k_{z1}z - \omega t)} \tag{3.3}$$

$$E_1 = (E_{x1}, 0, E_{z1})e^{i(k_{x1}x - k_{z1}z - \omega t)} \tag{3.4}$$

For the region in the dielectric (z>0):

$$H_2 = (0, H_{y2}, 0)e^{i(k_{x2}x + k_{z2}z - \omega t)} \tag{3.5}$$

$$E_2 = (E_{x2}, 0, E_{z2})e^{i(k_{x2}x + k_{z2}z - \omega t)} \tag{3.6}$$

Then from the Maxwell equations, it can be derived that:

$$k_{z1}H_{y1} = \frac{\omega}{c}\varepsilon_1 E_{x1}, k_{z2}H_{y2} = -\frac{\omega}{c}\varepsilon_2 E_{x2} \tag{3.7}$$

And from the continuous boundary condition,

$$k_{x1} = k_{x2} = k_x, \frac{k_{z1}}{\varepsilon_1} + \frac{k_{z2}}{\varepsilon_2} = 0 \tag{3.8}$$

Plus: the propagation function

$$\varepsilon_i(\frac{\omega}{c})^2 = k_x^2 + k_{zi}^2 \tag{3.9}$$

Finally, from Eq. (3.7) to (3.9), the dispersion relationship for the surface plasmon polariton wave is illustrated: [85]

$$k_x = \frac{\omega}{c}(\frac{\varepsilon_1\varepsilon_2}{\varepsilon_1 + \varepsilon_2})^{\frac{1}{2}} \tag{3.10}$$

To have the traveling wave of SPP at the surface, the real part of this propagation constant must be real, then $\varepsilon_1' < 0, \left|\varepsilon_1'\right| > \varepsilon_2$. This is the condition in order to have a SPP wave at the boundary. At the boundary of metal (e.g. silver or gold) and dielectric, these conditions are satisfied.

Besides the condition of the SPP wave, some other physical properties of SPP

are listed:

1. A SPP wave can only happen at the P-polarized incident wave. Follow the save derivation as the P-type, for any S-polarized EM wave there is no non-zero solution for the continuous boundary condition. So, an S-polarized incident wave cannot generate this SPP effect. See also Ref.87.

2. A SPP wave can only travel at the boundary. It is an evanescent wave in both the dielectric and metal. From the dispersion relationship, then: (assume $k_x = k_x' + ik_x''$)

$$k_x' = \frac{\omega}{c}\left(\frac{\varepsilon_1'\varepsilon_2}{\varepsilon_1' + \varepsilon_2}\right)^{\frac{1}{2}} \tag{3.11}$$

$$k_x'' = \frac{\omega}{c}\left(\frac{\varepsilon_1'\varepsilon_2}{\varepsilon_1' + \varepsilon_2}\right)^{\frac{3}{2}} \frac{\varepsilon_1''}{2(\varepsilon_1')^2} \tag{3.12}$$

Plug Eq. (3.11) and (3.12) into Eq. (3.9), then $k_{zi}^{\ 2} < 0$, i.e. evanescent wave.

3. The energy of the SPP wave is confined around the boundary. The skin depth is defined as $z = 1/k_{zi}$. Some sample numbers for the skin depth: at wavelength 600nm, for silver, the skin depth into the dielectric is 390nm, and the skin depth into the metal is 24nm; while for gold, these numbers change to 280nm and 31nm. At the boundary, the energy can travel as a traveling wave with a distance of $L_{SP} = 2\,\mathrm{Im}(k_{sp})$, e.g. for silver, when $\lambda = 514.5nm$, $L_{sp} = 22.5\mu m$.

3.2.2. Localized Surface Plasmon Resonance

Localized surface plasmon resonances are excited when accompanied by the enhancement of an electrical/optical near field. Before exploring more details about LSPR, first, the famous Mie theory [65] needs to be introduced.

Generally, for electromagnetic field propagation problems, the wave functions often have these forms:

$$\nabla^2 E + k^2 E = 0 \tag{3.13}$$

$$\nabla^2 H + k^2 H = 0 \tag{3.14}$$

The main idea of the Mie scattering theory is that, assuming a scalar Ψ and a random vector c, there is a vector M which $M = \nabla \times (c\Psi)$ to fit $\nabla \bullet M = 0$. Thus,

$$\nabla^2 M + k^2 M = \nabla \times [c(\nabla^2 \Psi + k^2 \Psi)] \tag{3.15}$$

Apparently, in order for this function to have the form of Eq. (3.13) it is required that $\nabla^2 \Psi + k^2 \Psi = 0$. Similarly, besides the vector M, there is another vector N where $N = \frac{\nabla \times M}{k}$. Then, $\nabla^2 N + k^2 N = 0$ and $\nabla \bullet N = 0$. So, any property of the EM field related to functions (3.13) and (3.14) is transformed into a problem to solve this equation:

$$\nabla^2 \Psi + k^2 \Psi = 0 \tag{3.16}$$

Under a spherical coordinate system and using the separate variable method: assume a solution that $\Psi(r, \theta, \phi) = R(r)\Theta(\theta)\Phi(\phi)$, then:

$$\frac{d^2 \Phi}{d\phi^2} + m^2 \Phi = 0 \tag{3.17}$$

$$\frac{1}{\sin\theta} \frac{d}{d\theta} (\sin\theta \frac{d\Theta}{d\theta}) + [n(n+1) - \frac{m^2}{\sin^2 \theta}]\Theta = 0 \tag{3.18}$$

$$\frac{d}{dr}(r^2\frac{dR}{dr})+[k^2r^2-n(n+1)]R=0 \tag{3.19}$$

If these equations are solved individually, then a standard set of solutions are achieved as:

$$\psi_{emn}=\cos m\phi P_n^m(\cos\theta)z_n(kr) \tag{3.20}$$

$$\psi_{omn}=\sin m\phi P_n^m(\cos\theta)z_n(kr) \tag{3.21}$$

The $P_n^m(\cos\theta)$ is the associated Legendre polynomials of the first kind and $z_n(kr)$ is standing for one of the Bessel functions: $j_n, y_n, h_n^{(1)}, h_n^{(2)}$. The first two are the Bessel functions of the first and second kinds, and the other two are the Hankel functions of the first and second kinds [5, 6].

Thus, the EM modes are given by:

$$M_{emn}=\nabla\times(r\psi_{emn}) \tag{3.22}$$

$$M_{omn}=\nabla\times(r\psi_{omn}) \tag{3.23}$$

$$N_{emn}=\frac{\nabla\times M_{emn}}{k} \tag{3.24}$$

$$N_{omn}=\frac{\nabla\times M_{omn}}{k} \tag{3.25}$$

Next, consider a small (e.g. nano-sized) sphere particle in the EM field. The incident E-field is given by:

$$E_i=E_0e^{ikr\cos\theta}\hat{e}_x \tag{3.26}$$

Use the vector M and N to expand it, then:

$$E_i=E_0\sum_{n=1}^{\infty}i^n\frac{2n+1}{n(n+1)}(M_{o1n}^{(1)}-iN_{e1n}^{(1)}) \tag{3.27}$$

Here the (1) means the Bessel function with the form of j_n.

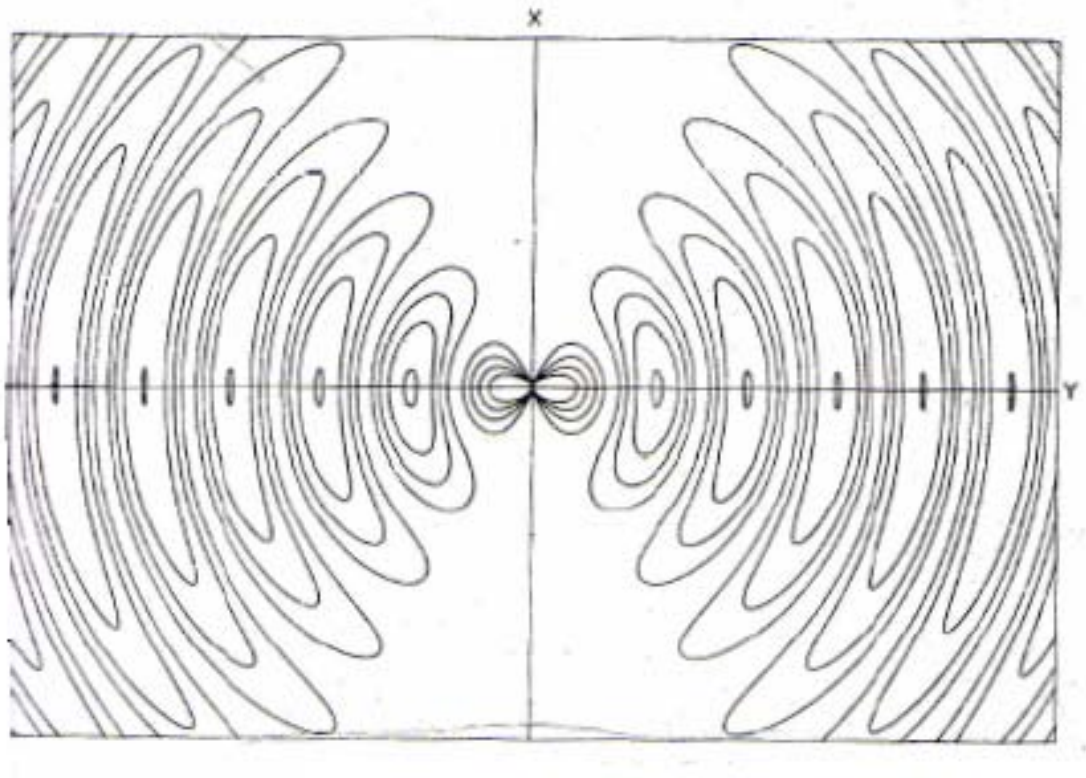

Figure 3.3: Radiation pattern of a dipole[5]

The corresponding magnetic field is given by:

$$H_i = \frac{-k_m}{\omega\mu_m} E_0 \sum_{n=1}^{\infty} i^n \frac{2n+1}{n(n+1)} (M_{e1n}^{(1)} + iN_{o1n}^{(1)}) \tag{3.28}$$

The electrical field radiation pattern is shown in figure 3.3.

Finally, with the consideration of the boundary conditions, a set of solutions from the sphere EM field problem, i.e. the Mie scattering problem [5], is obtained.

The EM field component inside the sphere:

$$E_1 = E_0 \sum_{n=1}^{\infty} i^n \frac{2n+1}{n(n+1)} (c_n M_{o1n}^{(1)} - id_n N_{e1n}^{(1)}) \tag{3.29}$$

$$H_1 = \frac{-k}{\omega\mu} E_0 \sum_{n=1}^{\infty} i^n \frac{2n+1}{n(n+1)} (d_n M_{e1n}^{(1)} + ic_n N_{o1n}^{(1)}) \tag{3.30}$$

The scattering EM field component (3) means Henkel function $h_n^{(1)}$

$$E_s = E_0 \sum_{n=1}^{\infty} i^n \frac{2n+1}{n(n+1)} (ia_n N_{e1n}^{(3)} - b_n M_{o1n}^{(3)}) \tag{3.31}$$

$$H_s = \frac{k_m}{\omega \mu_m} E_0 \sum_{n=1}^{\infty} i^n \frac{2n+1}{n(n+1)} (ib_n N_{o1n}^{(3)} + a_n M_{e1n}^{(3)}) \tag{3.32}$$

And the coefficients:

$$c_n = \frac{\mu_1 m \psi_n(x) \xi_n'(x) - \mu_1 m \xi_n(x) \psi_n'(x)}{\mu_1 \psi_n(mx) \xi_n'(x) - \mu m \xi_n(x) \psi_n'(mx)} \tag{3.33}$$

$$d_n = \frac{\mu_1 m \psi_n(x) \xi_n'(x) - \mu_1 m \xi_n(x) \psi_n'(x)}{\mu m \psi_n(mx) \xi_n'(x) - \mu_1 \xi_n(x) \psi_n'(mx)} \tag{3.34}$$

$$a_n = \frac{\mu m \psi_n(mx) \psi_n'(x) - \mu_1 \psi_n(x) \psi_n'(mx)}{\mu m \psi_n(mx) \xi_n'(x) - \mu_1 \xi_n(x) \psi_n'(mx)} \tag{3.35}$$

$$b_n = \frac{\mu_1 \psi_n(mx) \psi_n'(x) - \mu m \psi_n(x) \psi_n'(mx)}{\mu_1 \psi_n(mx) \xi_n'(x) - \mu m \xi_n(x) \psi_n'(mx)} \tag{3.36}$$

with $m = n / n_m$, $x = \frac{2\pi n_m}{\lambda} R$ (R: radius of the sphere), $\psi_n(x) = x j_n(x)$, $\xi_n(x) = x h_n^{(1)}(x)$, μ_1 permeability of the sphere, and μ permeability outside.

A more detailed derivation of the Mie theory, including all the boundary conditions, can be found in Ref. 5. Equipped with this theory, one is able to calculate the localized surface plasmon resonances of metallic nanospheres.

As mentioned before, the size, shape and structure of metal nanoparticles and the refractive index of the surrounding medium can be used to tailor plasmonic properties. In the following paragraphs, the influence of each factor is discussed separately.

Influence of Size:

Quasistatic theory is often used for the LSPR effect of nanospheres. Because the coefficient a_n and b_n are proportional to $(kR)^{2n+1}$, then when R<<λ only the n=1 term, which is the dipole plasmon resonance term, will be considered. In this case, the

extinction cross-section is defined as: [6] (let $\varepsilon = \varepsilon_1 + i\varepsilon_2$)

$$\sigma_{ext}(\omega) = 9\frac{\omega}{c}\varepsilon_m^{3/2}\frac{4\pi}{3}R^3\frac{\varepsilon_2(\omega)}{[\varepsilon_1(\omega)+2\varepsilon_m]^2+\varepsilon_2^2(\omega)} \tag{3.37}$$

Clearly, the surface plasmon resonance peak is at the position when $\varepsilon_1 = -2\varepsilon_m$

This position is not related to the size of the nanosphere. But in fact, when the radius of the nanoparticle is larger than 30nm, not only the dipole plasmon resonance term but also the quadrupole plasmon resonances should be considered [9]. See figure 3.4 for an illustration, and ref. 9 for a detailed derivation and physics interpretation.

Approximation: when only considering the dipole resonance term, as the radius increases, the LSPR peak position will be red shifted. See Figure 3.5 for the results of gold, silver and copper nanoparticles [6].

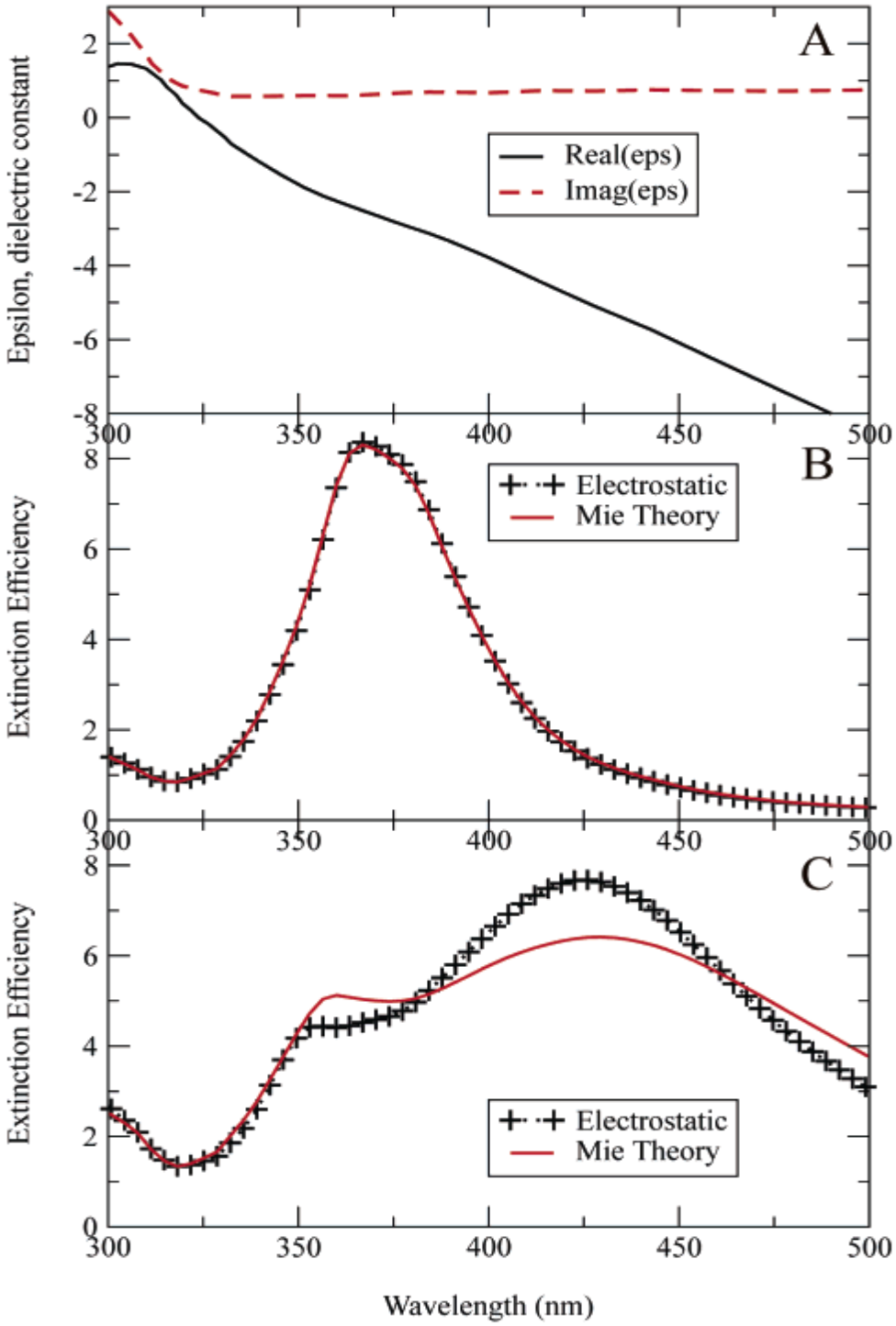

Figure 3.4: (a) Real and imaginary part of silver dielectric constants as function of wavelength. (b) Extinction efficiency as obtained from quasistatic theory for a 30nm radius silver sphere (c) The extinction efficiency for a 60 nm radius sliver sphere. In b and c, the exact Mie theory result is also plotted. [9]

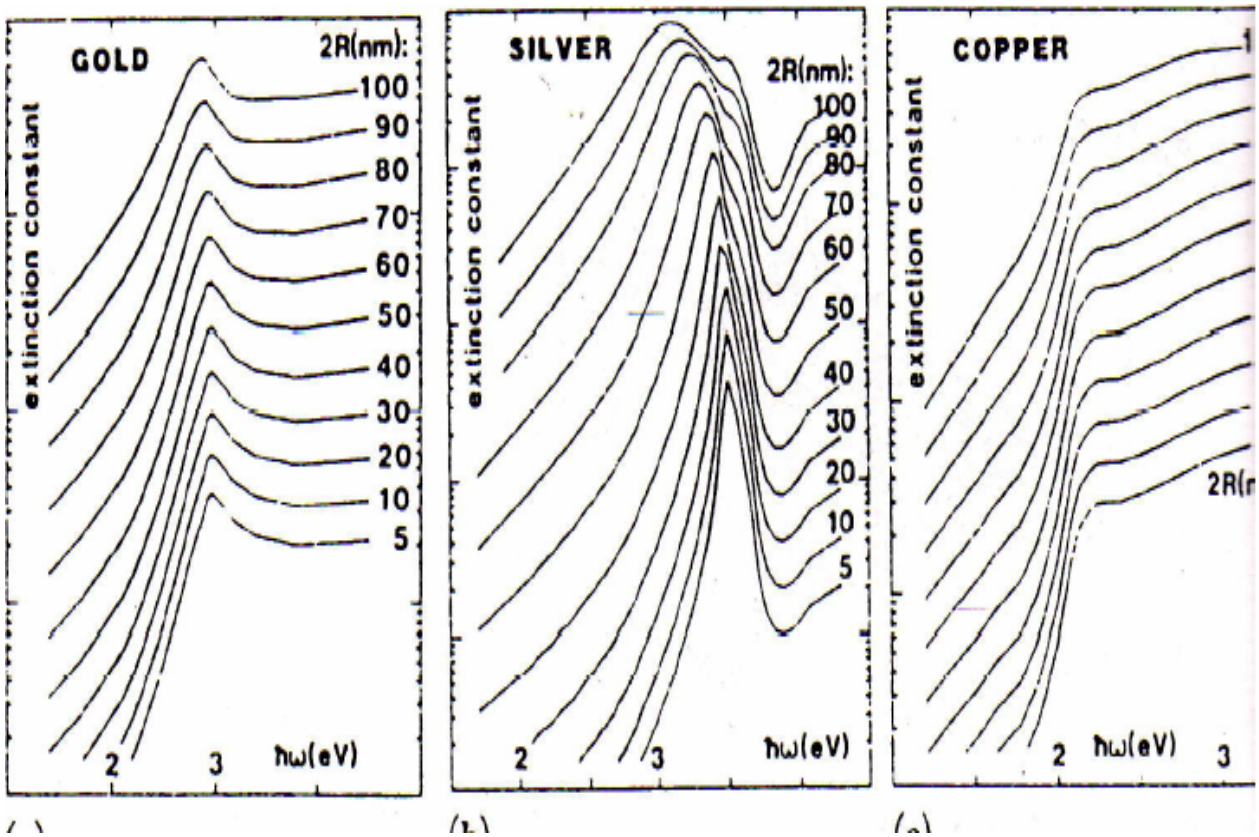

Figure 3.5: Surface plasmon resonances of gold, silver and copper with a different radius of nanospheres[6]

Influence of shape:

Changing the shape or structure of the nanoparticle will have some impact on the localized surface plasmon resonance's peak position as well. For example, with a silver spheroid nanoparticle [9], the electric near field enhancement is simulated as shown in Figure. 3.6. The result of the extinction efficiency of different spheroids is compared in Figure 3.7. The sizes of these spheroids are similar to a 30nm radius nanosphere. They differ in aspect ratio, which is the ratio between the length of the long axis and the length of the short axis. From fig.3.7, clearly, as the aspect ratio is increased, the peak position of the LSPR is red-shifted.

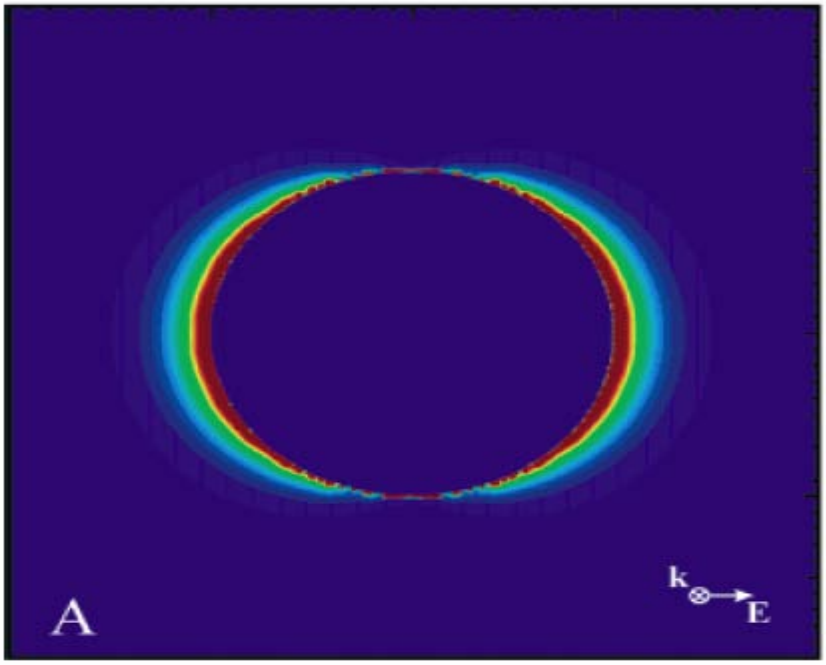

Figure 3.6: E-field near field enhancement calculation of a 5:1 ellipsoid in a vacuum based calculation at 775 nm. Plane chosen perpendicular to the k direction.[9]

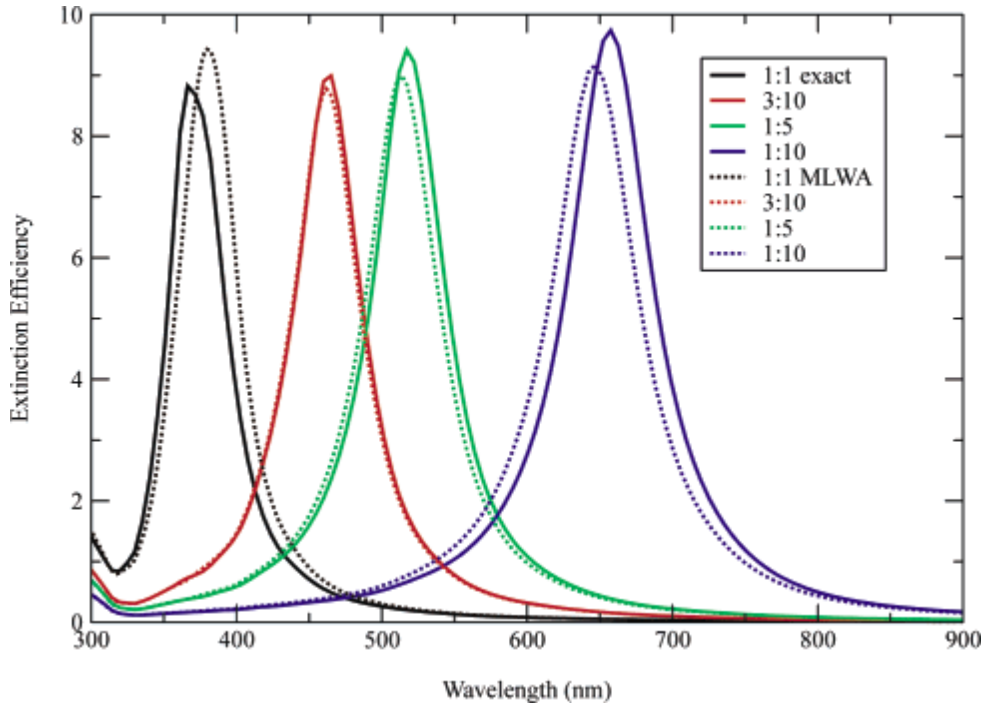

Figure 3.7: Extinction spectra of silver spheroids, the ratio of major to minor axis is, from left to right, r = 1, 3.33, 5, and 10.[9]

Influence of the nanoparticle structure and the surrounding medium:

As the nanofabrication technique developed, not only the nanospheres, but also people can synthesize the coated core-shell nanostructures. For example, a gold nanoshell with silica nanocore structure's extinction efficiency result is shown in Figure 3.8. [88]

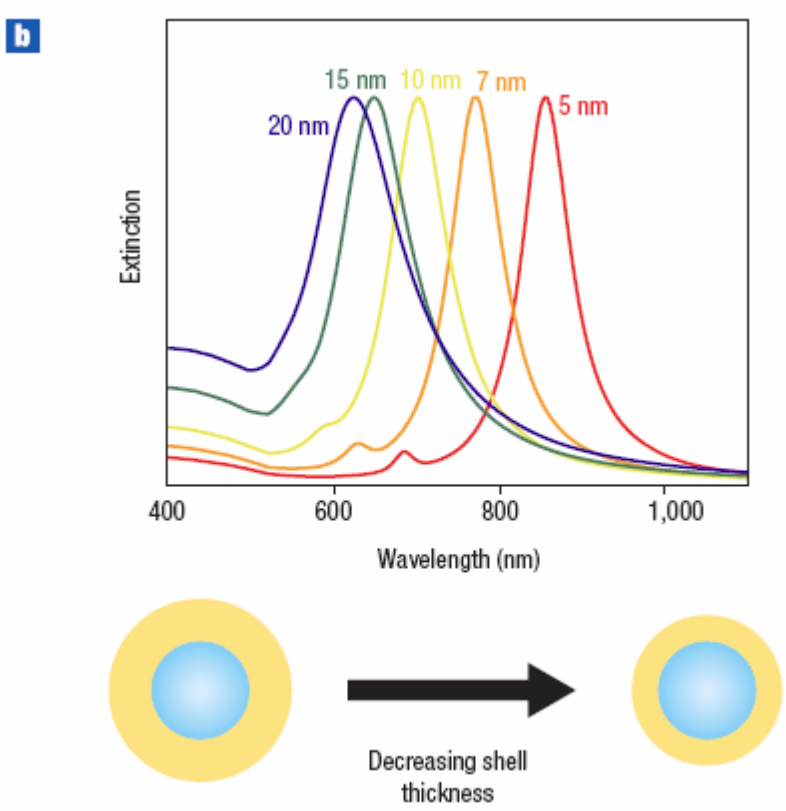

Figure 3.8: Plasmon resonances of a 120-nm-diameter silica core coated with varying thicknesses of a gold shell. As the size of the gold layer increases from 5 nm to 20 nm, the plasmon resonance is blue shifted.[88]

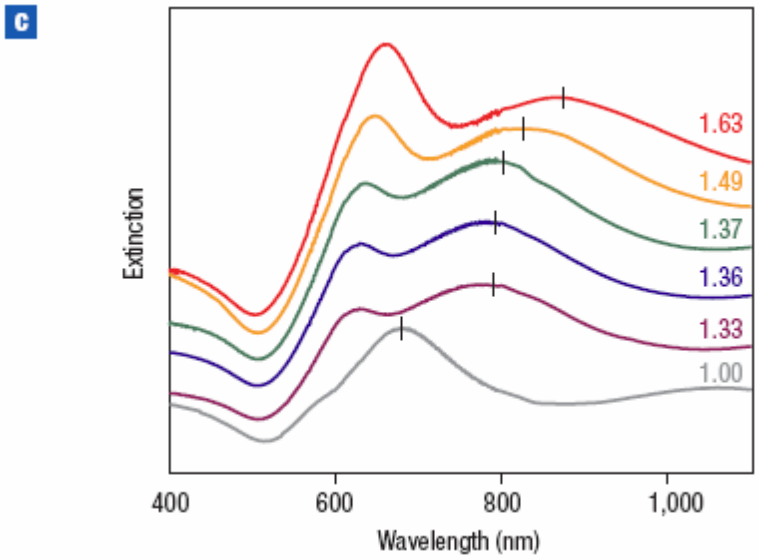

Figure 3.9: Surface plasmon resonance peak position shifts of a nanoshell's resonance with surrounding medium's refractive indices varying from 1.00 to 1.63.[88]

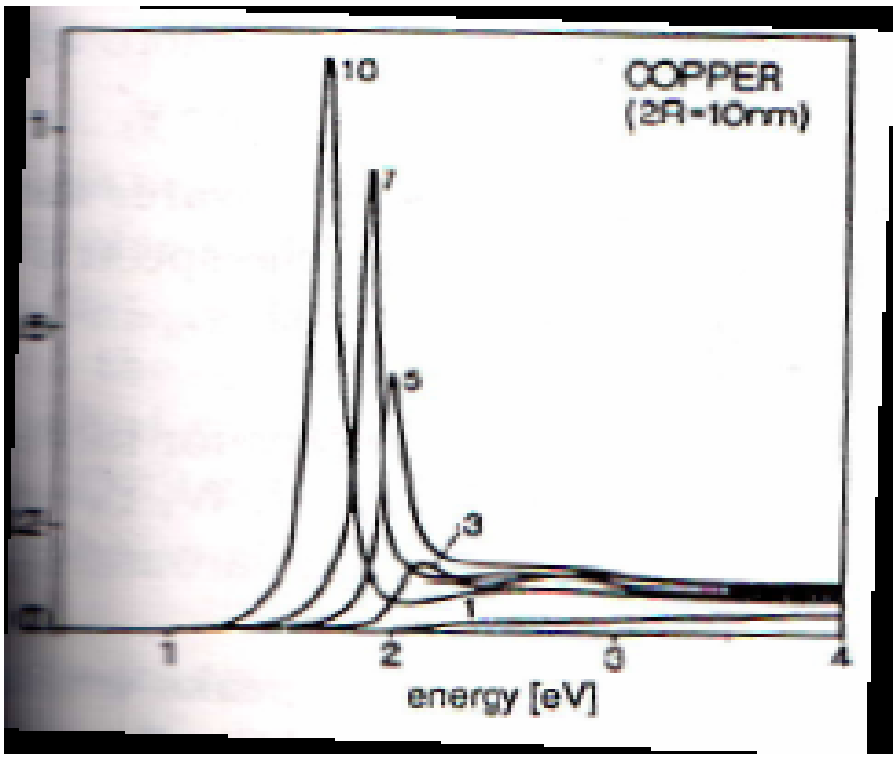

Figure 3.10: Surface plasmon resonance peak position shifts of a copper nanosphere. [5]

Finally, for the change of the surrounding medium's refractive index: (from figure 3.9 and 3.10) as the refractive index increases, the LSPR caused by nanospheres or nanoshells is red-shifted, and the extinction efficiency of this

resonance also increases. This property will be further evaluated when we come to the study of liquid crystal in later chapters.

3.2.3 Geometric Resonance

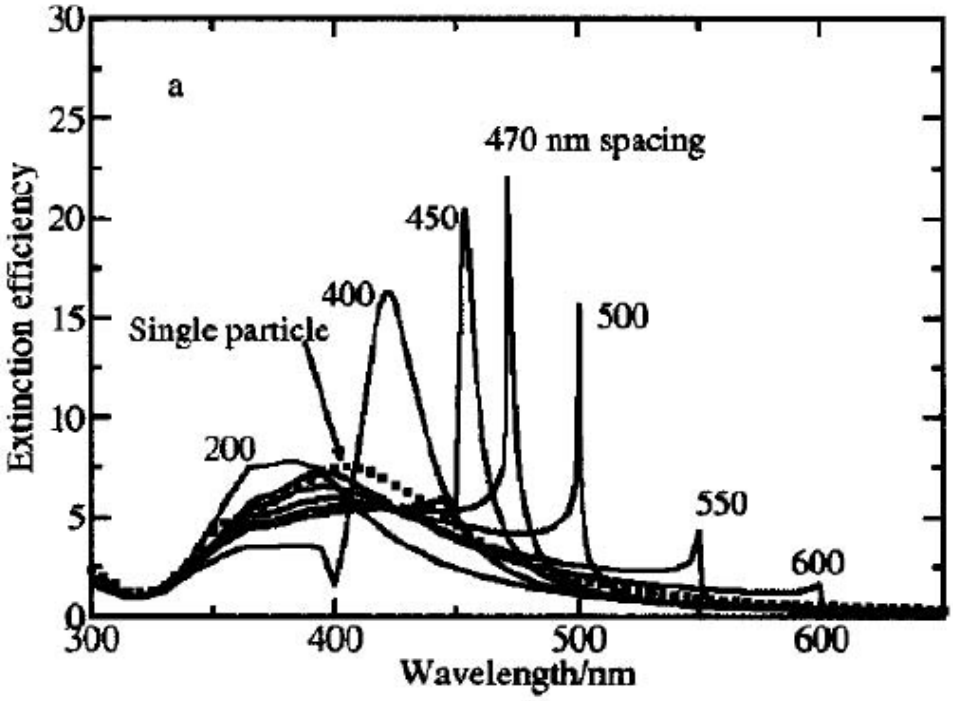

Figure 3.11: Extinction efficiency spectra for a 400 nanosphere one dimensional array with different inter-particle spacing. The radius of the nanosphere is 50nm. [90]

When an incident wave hits onto a well-defined periodic nanoparticle array, the scattering wave from one nanoparticle will has multiple scattering again by other periodic particles. Especially when the wavelength of the incident wave is close to the inter-particle distance, all of the scattering waves will be constructive interference, which creates a total resonance. The resonance from the interference is the so-called Geometric Resonance.

Geometric resonance has some special properties. For example, as shown in figure 3.11, the resonance has a much narrower bandwidth compared to LSPR [89, 90]. Also, the resonance is insensitive to the shape of the nanoparticles [91, 92]. In

nano-disk array [91] or nano-spheroid array [93], people have found the geometric resonance effect as well.

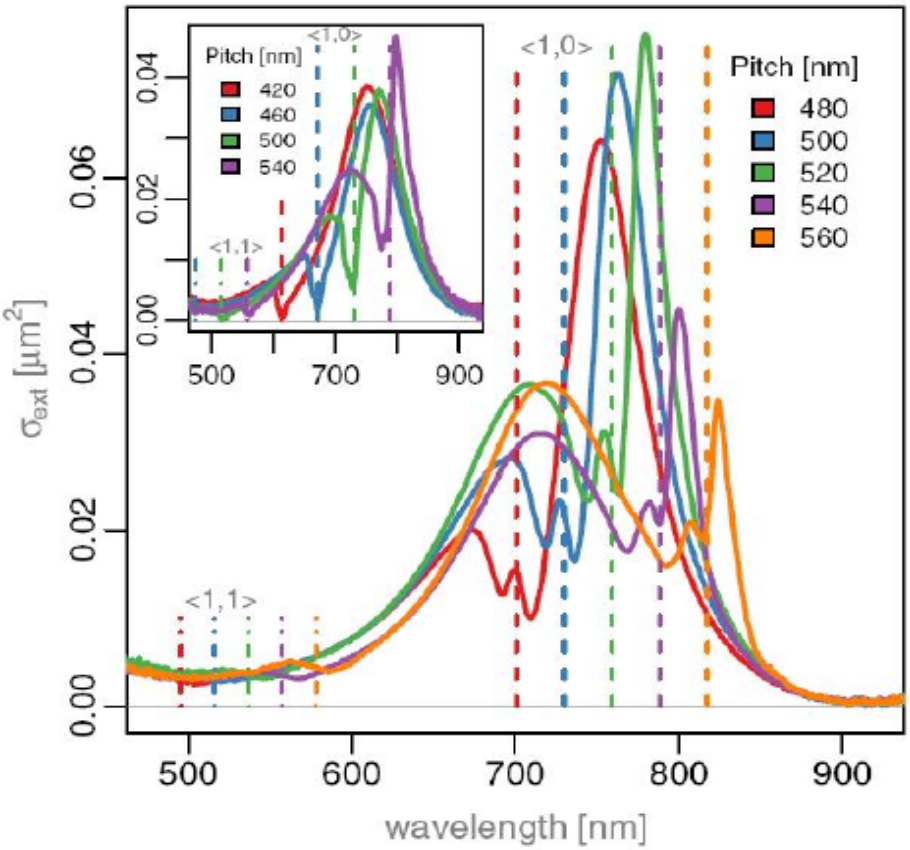

Figure 3.12: Extinction efficiency spectra from experimental result for a two-dimensional nano-spheroid array with different pitch/ inter-particle spacing. [93]

3.3 Methods to Study Surface Plasmon

In section 3.2.2, the Mie scattering theory was introduced. This theory gives an analytical solution to a specific kind of problem, such as a nanosphere dispersed medium. For more complex nanostructures, there is no general analytical solution. Because of this, some approximation methods or numerical calculations are considered. As the surface plasmon problems are still an electromagnetic field problem, the numerical simulation method Finite-Difference Time-Domain (FDTD) is one of the most useful methods. Besides FDTD, other approximation methods, e.g.

Coupled dipole approximation (CDA) [94], Discrete dipole approximation (DDA) [95, 96], Transition matrix method (TMM) [97], or Green's function method (GFM) [98] are also used according to a researcher's preference. In this dissertation, since liquid crystal is an anisotropic medium which cannot fit into many approximation methods' pre-requirements, the FDTD method is certainly a convenient choice.

FDTD is a very popular method in dealing with EM problems. This method was proposed by Yee in 1966 [99]. Start with the Maxwell Equations:

$$\nabla \times E = -\partial B / \partial t \tag{3.38}$$

$$\nabla \times H = \partial D / \partial t + J \tag{3.39}$$

Then re-arrange the equations into this form: [100]

$$\nabla \times E^{total} = -\mu \partial H^{total} / \partial t - \sigma^{*} H^{total} \tag{3.40}$$

$$\nabla \times H^{total} = \varepsilon \partial E^{total} / \partial t + \sigma E^{total} \tag{3.41}$$

Define: $E^{total} = E^{i} + E^{s}$, and $H^{total} = H^{i} + H^{s}$, then:

$$\frac{\partial H^{s}}{\partial t} = -\frac{(\mu - \mu_0)}{\mu}\frac{\partial H^{i}}{\partial t} - \frac{1}{\mu}(\nabla \times E^{s}) \tag{3.42}$$

$$\frac{\partial E^{s}}{\partial t} = -\frac{(\varepsilon - \varepsilon_0)}{\varepsilon}\frac{\partial E^{i}}{\partial t} - \frac{1}{\varepsilon}(\nabla \times H^{s}) \tag{3.43}$$

And the scattering E's and H's x components have the following relationship: (same for y and z components)

$$\frac{\partial E_x^{s}}{\partial t} = \frac{1}{\varepsilon}\left(\frac{\partial H_z^{s}}{\partial y} - \frac{\partial H_y^{s}}{\partial z}\right) \tag{3.44}$$

$$\frac{\partial H_x^{s}}{\partial t} = -\frac{1}{\mu_0}\left(\frac{\partial E_z^{s}}{\partial y} - \frac{\partial E_y^{s}}{\partial z}\right) \tag{3.45}$$

Consider, for any function f, these properties are valid:

$$\frac{\partial f}{\partial t} = \lim_{\Delta t \to 0} \frac{f(x,t_2) - f(x,t_1)}{\Delta t} \approx \frac{f(x,t_2) - f(x,t_1)}{\Delta t}$$
$$\frac{\partial f}{\partial x} = \lim_{\Delta x \to 0} \frac{f(x,t_2) - f(x,t_1)}{\Delta x} \approx \frac{f(x,t_2) - f(x,t_1)}{\Delta x} \tag{3.46}$$

The coupled equations (3.42) and (3.43) can be further developed into: [100]

$$\frac{E_x^{s,n} - E_x^{s,n-1}}{\Delta t} = \frac{1}{\varepsilon_0}\left[\frac{\Delta H_z^{s,n-\frac{1}{2}}}{\Delta y} - \frac{\Delta H_y^{s,n-\frac{1}{2}}}{\Delta z}\right] \tag{3.47}$$

$$\frac{H_y^{s,n+\frac{1}{2}} - H_y^{s,n-\frac{1}{2}}}{\Delta t} = \frac{1}{\mu_0}\left[\frac{\Delta E_z^{s,n}}{\Delta x} - \frac{\Delta E_x^{s,n}}{\Delta z}\right] \tag{3.48}$$

Equation (3.47) and (3.48) are the fundamental equations of the FDTD method. The idea of FDTD is: divide the whole calculation space into finite small square cells (Yee cell, [99]); for each cell, certain boundary conditions and Maxwell equations are valid. Then the value of the E and H field values of the eight surfaces' center of the cell can be calculated. Plug these values into eq. (3.47) and (3.48), one is able to get the E and H values of the adjacent cell, and so forth.

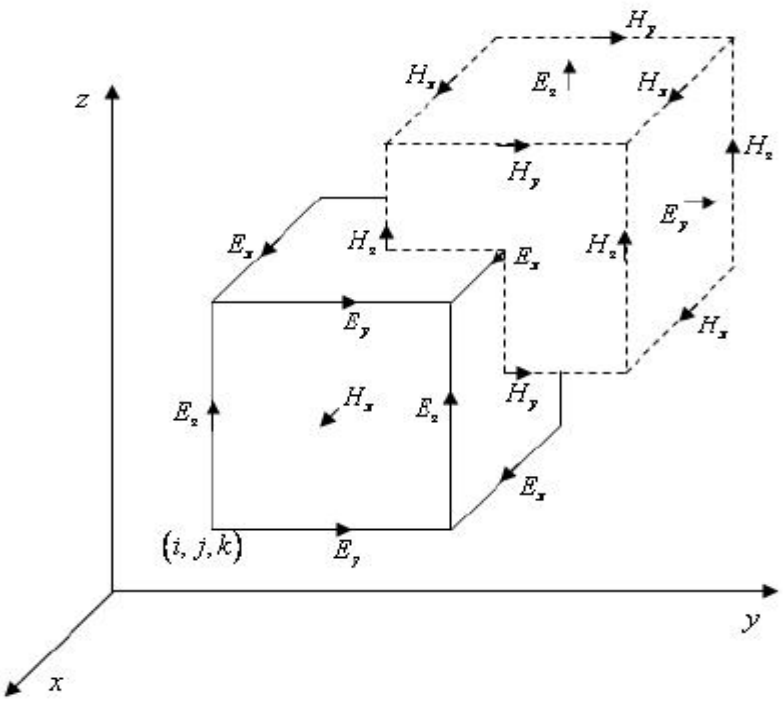

Figure 3.13: Illustration of the Yee cell with the FDTD method [99]

From the derivations, notice that: the FDTD method has no approximation of the field. To perform this calculation, a proper boundary condition and a small enough cell size is required. Most of the time, an absorbing boundary condition is selected. But sometimes, for periodic structures, a periodic boundary condition is preferred. For the cell size, the general requirements are:

$$\Delta x << \lambda \tag{3.49}$$

$$\Delta t << \frac{\Delta x}{\sqrt{3}c}, (\,for 3-D) \tag{3.50}$$

Now, some commercial FDTD software is ready for use in research related simulations, e.g. XFDTD [101] from Remcom, or FDTD Solutions [102] from Lumerical Solutions.

The FDTD method is very powerful. By selecting the correct conditions and using FDTD software, one could solve very complicated nanostructure problems. However, the results from the software are just the values of the E and H field. These results need appropriate physical interpretation and analysis.

Chapter 4 Nanoparticle Dispersed Liquid Crystal or Nonlinear Liquid

As mentioned in Chapter 1, the dispersion of nanoparticles in a nematic liquid crystal host medium is an efficient way to obtain a tunable optical response in the whole visible wavelength region. In this chapter, a brief discussion of the basic physics theory used in the refractive index calculation will be introduced. Then, the calculated results of the effective refractive index of the two types of nanoparticles, solid spheres and coated spheres, will be provided.

4.1 Fundamental Concepts

4.1.1 Effective Medium Theory

The calculation of the complex refractive index of the nanoparticles dispersed in NLCs with a tunable permittivity for the host medium is performed by using the Mie theory. This may also be called as effective medium theory [103].

First, consider an incident plane wave with magnetic field $H_{inc} = H_0 \exp(ik_o z)\hat{y}$ and $k_o = \varpi / c$, incident on a sphere of radius r_1 and relative permittivity $\varepsilon_1 = n_1^2 (\mu_1 = \mu_2 = \mu_3 = 1)$ with the host medium (liquid crystal) of relative permittivity $\varepsilon_3 = n_3^2$ .The scattered field is decomposed into multiple terms; the proportionality constant of the 2^n-pole coefficients can be calculated using the Mie scattering theory as introduced in section 3.2.2 [5]:

2^n-pole coefficients of scattered electric field:

$$a_n = \frac{\mu m^2 j_n(mx)[x j_n(x)]' - \mu_1 j_n(x)[mx j_n(mx)]'}{\mu m^2 j_n(mx)[x h_n^{(1)}(x)]' - \mu_1 h_n^{(1)}(x)[mx j_n(mx)]'}, \quad (4.1)$$

2^n-pole coefficients of scattered magnetic field:

$$b_n = \frac{\mu_1 j_n(mx)[xj_n(x)]' - \mu j_n(x)[mxj_n(mx)]'}{\mu_1 j_n(mx)[xh_n^{(1)}(x)]' - \mu h_n^{(1)}(x)[mxj_n(mx)]'}, \tag{4.2}$$

where the size parameter x and the relative refractive index m are defined as: $x = k_3 r_1$, $m = \frac{k_1}{k_3} = \frac{n_1}{n_3} = \sqrt{\varepsilon_r}$, and $\psi_n(\rho) = \rho j_n(\rho)$, $\xi_n(\rho) = \rho h_n^{(1)}(\rho) = \rho[j_n(\rho) + iy_n(\rho)]$ are the *Riccati-Bessel* functions.

The scattered magnetic dipole is shown as follows [5], which is proportional to b_1:

$$\begin{aligned} H_{sca} &= -\frac{3}{2} H_0 b_1 \{2\hat{r}\sin\theta\sin\phi\frac{h_1^{(1)}(k_0 r)}{k_0 r} + (\hat{\theta}\cos\theta\sin\phi + \phi\cos\phi)\frac{[k_0 r h_1^{(1)}(k_0 r)]'}{k_0 r}\} \\ &= \frac{3}{2}\frac{iH_0 b_1}{k_0^3}\frac{e^{ik_0 r}}{r}\{k_0^2(\hat{r}\times\hat{y})\times r + [3(y\cdot r)r - y](\frac{1}{r^2} - \frac{ik_0}{r})\} \end{aligned} \tag{4.3}$$

This expression may be compared with the standard expression of magnetic dipole radiation: [104]

$$H_{dipole} = \frac{1}{4\pi}\frac{e^{ik_0 r}}{r}\{k_0^2(\hat{r}\times\hat{m})\times r + [3(m\cdot r)r - m](\frac{1}{r^2} - \frac{ik_0}{r})\} \tag{4.4}$$

Therefore, the sphere is equivalent to a magnetic dipole with an effective moment m and effective polarizability α_m, where $m = \alpha_m H_{inc}(0) = \alpha_m H_0 \hat{y}$ [105]

The effective polarizability is then [105] $\alpha_m = 6\pi i b_1 / k_0^3$.

From the Clausius-Mossotti equation [104], the polarizability (in the long-wavelength limit) is also equal to: $\alpha_m = \frac{3}{N}(\frac{\mu^{eff} - 1}{\mu^{eff} + 2})$, where the μ^{eff} is the effective permeability, and N is the volume density of the spheres. Assuming the nanoparticles are homogeneously dispersed in the host medium, the filling fraction of the composite will be $f = 4\pi N r_1^3 / 3$.

The response of the bulk composite is given by the effective permittivity and permeability:

Effective Permittivity: $\varepsilon^{eff} = \varepsilon_3(\frac{k_3^3 + j4\pi Na_1}{k_3^3 - j2\pi Na_1})$

Effective Permeability: $\mu^{eff} = \frac{k_3^3 + j4\pi Nb_1}{k_3^3 - j2\pi Nb_1}$

Notice: an assumption has been made that the particles are homogeneously dispersed in the medium. If considering inhomogeneous dispersion, the average (effective) dielectric function is calculated by the Maxell-Garnett mixing rule [5].

$$\varepsilon_{av} = \varepsilon_m[1 + \frac{3f(\frac{\varepsilon - \varepsilon_m}{\varepsilon + 2\varepsilon_m})}{1 - f(\frac{\varepsilon - \varepsilon_m}{\varepsilon + 2\varepsilon_m})}] \tag{4.5}$$

$$\mu_{av} = \mu_m[1 + \frac{3f(\frac{\mu - \mu_m}{\mu + 2\mu_m})}{1 - f(\frac{\mu - \mu_m}{\mu + 2\mu_m})}] \tag{4.6}$$

It can be shown that using these two effective permittivity and permeability separately, the result is almost the same; it only varies when the filling-fraction is high (i.e. ~ 25%), in which case there is a slight difference.

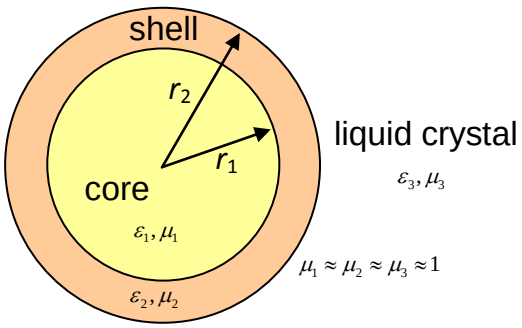

Figure 4.1: Coated spheres with surrounding medium liquid crystal [55]

As shown in the figure 4.1, for coated spheres, the core is in the region $0 < r < r_1$ with index $n_1 = \varepsilon_1^{\,2}(\mu_1 \approx \mu_2 \approx \mu_3 \approx 1)$; the coating is in the region $r_1 < r < r_2$ with

index $n_2 = \varepsilon_2^2$, the scattering coefficients can also be calculated by using the Mie theory, as given by [5]:

$$a_n = \frac{\psi_n(y)\left[\psi_n'(m_2 y) - A_n \chi_n'(m_2 y)\right] - m_2 \psi_n'(y)\left[\psi_n(m_2 y) - A_n \chi_n(m_2 y)\right]}{\xi_n(y)\left[\psi_n'(m_2 y) - A_n \chi_n'(m_2 y)\right] - m_2 \xi_n'(y)\left[\psi_n(m_2 y) - A_n \chi_n(m_2 y)\right]} \tag{4.7}$$

$$b_n = \frac{m_2 \psi_n(y)\left[\psi_n'(m_2 y) - B_n \chi_n'(m_2 y)\right] - \psi_n'(y)\left[\psi_n(m_2 y) - B_n \chi_n(m_2 y)\right]}{m_2 \xi_n(y)\left[\psi_n'(m_2 y) - B_n \chi_n'(m_2 y)\right] - \xi_n'(y)\left[\psi_n(m_2 y) - B_n \chi_n(m_2 y)\right]} \tag{4.8}$$

with coefficients

$$A_n = \frac{m_2 \psi_n(m_2 x)\psi_n'(m_1 x) - m_1 \psi_n'(m_2 x)\psi_n(m_1 x)}{m_2 \chi_n(m_2 x)\psi_n'(m_1 x) - m_1 \chi_n'(m_2 x)\psi_n(m_1 x)} \tag{4.9}$$

$$B_n = \frac{m_2 \psi_n(m_1 x)\psi_n'(m_2 x) - m_1 \psi_n(m_2 x)\psi_n'(m_1 x)}{m_2 \chi_n'(m_2 x)\psi_n(m_1 x) - m_1 \psi_n'(m_1 x)\chi_n(m_2 x)} \tag{4.10}$$

where the arguments are

$$x = k_3 r_1, \quad y = k_3 r_2$$
$$m_1 = \frac{n_1}{n_3}, \quad m_2 = \frac{n_2}{n_3}$$

and $\chi_n(\rho) = -\rho y_n(\rho)$ is the Riccati-Bessel function of the second kind.

4.1.2 Material Models

Metals

There are two types of models used for metals. One is a well-known Lorentz-Drude Model, or just simply called the LD model; the other one is described by Brendel and Bormann, which is called the BB model. [106]

The LD model's dielectric function has been shown as: [107]

$$\varepsilon_r(\varpi) = \hat{\varepsilon}_r^{(f)}(\varpi) + \varepsilon_r^{(b)}(\varpi)$$

The intraband part $\hat{\varepsilon}_r^{(f)}(\varpi)$ is described by the free-electron Drude model

[107]: (notice here, to be consistent with the notation before: $E_{inc} = E_0 \exp(ik_o z)\hat{x}$ [5], the plus sign is used instead of the minus sign in Ref.107).

$$\hat{\varepsilon}_r^{(f)}(\varpi) = 1 - \frac{\Omega_p^2}{\varpi(\varpi + i\Gamma_0)} \tag{4.11}$$

The interband part $\hat{\varepsilon}_r^{(b)}(\varpi)$ is described by the simple semi quantum model that resembles the Lorentz result for insulators: [107]

$$\hat{\varepsilon}_r^{(b)}(\varpi) = \sum_{j=1}^{k} \frac{f_j \varpi_p^2}{(\varpi_j^2 - \varpi^2) + i\varpi\Gamma_j}, \tag{4.12}$$

where ϖ_p is the plasma frequency, k is the number of oscillators with frequency ϖ_j, strength f_j and lifetime $1/\Gamma_j$, while $\Omega_p = \sqrt{f_0}\varpi_p$ is the plasma frequency associated with intraband transitions with oscillator strength f_0 and damping constant Γ_0.

Usually the Gaussian line shape is a much better approximation for the broadening function than the Lorentzian line shape. This BB model of the Gaussian line shape is used to describe optical properties of a wide range of materials, including metals [107].

The difference between these two models is at the interband part, which for the BB model is:

$\hat{\varepsilon}_r^{(b)}(\varpi) = \sum_{j=1}^{k} \chi_j(\varpi)$, where k is the number of the BB oscillators $\chi_j(\varpi)$.

$$\chi_j = \frac{i f_j \varpi_p^2}{2\sqrt{2}\alpha_j \sigma_j}\{U[1/2,1/2,-(\frac{\alpha_j - \varpi_j}{\sqrt{2}\sigma_j})^2] + U[1/2,1/2,-(\frac{\alpha_j + \varpi_j}{\sqrt{2}\sigma_j})^2]\}, \tag{4.13}$$

where $U[1/2,1/2,z^2] = \sqrt{\pi}e^{z^2}erfc(z)$ is the Kummer function of the second kind, and erfc(z) is the complementary error function. To satisfy the condition that the imaginary part of α_j must be larger than zero, the solution for α_j is: [107]

$$\alpha_j = \alpha_j' + \alpha_j'' \tag{4.14}$$

$$\alpha_j' = \frac{\varpi}{\sqrt{2}}\{[1+(\Gamma_k/\varpi)^2]^{1/2}+1\}^{1/2}, \tag{4.15}$$

$$\alpha_j'' = \frac{\varpi}{\sqrt{2}}\{[1+(\Gamma_k/\varpi)^2]^{1/2}-1\}^{1/2}. \tag{4.16}$$

Finally, the complete optical dielectric function for the BB model reads:

$$\hat{\varepsilon}_r(\varpi) = 1 - \frac{\Omega_p^2}{\varpi(\varpi + i\Gamma_0)} + \sum_{j=1}^{k} \chi_j(\varpi) \tag{4.17}$$

The following figure, 4.2, is the analysis of these two models for Gold and Silver.

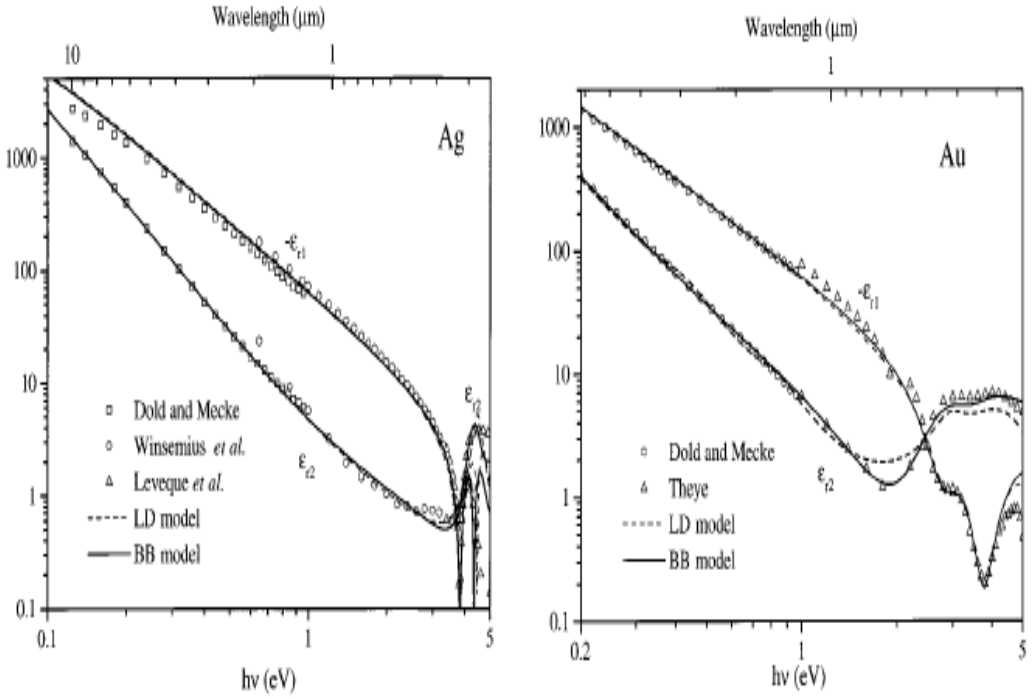

Figure 4.2: Comparison of the LD model and the BB model. Left: Real and imaginary parts of the optical dielectric function of Ag., the solid curve is the calculated value using the BB model,the dashed curve the LD model; Right: Real and imaginary parts of the optical dielectric function of Au., the solid curve is the calculated value using the BB model, the dashed curve the LD model. [107]

At around 2 eV, the BB model fits the data much better than the LD model. The result shows that the BB model is needed for an appropriate description of the

onset of interband absorption in noble metals (e.g. Ag, Au).

Liquid Crystal

The permittivity of the host medium, nematic liquid crystal (NLC) is very tunable. For a linearly polarized light incident at an oblique angle θ, ε_{host} is given by: [17]

$$\varepsilon_{host} = \frac{\varepsilon_{\parallel}\varepsilon_{\perp}}{\varepsilon_{\parallel}\cos^2\theta + \varepsilon_{\perp}\sin^2\theta}, \tag{4.18}$$

where $\varepsilon_{\parallel}$ and $\varepsilon_{\perp}$ are the respective permittivity for light polarized parallel and perpendicular to the director axis $\hat{n}$, and θ is the angle made by the director axis with the optical wave vector k_0. This model, which can be derived from the Eq. (2.3), does not carry any frequency dependence and the angle θ may vary continuously if an electric field is applied to the material. In the case of nanoparticles dispersed liquid crystal, the permittivity of the host medium ε_{host} can continuously vary from 2.0 to 4.0, which is achievable in the nematic liquid crystal.

4.1.3 Electron-Free Path

The small size of the nanoparticles will result in a limit of the mean free path for the free electrons, and then increase the rate of scattering from the surface of the particle due to bulk scattering. [5] This effect is taken into account by adding to the damping constant γ_0 in the free-electron Drude model at a surface scattering rate of $\varpi_s = Av_f / r$ where v_f is the Fermi velocity, r is the radius of the nanoparticle, and A is a proportional factor. The intraband expression $\hat{\varepsilon}_r^{(f)}(\varpi)$ is modified to: [108]

$$\hat{\varepsilon}_r^{(f)}(\varpi) = 1 - \frac{\Omega_p^2}{\varpi(\varpi + i(\Gamma_0 + Av_F / r))}, \tag{4.19}$$

where $\Omega_p = \sqrt{f_0 \varpi_p}$ is the plasma frequency associated with intraband transitions with oscillator strength f_0 and damping constant Γ_0, as defined before. Since the only changes are in the intraband part of the permittivity, the eq. (4.19) applies to both the LD and the BB models.

From the literature and previous research [108], the factor A is set to be 1.4 for gold [109] and 0.25 for silver [110].

4.2 Dispersion of Nanoparticles in Nematic Liquid Crystal

4.2.1 Model Selection

Before the simulation, the selection of models is necessary.

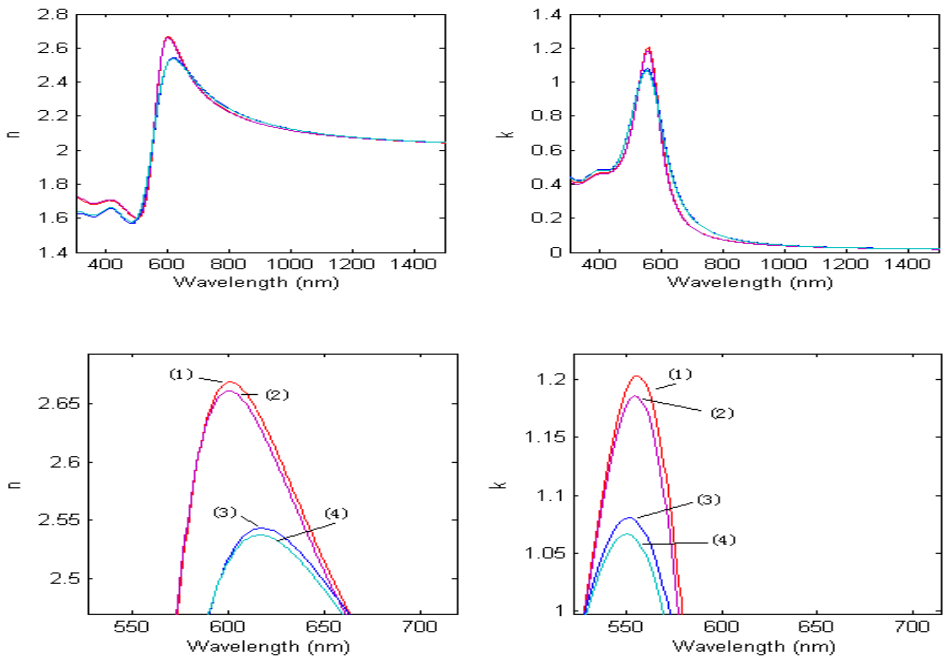

Figure 4.3: Comparison of the models: Top two, permittivity of the host medium, $\varepsilon_{host} = 2.0$ *nanoparticle: solid gold, filling fraction of the nanosphere is 0.25, using four different combinations: Curve (1): the BB model for gold and using the Clausius-Mossotti equation to calculate the effective permittivity. Curve (2): the BB model for gold and using the Maxell-Garnett mixing rule to calculate the effective*

permittivity. Curve (3): the LD model for gold and using the Clausius-Mossotti equation to calculate the effective permittivity. Curve (4): the LD model for gold and using the Maxell-Garnett mixing rule to calculate the effective permittivity.

From figure 4.3, the results for the effective permittivity when using the Clausius-Mossotti equation or the Maxell-Garnett mixing rule are almost the same (compare 1 and 2, or 3 and 4). As the nanoparticle dispersed in the NLC is assumed to be homogenous, the more commonly used Clausius-Mossotti equation will be used for the calculation of the effective permittivity for the material. The bigger difference is between the LD model and the BB model when describing the metal. To choose between these two, some experimental results are needed.

The following figures are from previous research [108]:

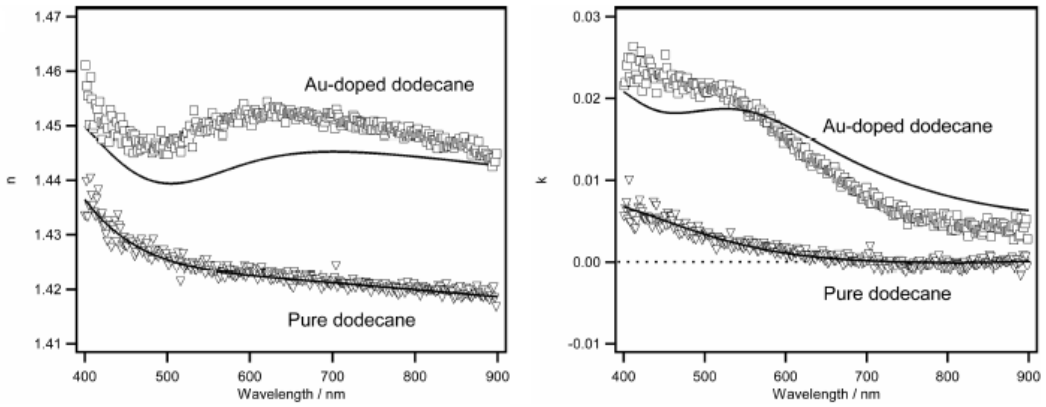

Figure 4.4(a) Comparison of experimentally measured and theoretically calculated refractive indices of pure dodecane and gold nanoparticles dispersed in dodecane at a volume fraction of 1.0%. Solid line: calculated results using LD model for Au, a constant value of A=1.4; markers: experimental results [108].

These figures are about gold nanoparticles dispersed in a host medium with dodecane. For the pure dodecane, the calculated curve agrees with the experimental result very well. For the Au-doped one, the two are the same with the trend for the curve, however the values are different.

With the same configuration but different material models, the following curves can be calculated:

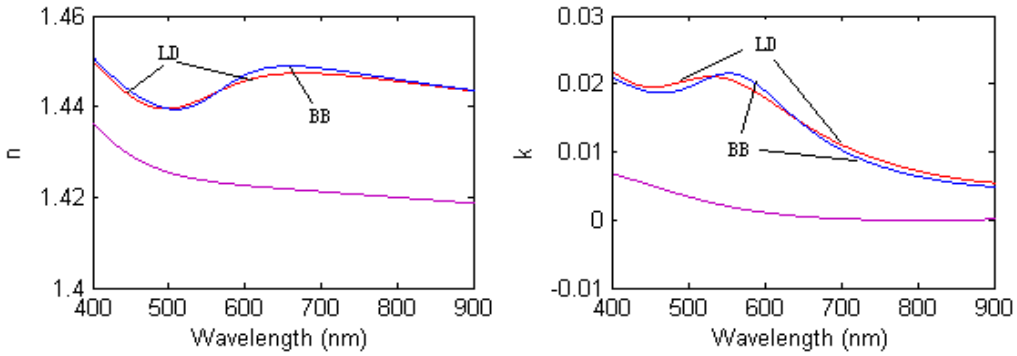

Figure 4.4(b) Comparison of theoretically calculated refractive indices between different models (LD and BB), configuration same as 4.4(a)

Compare figure 4.4(b) with figure 4.4(a), in this visible wavelength region, the BB model has better agreement in the value with the measured permittivity of metals. Based on these, the BB model is the one used for later calculation in describing metal permittivity.

4.2.2 Solid Spheres

For the gold nanoparticle, using the BB model and the parameter found in the literature[107], the parameters are: ϖ_p =9.03eV, f_0 =0.770, Γ_0 =0.050eV, f_1 =0.054, Γ_1 =0.074eV, ϖ_1 =0.218eV, σ_1 =0.742eV, f_2 =0.050, Γ_2 =0.035eV, ϖ_2 =2.885eV, σ_2 =0.349eV, f_3 =0.312, Γ_3 =0.083eV, ϖ_3 =4.069eV, σ_3 =0.830eV, f_4 =0.719, Γ_4 =0.125eV, ϖ_4 =6.137eV, σ_4 =1.246eV, f_5 =1.648, Γ_5 =0.179eV, ϖ_5 =27.97eV, and σ_5 =1.795eV. The other parameters are: filling fraction 0.25, gold particle radius 2nm, and the host medium dielectric constant varies between 2.0 and 4.0(step 0.5).

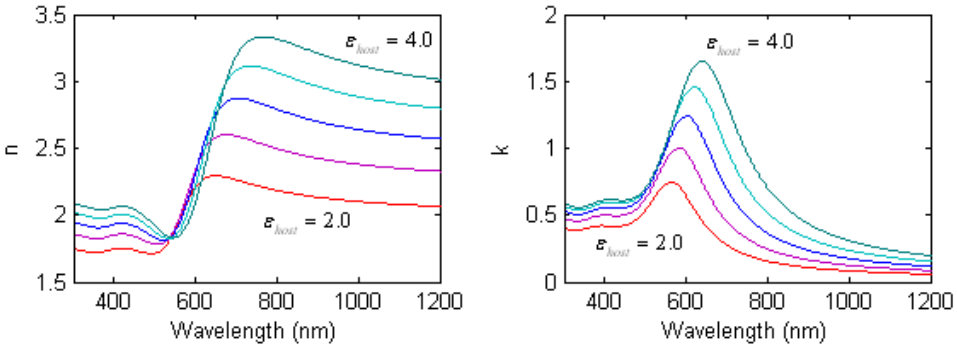

Figure 4.5: Calculation of the real (n) and imaginary (k) parts of the refractive index for 2nm radius gold nanoparticle dispersed in NLC, when relative permittivity ε_{host} varies between 2.0 and 4.0 in steps of 0.5.

For the silver nanoparticle, when also using the BB model and the parameters found in the literature [107], the parameters are: ϖ_p =9.01eV, f_0=0.821, Γ_0 =0.049eV, f_1 =0.050, Γ_1 =0.189eV, ϖ_1 =2.025eV, σ_1 =1.894eV, f_2 =0.133, Γ_2 =0.067eV, ϖ_2 =5.185eV, σ_2 =0.665eV, f_3 =0.051, Γ_3 =0.019eV, ϖ_3 =4.343eV, σ_3 =0.189eV, f_4 =0.467, Γ_4 =0.117eV, ϖ_4 =9.809eV, σ_4 =1.170eV, f_5 =4.000, Γ_5 =0.052eV, ϖ_5 =18.56eV, and σ_5 =0.516eV.

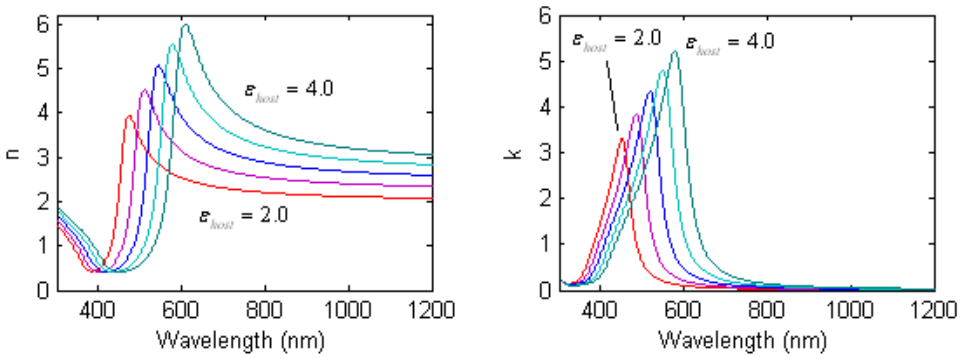

Figure 4.6: Calculation of the real (n) and imaginary (k) parts of the refractive index for 2nm radius silver nanoparticle dispersed in NLC when relative permittivity ε_{host} varies between 2.0 and 4.0 in steps of 0.5.

From Figure 4.5 and 4.6, for the gold nanoparticle dispersion, the effective index is always greater than 1.0, even if the filling fraction is very large (e.g. more than 50%). For the silver particles, however, clearly the minimum effective refractive index is less than 1.0, in this case, a minimum of n_{eff} =0.4101 is obtained at the wavelength of 416.5nm when ε_{host} =3.0.

In both cases, the range of values of the refractive index's real part is greater than the expected changes from the variation of the host medium alone. Moreover, the silver particles' changes are bigger than the gold one when the silver particle was the same size as the gold particles. In the case shown in Figure 4.6, assume an incident beam with wavelength at 532nm: for $\lambda = 532.1nm$, the minimum n=0.9975 is obtained at ε_{host} =4.0 and the maximum n=4.678 is obtained at ε_{host} =3.0. The difference of n is 3.68, with the permittivity of the host medium changing only 1.0. This birefringence of the refractive index is much bigger with the nanoparticle dispersion. This property is useful for the nonlinear optics study of liquid crystals, as mentioned in Chapter 2.

4.2.3 Coated Nanoshells

The following figures show the real and imaginary parts of the refractive index for Au/Ag-coated silica nanoshells.

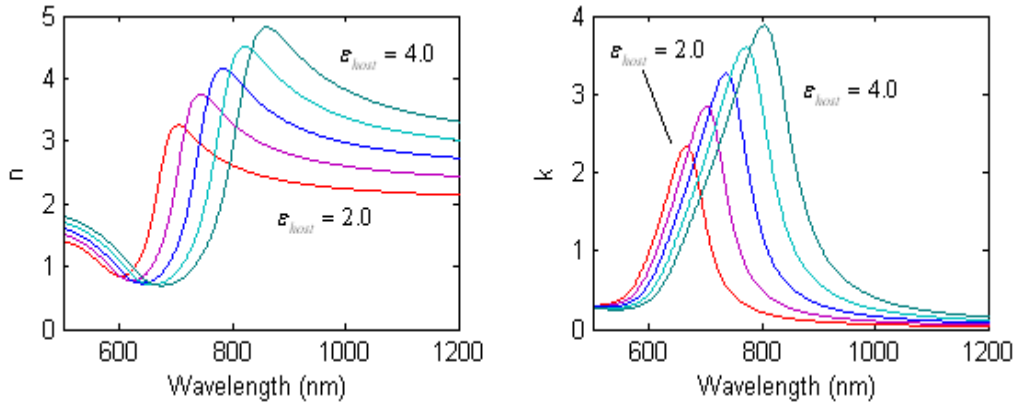

Figure 4.7: Calculation of the real part (n) and the imaginary part (k) of the refractive index for silica-gold core-shell nanospheres dispersed in a NLC. The radius for the silica core is 10nm with a permittivity of 3.8, and the thickness for the shell (gold) is 5nm. The filling fraction is 0.25. The permittivity of the host medium (NLC) varies from 2.0 to 4.0 in steps of 0.5.

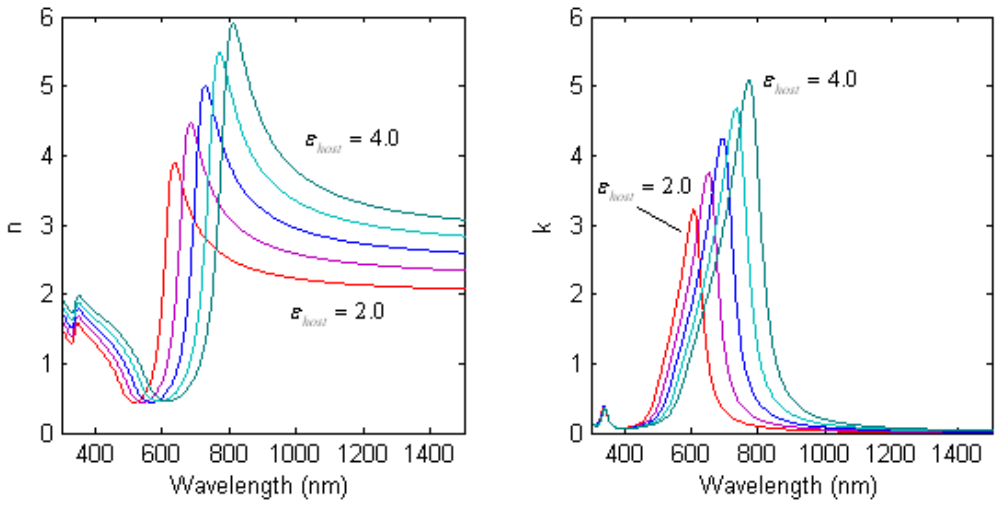

Figure 4.8: Calculation of the real part (n) and the imaginary part (k) of the refractive index for silica-silver core-shell nanospheres dispersed in a NLC. The radius for the silica core is 10nm with a permittivity of 3.8, and the thickness for the shell (silver) is 5nm. The filling fraction is 0.25. The permittivity of the host medium (NLC) varies from 2.0 to 4.0 in steps of 0.5.

Generally for the coated nanoshells, by increasing the diameter of the silica core, it is possible to shift the part of low index to a longer wavelength region, while the values of the index remain the same [111].

For the nanoshells dispersed liquid crystal: As in figure 4.7, the lowest point of the real part of the refractive index n is 0.6984, at 673.9nm wavelength and $\varepsilon_{host} = 4.0$. In figure 4.8, the lowest point of the real part of the refractive index n is 0.439, at 540.2nm wavelength and $\varepsilon_{host} = 2.5$. Both of these structures reach a sub-unity refractive index of the real part.

Further, the localized surface plasmon resonance caused by the nanoparticles or nanoshells is considered. From figures 4.5 - 4.8, as the refractive index increases, the LSPR resonance peak position is red-shifted. This conclusion is the same as in section 3.2.3, when the LSPR effect was introduced with the surrounding medium's change. Because the efficiency of this resonance increases as the refractive index increases, the bulk medium enjoys a bigger bulk's refractive index. This is the impact on the liquid crystal by the nanoparticles.

Also notice: in order to have a bigger effect on the tuning of the refractive index and surface plasmon resonance, the filling fraction set here is 0.25, which is very high compared with the other work, such as the one in section 4.3. In fact, it is hard to dissolve the metal nanoparticles into the liquid crystal material. In this case, an ultrasonic dispersion may be considered. The detailed fabrication of the material is ignored in this dissertation.

More details about this work and the applications of using a larger tuning range of the refractive index for nonlinear optical applications can be found in the Ref. 17.

4.3 Dispersion of Nanoparticles in Nonlinear Liquid

As described in section 2.4, liquid crystal is one of the nonlinear optical materials with high nonlinearity. Many nonlinear optical phenomena have been observed in liquid crystals, such as two photon absorption (TPA) [17]. Recently, our lab and co-workers have developed a new kind of “nonlinear liquid”, which is called L34 [113]. L34, or liquid crystals in their isotropic phase (i.e. neat liquid), has a nonlinear TPA effect that can be used for very fast all-optical switching operations in the sub-nanosecond time scale [57,113].

In previous research from our lab, we already found that in the carbon nanotube- or C60-doped nematic liquid crystals [54], or Methyl-red doped liquid crystals [52], the nonlinearity could be modulated and enhanced. This kind of research was performed on the nonlinear liquid L34. Recently, it is believed that by doping metal nanoparticles, the TPA coefficient is enhanced [114]. In the following, this effect is analyzed and some predictions by simulation will be made based on the actual experimental results.

I will start with the physical property of the nonlinear liquid- L34. The real part of the refractive index of L34 is around 1.61, and the imaginary part of the refractive index is derived from the absorbance spectrum using eq. (4.20) below (host: L34)

$$n''_{host} = \frac{\lambda}{4\pi}\alpha \tag{4.20}$$

The absorbance (in cm^{-1}) is shown in figure 4.9 [113].

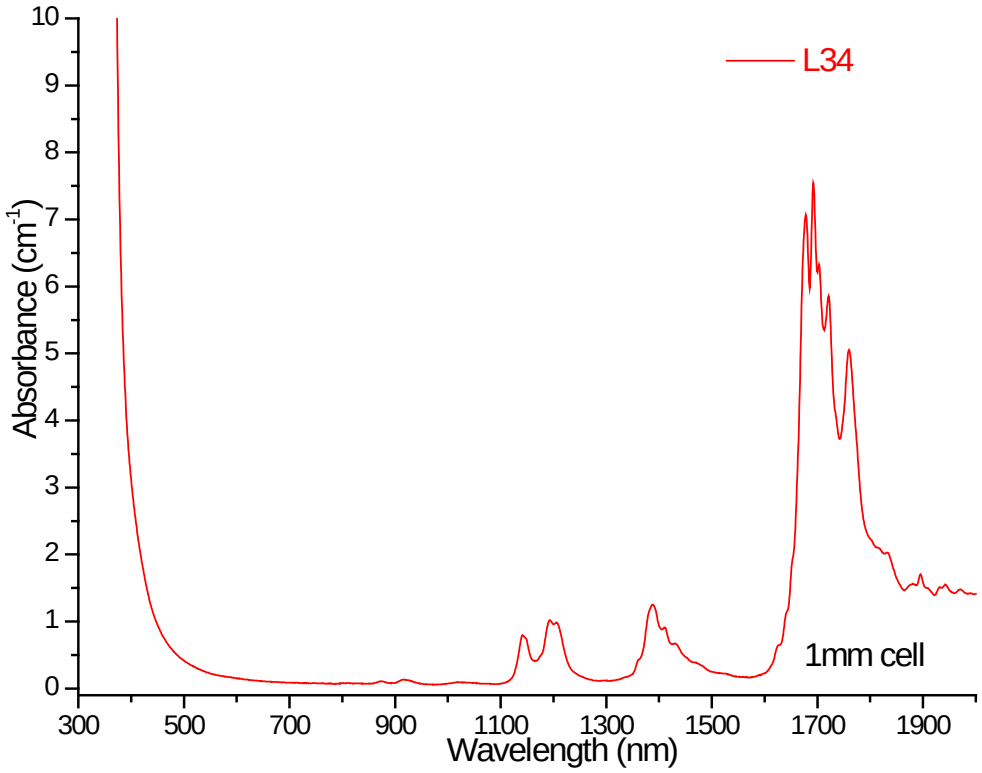

Figure 4.9: Absorbance spectrum of L34 [113]

Next, consider a gold nanoparticle dispersed in the host medium L34. Using the Maxwell-Garnett (MG) mixing rule as mentioned in Chapter 4 for the composite, the effective composite dielectric constant is calculated as:

$$\varepsilon_{com} = \frac{1+2f\gamma}{1-f\gamma}\varepsilon_{host}, \gamma = \frac{\varepsilon_{Au}-\varepsilon_{host}}{\varepsilon_{Au}+2\varepsilon_{host}}$$ f: filling fraction for the gold particle.

The equations above are the same as Eq. (4.5) and (4.6).

To extend the MG theory into the nonlinear optical field, J. E. Sipe and R.W. Boyd [115] have calculated the nonlinear susceptibility of a composite nonlinear host material filling with spherical nanoparticles. The resulting nonlinear susceptibility enhancement factor $g^{(3)}$ of the third order susceptibility of this metal-host composite is given by: [115]

$$g^{(3)} \equiv \frac{\chi^{(3)}_{com}}{\chi^{(3)}_{host}} = \frac{1}{5}\left|\frac{\varepsilon_{com}+2\varepsilon_{host}}{3\varepsilon_{host}}\right|^2\left(\frac{\varepsilon_{com}+2\varepsilon_{host}}{3\varepsilon_{host}}\right)^2 [8f|\gamma|^2\gamma^2+6f|\gamma|^2\gamma+2f\gamma^3+18f(|\gamma|^2+\gamma^2)+5(1-f)] \quad (4.21)$$

Because the nonlinear refractive index $n_2 = \frac{3}{4\varepsilon_0 c|n_0|^2}(1-i\frac{n_0''}{n_0'})\chi^{(3)}$, then a nonlinear refractive index enhancement factor $g^{(2)}$ can be defined as:

$$g^{(2)} \equiv \frac{n_{2,com}}{n_{2,host}} = \frac{|n_{0,host}|^2}{|n_{0,com}|^2}\frac{1-i(n_{0,com}''/n_{0,com}')}{1-i(n_{0,host}''/n_{0,host}')}g^{(3)} \quad (4.22)$$

Thus, to obtain the effective nonlinear absorption coefficient from the imaginary part of the nonlinear refractive index of the composite, the real part of the nonlinear refractive index of L34 and the intrinsic TPA absorption coefficient of L34 need to be determined using the z-scan technique [116]. From previous z-scan experimental results, [114] the real part of the nonlinear refractive index of L34 is shown in Fig.4.10.

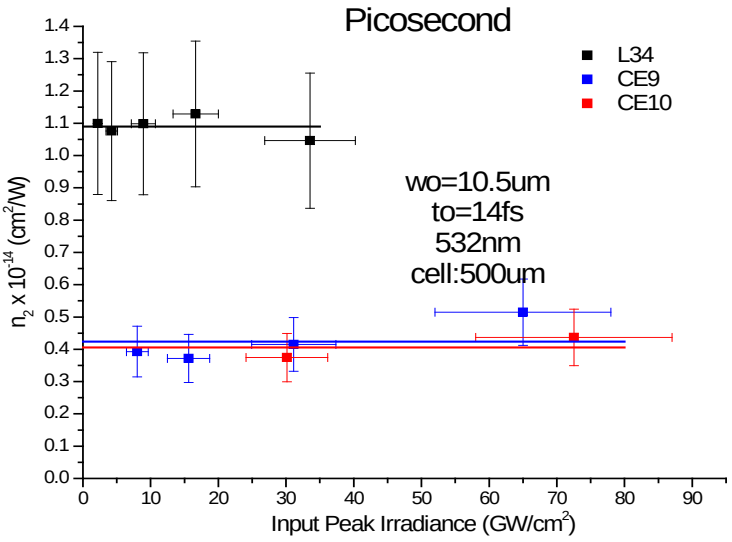

Figure 4.10: Pico-second z-scan experimental results of the real part of the L34's nonlinear refractive index.

To simplify, in our calculation the $n_{0,host}'$ value is selected to be 1×10^{-14} (cm^2/W). Next, the intrinsic TPA absorption coefficient of L34 is changed from 3.4 cm/GW to 4 cm/GW, as shown in Fig.4.11. (The experimental results in this figure are from Ref. 114.)

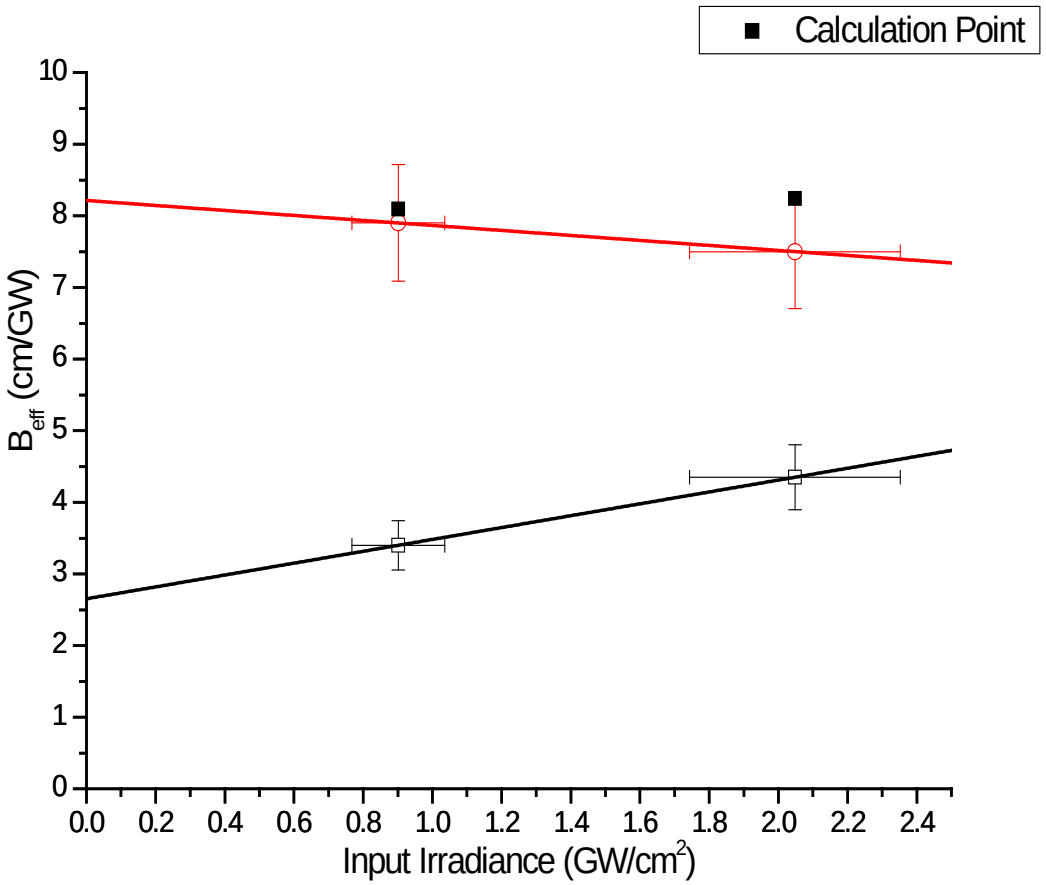

Figure 4.11: Simulation and experimental results for effective nonlinear absorption coefficient. The experiments were done by 460nm 83 ps laser. Cell thickness: 0.1 mm; laser focused beam waist: 10 m; Au nano-spheres diameter: 4 nm.

From Fig.4.11, within the error bar the calculation results fit very well with the experimental results. Based on this, one is able to further evaluate the factors that may impact the enhancement effect.

For the same filling fraction (0.5%), the particle's diameter is the first factor to

be studied. For a gold nanosphere, the diameter is increased from 4nm to 10nm. For the intrinsic TPA absorption coefficient of L34 to equal 4 cm/GW, the calculated effective nonlinear absorption coefficient effective (β_{eff}) for 4nm case is 8.241 cm/GW; whereas for 10nm, it is 12.72 cm/GW at the wavelength of 460nm. For a bigger sized particle, a larger enhancement in the β_{eff} is expected.

Next is the evaluation of the impact from the change of the intrinsic TPA absorption coefficient. The 140fs z-scan experiment data (Fig. 4.12) is employed. The calculation result is shown in Fig. 4.13.

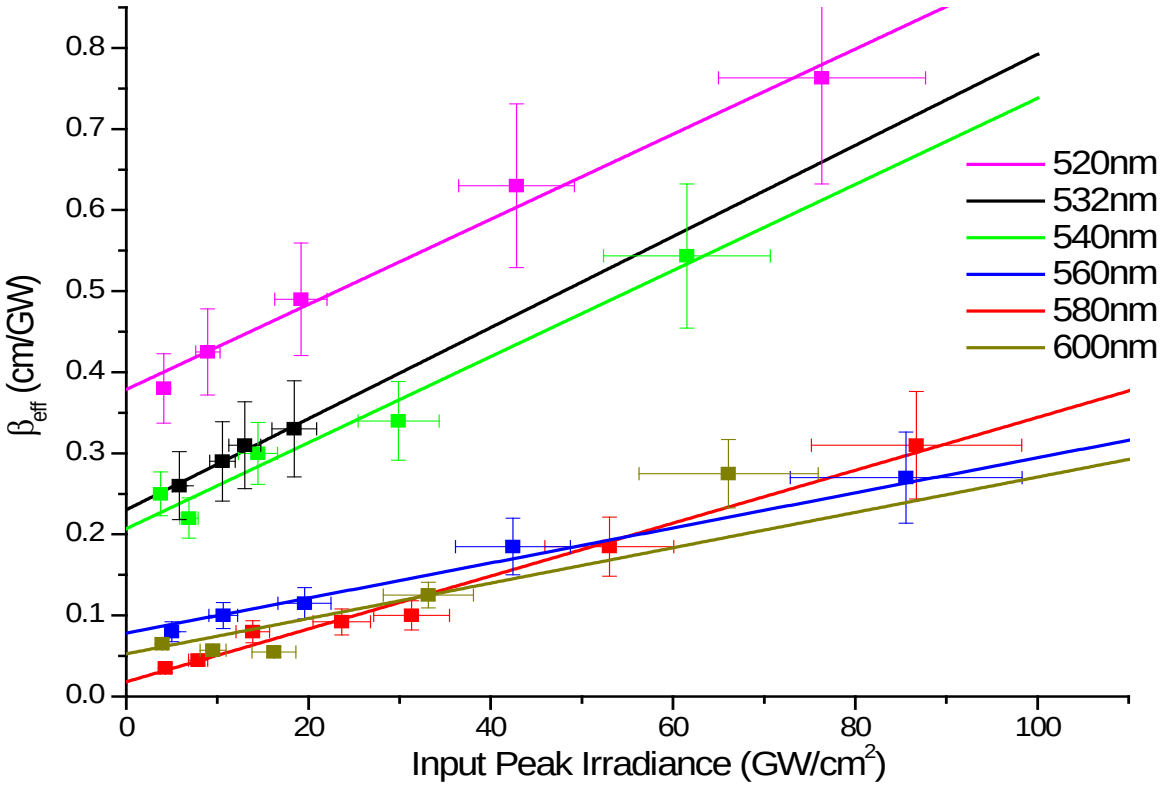

Figure 4.12: 140fs z-scan experimental results of the real part of the L34's nonlinear refractive index. Different wavelengths were examined.

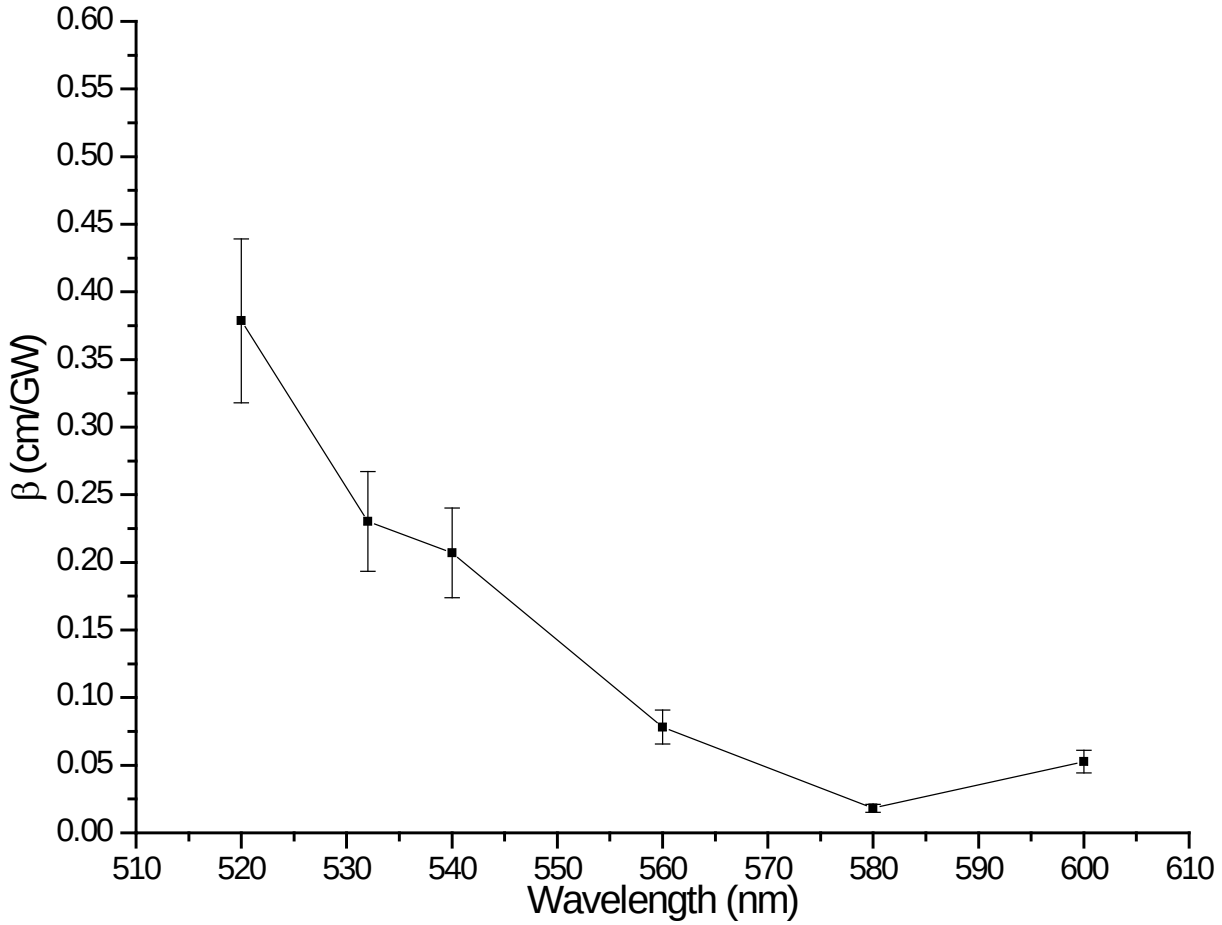

Figure 4.13: the analyzed result of effective nonlinear absorption coefficient for each wavelength from figure 4.12.

Clearly, the intrinsic TPA absorption coefficient of L34 is not a constant. Due to this fact, the calculated effective nonlinear absorption coefficient effective (β_{eff}) should also be evaluated point by point. As an illustration, a 10nm diameter silver nanoparticle is used in the simulation (Fig.4.14).

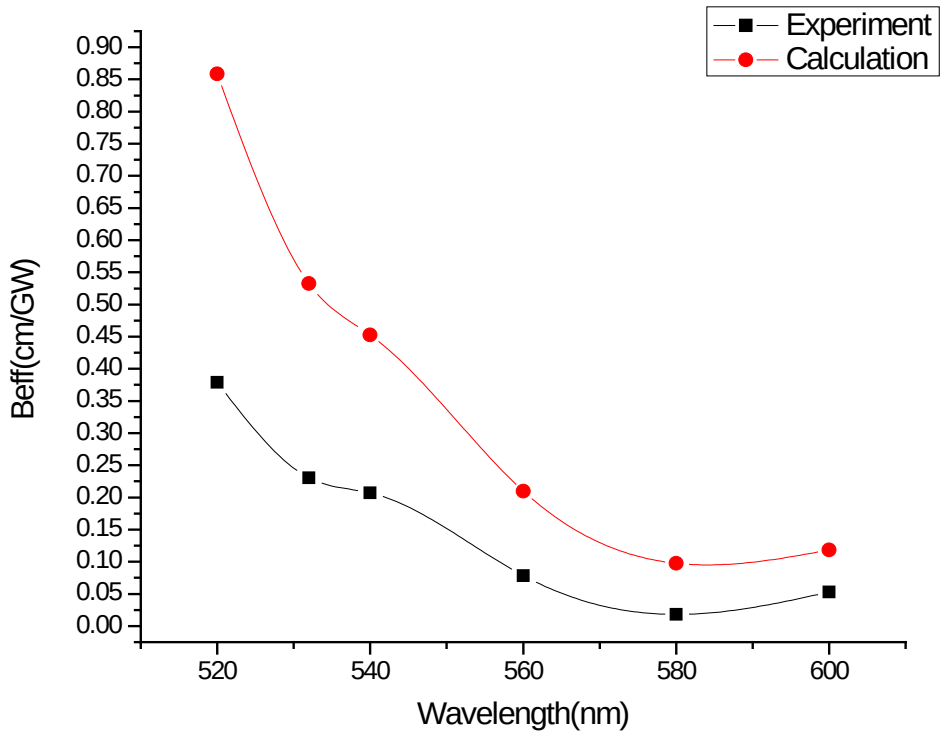

Figure 4.14: The new calculation result for effective nonlinear absorption coefficient for 10nm diameter silver nanoparticle in L34 based on the real experimental intrinsic TPA absorption coefficient value. Filling fraction is 0.5%.

Furthermore, these data can also be fitted using an exponential function. By using the fitted function, my goal is to predict the effective nonlinear absorption coefficient just below the resonance frequency. As shown in Fig.4.15, four different combinations have been chosen for simulation: L34 plus 2nm/5nm radius silver/gold nanoparticles with filling fraction 0.5%. The largest enhancement is obtained just below the resonance at 460nm. For the 5nm radius silver nanoparticle case, the enhancement factor is approaching 5.

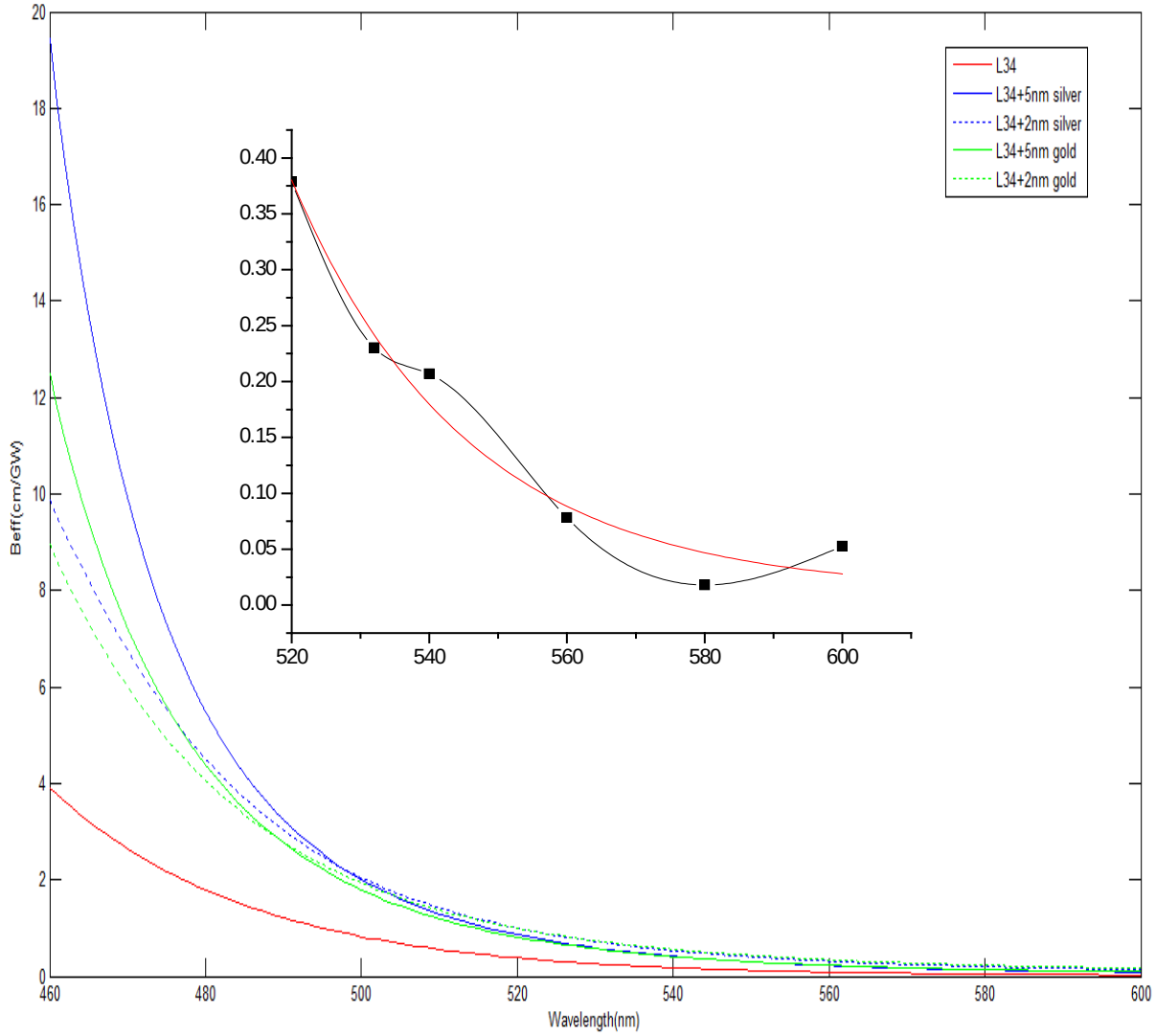

Figure 4.15: The exponential curve fitted simulation result for: L34 (red line) , L34+ 2nm radius gold nanoparticle (green dotted line), L34+ 5nm radius gold nanoparticle (green line), L34+ 2nm radius silver nanoparticle (blue dotted line), and L34+ 5nm radius silver nanoparticle (blue line) with filling fraction 0.5%.

Now, predictions of the effective nonlinear absorption coefficient changing trend for different wavelengths can be made based on the z-scan intrinsic TPA absorption coefficient result. At 460nm, for the 5nm radius silver nanoparticle with 0.5% filling

fraction, this TPA absorption coefficient is almost 5 times bigger than the pure L34 sample (from Fig.4.15).

4.4 Conclusion

Metamaterial is defined as: macroscopic composites having a manmade, three-dimensional, periodic cellular architecture designed to produce an optimized combination, not available in nature, of two or more responses to specific excitation [112]. The nanoparticles dispersed in NLC are a perfect combination for a metamaterial. The properties shown in this dissertation are quite different from those of natural materials, and of great current interest. By varying the parameters of this combination, e.g. the structure and the material, the dimension and filling fraction, the permittivity of the host medium and so on, it is possible to obtain a metamaterial with a tunable refractive index over a very broad wavelength region (from visible to IR). It has a dramatically increased birefringence for the index. It is defined as an ultra-nonlinear optical material with a tunable refractive index.

The effective nonlinear absorption coefficient changed by the nanoparticles dispersed into the nonlinear liquid has been studied as well. Although the experimental result of this effect is limited, certain valid simulations can be made. Notice that in this research the impact from a metal particle's nonlinear optical absorption is ignored. Further study on how to separate the impact from the absorption of metal itself and the enhanced absorption by nonlinear liquid is expected.

Chapter 5 Liquid Crystal Modulated Surface Plasmon Effect

The impact of liquid crystal on the LSPR effect is an important factor to be evaluated by researchers in the optical field. Generally speaking, liquid crystal is used to tune the peak position of the LSPR effect in order to make the resonance position suitable for the applications, e.g. optical switching.

In this chapter, the local electrical field enhancement and the sensitivity of the resonance peak position change due to the local refractive index difference have been calculated. The relationships between the inter-particle distance, particle aspect ratio, particle size and sensitivity will be investigated. Based on these, some SPP – liquid crystal applications are going to be introduced.

5.1 Introduction and Literature Review

The feasibility of using the LSPR effect in LC for the application of optical switching was first shown in Muller et al.'s paper [118]. Their conclusion of the feasibility was based on an experiment conducted by using a single gold nanoparticle. They embedded the gold nanoparticle into a LC cell coated with glass, and then used an applied external electric field to modulate the liquid crystal. A comparison was made between the scattering spectra with the electric field and without the field. According to the image from the scattering spectra, the researchers were able to measure the position of the peak to determine whether it was red-shifted or blue-shifted, corresponding to the wavelength which became larger or smaller. The result of this comparison showed that, with the help of the external field, the researchers were able to modulate the LC and then make the single gold nanoparticle's LSPR peak position of wavelength red-shifted for about one nanometer (nm). Later, Park and Stroud [119] used two physical approaches to calculate the

surface plasmon resonance peak position of gold nanoparticles embedded into a liquid crystal sample. They adopted both the Maxwell-Garnett mixing rule approximation and the discrete dipole approximation for simulation. These two simulation methods are commonly used by theoretical researchers in the physical-optical field. Both of the simulation results show that there is a splitting of the resonance wavelength. The distance between these two peaks is around one nm. These theoretical calculation results agree with the observation results from the experiment conducted by Muller et al. [118].

Since the discovery of this feasibility, the modulation of the LSPR effect using LC has attracted much interest from researchers. However, from the theory to the real application of the optical switching, there is still a long way to go. One problem involves the tuning range. According to Muller et al.'s [118] result, the tuning range for a single gold nanoparticle in liquid crystal is only one nm, which is equal to the resolution range of a super-resolution spectrometer. Under this configuration, a normal spectrometer without super-resolution cannot detect this small shift. For practical purposes, in order for most of the equipment to successfully detect the wavelength shift, a wider tuning range is needed.

To address this tuning range problem, several groups of researchers focused on the construction of the metallic structure; such as Kossyrev, Yin, Cloutier, and Cardimona [120], Chu, Chao, Chen, Wu, and Chen [121] and Hsiao, Zheng, Juluri, and Huang [122]. Moreover, based on the previous experimental results, Dridi and Vial [129] provided a general simulation model to describe the tuning effect of the plasmon resonance of the metallic nanostructures embedded in liquid crystals. They used the FDTD method to numerically calculate the LSPR peak position and developed a model for: $\lambda_{\max} = \lambda_0 + \Delta\lambda \sin^2\theta$, where the $\lambda_{\max}$ is the maximum wavelength of the tuning range, λ_0 is the starting wavelength, $\Delta\lambda$ is the tuning spectra and $\sin\theta$ is the rotational order of the LC molecule. This model linked the wavelength tuning range with the rotation of LC. Because $\sin\theta$ continues from 0 to

1, that means the rotation of the LC will continue. So as for the tuning effect, from zero to the maximum wavelength value, the tuning spectra will continue.

For the light wave propagation problems within liquid crystal devices, FDTD has already been shown to be a very practical tool [123,131]. In this section, a series of numerical calculations that also use FDTD will be conducted, based on a pair of silver nanocuboids dispersed into the nematic liquid crystal E7. The surface of the nanocuboid is assumed to be perfect, so the atomic roughness effect will not be considered [127]. Metal Nanocuboid particles have been synthesized and studied recently [124]. Two nanocuboids are put end-to-end to enhance the coupling strength in between. Compared to the nanospheres dimer [125, 126], the nanocuboid pair is more flat near the electric field enhancement during the entire gap.

5.2 FDTD Simulation of Silver Nanocuboid Pairs Embedded in Liquid Crystal

5.2.1 Two- Particle System Model

Similar to Ref. 126, a two-particle model for a pair of sliver nanocuboids can be derived. First, for the two- nanocuboid system: when the light is polarized along the inter-particle axis, the electrical field felt by each particle E' is:

$$E' = E + \frac{\mu'}{2\pi\varepsilon_m\varepsilon_0 d^3} \tag{5.1}$$

E stands for the electrical field of incident light and μ' is the electrical dipole moment. For a nanoparticle in an electric field E, $\mu' = \alpha'\varepsilon_m E$, the α' is the net of the Clausius-Mossotti dipole polarizability produced by the nanoparticles in this two-particle system. For an isolated nanoparticle, this polarizability in the quasi-static approximation is expressed as [126]:

$$\alpha = \varepsilon_0 V(1+\kappa)(\frac{\varepsilon - \varepsilon_m}{\varepsilon + \kappa\varepsilon_m}) \tag{5.2}$$

Here, V is the particle volume for the nanocuboid. Let l stand for the length of the long axis, and A be the area of the cross section. Then, $V = A*l$.

Another important factor to deal with is the shape factor κ. κ is directly related to the square of the nanocuboid aspect ratio (AR, the ratio between long axis and short axis) [128]. Then, let $\kappa = b*AR^2$ with an artificial coefficient b. Hence, $\kappa = b\frac{l^2}{A}$

The net polarizability α' of the two-particle system is given as [126]:

$$\alpha' = \frac{\alpha}{(1-\frac{\alpha}{2\pi\varepsilon_0 d^3})} \tag{5.3}$$

Plug in the expression of α ,then:

$$\alpha' = \frac{2\pi\varepsilon_0 b l^3(\varepsilon - \varepsilon_m)}{\varepsilon(2\pi\frac{\kappa}{1+\kappa} - b\frac{l^3}{d^3}) + \varepsilon_m(2\pi\frac{\kappa^2}{1+\kappa} + b\frac{l^3}{d^3})} \tag{5.4}$$

In a further derivation: define $s = d - l$ as the inter-particle surface-to-surface separation, then:

$$\varepsilon_{r|SP_{\max}} = -\varepsilon_m(\frac{2\pi AR^2(\frac{s}{l}+1)^3 + 1}{2\pi\frac{1}{b}(\frac{s}{l}+1)^3 - 1}) \tag{5.5}$$

Then, the effective shape factor for a two-nanocuboid system could be expressed as:

$$\kappa_{eff} = \frac{2\pi AR^2(\frac{s}{l}+1)^3 + 1}{2\pi\frac{1}{b}(\frac{s}{l}+1)^3 - 1} \tag{5.6}$$

The result for sensitivity is introduced as [126]: $S = \frac{d\lambda_{sp}}{dn_m} \propto \sqrt{\kappa_{eff}}$, where S denotes the sensitivity of the LSPR peak wavelength shift with the change of the refractive index of the surrounding medium, and κ_{eff} is the shape factor of the nanoparticle. In the case of liquid crystal, the sensitivity S is $S = S_\theta = \frac{\partial \lambda_{sp}}{\partial \theta}$ and $\lambda_{SP} = \lambda_0 + \Delta\lambda \sin^2\theta$ [129, 130].

Finally, an expression between $\Delta\lambda$ and the other parameters:

$$\Delta\lambda \propto \sqrt{\kappa_{eff}} = \sqrt{\frac{2\pi AR^2(\frac{s}{l}+1)^3+1}{2\pi\frac{1}{b}(\frac{s}{l}+1)^3-1}} \tag{5.7}$$

This equation sets up a relationship between the main parameters (AR, s) with the $\Delta\lambda$, or the sensitivity. With a fixed number of AR and b, if the inter-particle distance s is decreased, the coupling between these two nanocuboids is increased (i.e., the near field electrical field is enhanced). Therefore, the sensitivity increases near exponentially. Moreover, with the fixed number of separation distance s and the coefficient b, and under the condition that s is much smaller than the long axis l ($s \ll l$), the sensitivity is linearly increased with the aspect ratio increase. These statements will be all evaluated from the FDTD simulation results in section 5.2.3.

5.2.2 Description of the Method and Material Model

As introduced in section 3.3, FDTD is a widely used simulation method for spectroscopic studies in nanostructures. Several assumptions need to be made before the calculations: that the liquid crystal is perfectly lined up, easy to tune and the external electrical field is strong enough to tune the liquid crystal molecules.

Assume that the incident light is propagated along the z-direction and polarized along the x axis. The angle between the optical axis and the z axis in the x-z

plane is denoted by the angle θ. Then, the LC dielectric tensor expressed in the (x, y, z) basis will be [131]

$$\varepsilon = \varepsilon_0 \begin{pmatrix} n_o^2 \cos^2\theta + n_e^2 \sin^2\theta & 0 & (n_e^2 - n_o^2)\sin\theta\cos\theta \\ 0 & n_o^2 & 0 \\ (n_e^2 - n_o^2)\sin\theta\cos\theta & 0 & n_o^2 \sin^2\theta + n_e^2 \cos^2\theta \end{pmatrix} \tag{5.8}$$

The commercial nematic liquid crystal E7 is considered with ordinary refractive index $n_o = 1.53$ and extraordinary refractive index $n_e = 1.74$. The thickness of the LC layer is initially set to be 30nm.

The material model used for silver is the modified Debye model (MDM) for the broadband calculation of the FDTD program [100]. The frequency-dependent permittivity function of the MDM is shown as:

$$\varepsilon(\varpi) = \varepsilon_\infty + \frac{\varepsilon_s - \varepsilon_\infty}{1 + i\varpi\tau} + \frac{\sigma}{i\varpi\varepsilon_0} \tag{5.9}$$

where $\varepsilon(\varpi)$ is the complex relative permittivity, ε_∞ is the infinite-frequency relative permittivity, ε_s is the zero-frequency relative permittivity (static relative permittivity), τ is the relaxation time, σ is the conductivity and ε_0 is the permittivity of free space. The real model parameters used for the FDTD calculation are from Ref. 132.

The FDTD software employed in this work allows for the selection of different grid sizes for the different areas in the x,y,z directions ($\Delta x, \Delta y, \Delta z$). In the calculations, the grid size/mesh in the area between the two nanocuboids is set to be 1nm; the others are set to be 3nm. The absorbing boundary conditions (PML) are employed for all of the boundaries.

5.2.3 Results and Discussion

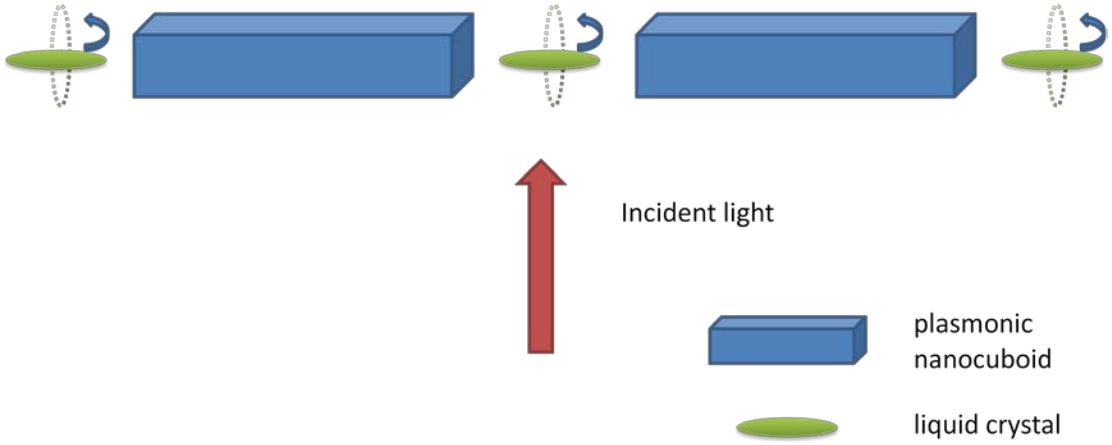

Figure 5.1: Illustration of a plasmonic nanocuboid pair embedded in nematic liquid crystal.

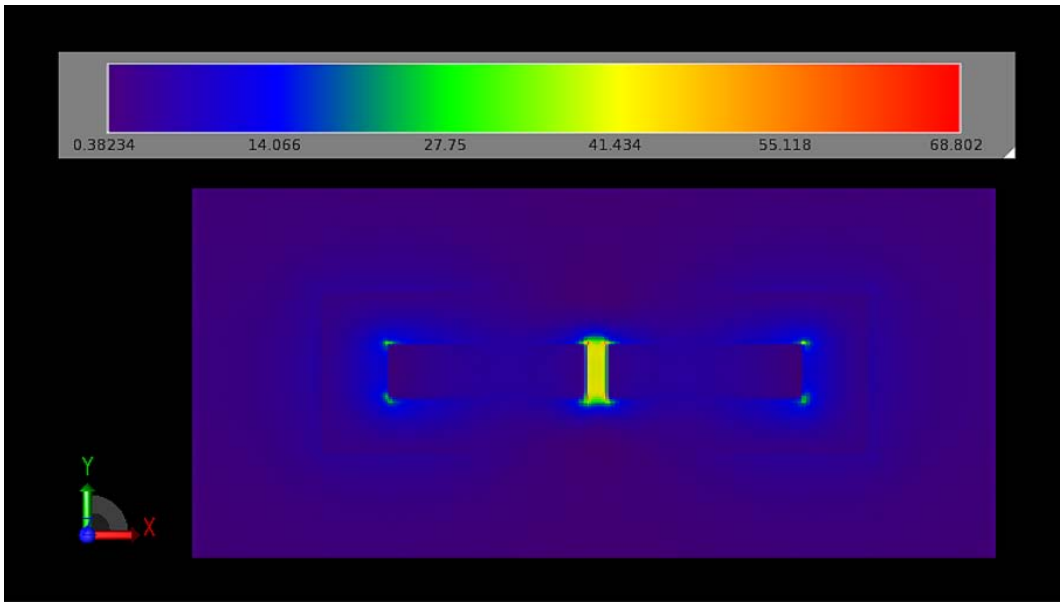

Figure 5.2: Spatial Distribution of the E-field near field enhancement of the nanocuboid pair

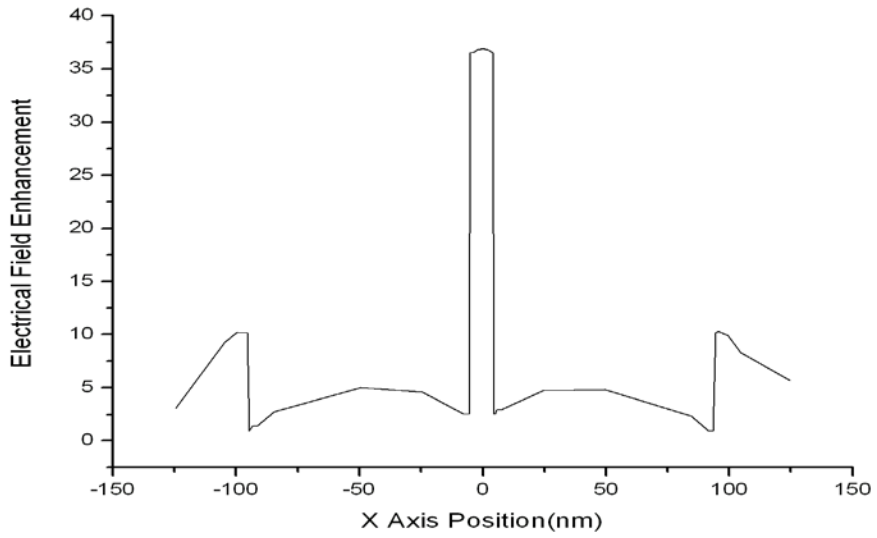

Figure 5.3: Horizontal cut of the calculated E-field Enhancement factor along Z= 0 such that the value along the X axis (axis connecting the two nanocuboids) is displayed

The light polarized along the axis of the two silver nanocuboids is shown in Figure 5.1. The inter-particle spacing between the two nanospheres was 9 nm. The E-field was determined at a steady state with an incoming sinusoid plane wave at 909nm wavelength.

The E-field enhancement of the two nanocuboids is shown in Fig.5.2 and Fig.5.3. The enhancement factor is defined as E_p / E_I, where E_p denotes the E-field strength at the position and E_I is the E-field strength of the incoming plane wave. The factor during the gap is almost the same, so I used the e-field strength of the middle point of the gap for further calculation. Instead of the sinusoid wave, a modulated Gaussian beam was used to excite all the frequencies. The LSPR peak was determined at the position where the electrical strength of the middle point reached the highest.

Effect of the liquid crystal thickness:

The method to evaluate the impact from each factor is very straightforward. A default value is set for each factor, and for every set of simulations, only one of the

factors can be changed. As the default, the separation distance is set at 9nm, with the size of the nanocuboid at 90nm*30nm*30nm. In the first set, the dependent of the surrounding medium liquid crystal's thickness is evaluated.

Thickness of liquid crystal(nm)	λ_0 (nm)	$\Delta\lambda$ (nm)
30	946	18.3
60	981	18.7
90	999	17.8

Table 5-1: Effect of the thickness of LC on the LSPR resonance peak position and sensitivity

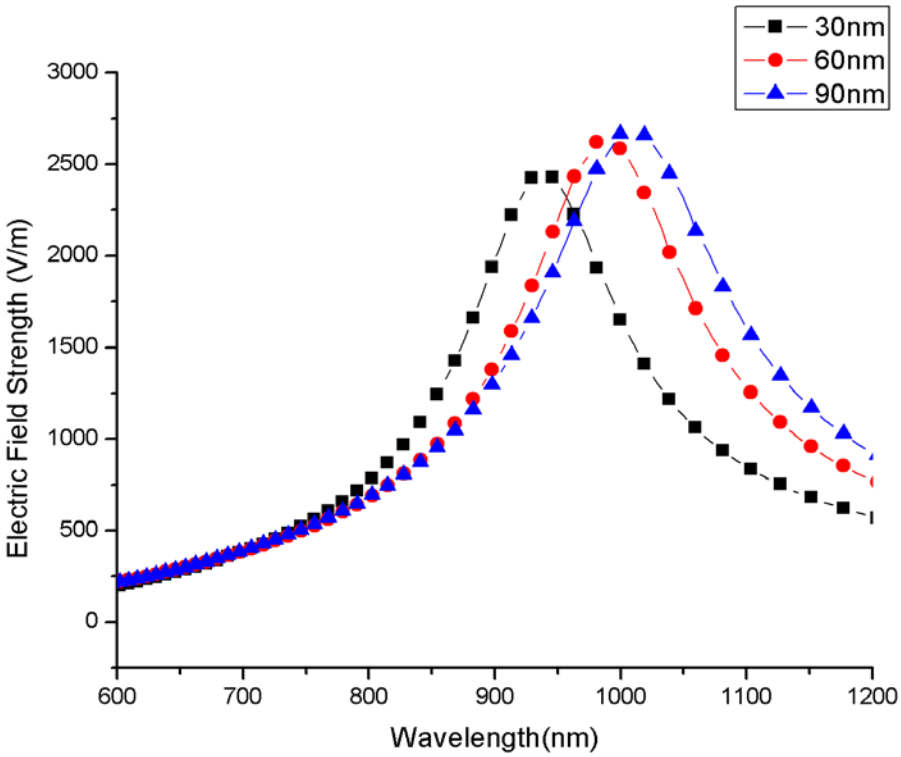

Figure 5.4: Change of the electrical field strength at the middle point of the gap due to the difference of the liquid crystal's thickness

Clearly, the peak position of the LSPR is red shifted with the increase of the thickness of the LC layer. In our field of interest, the sensitivity of the surrounding

medium change did not change much during the change of the thickness, and the resonance strength was almost the same.

Effect of the separation distance

If one fixes the geometry of the nanocuboid with 90nm*30nm*30nm and sets the thickness of the LC layer to be 30nm as the default number, then the separation distance of these two nanocuboids can be examined. The results are shown below:

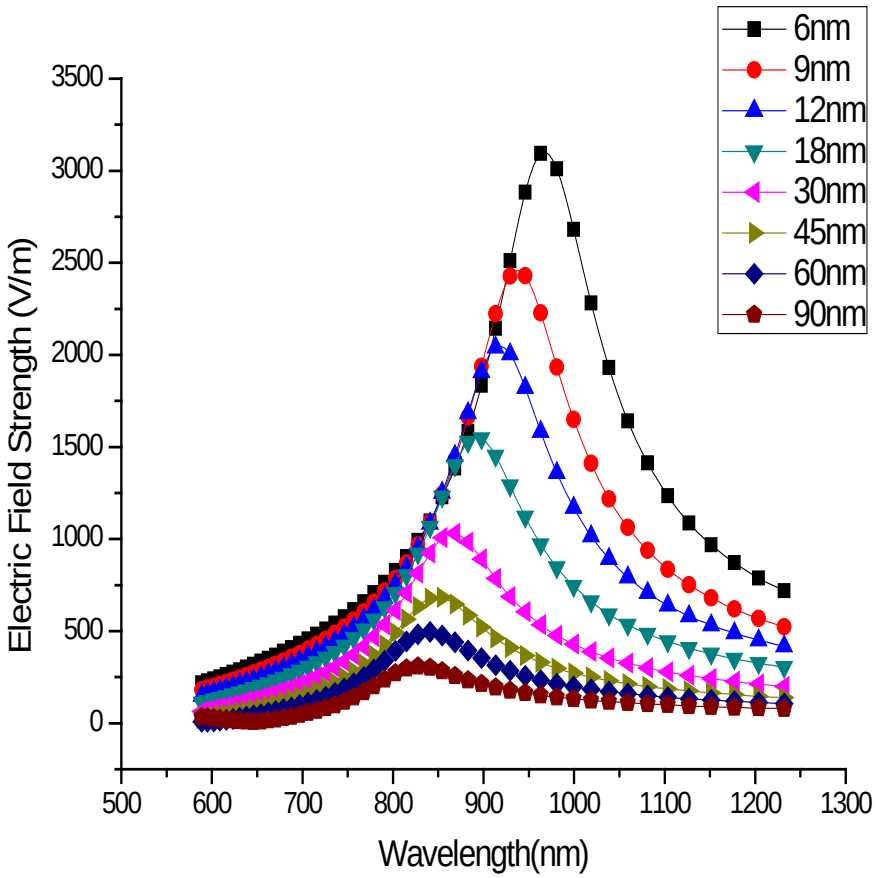

Figure 5.5 (a): Change of electrical field strength at the middle point of the gap due to the difference of the separation distance

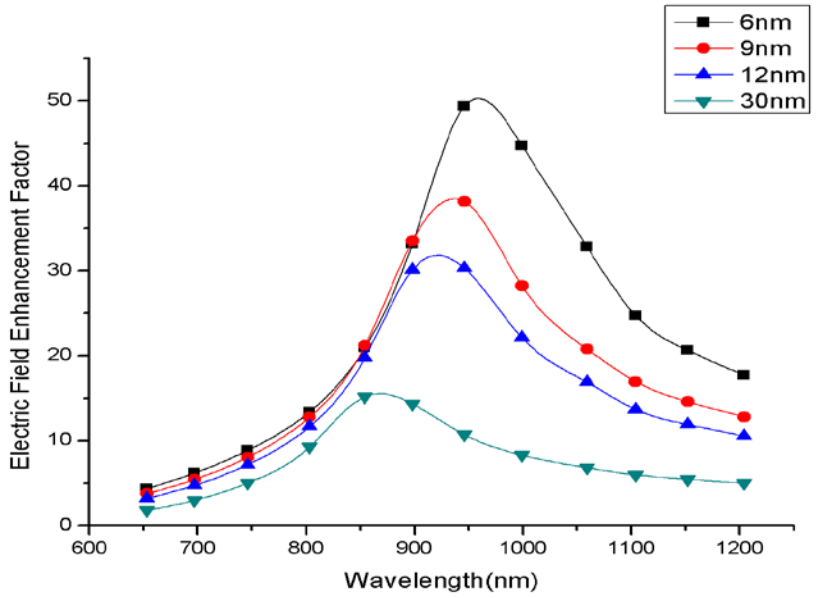

Figure 5.5 (b): Near field enhancement change due to the difference of the separation distance

Distance(nm)	λ_0 (nm)	$\Delta\lambda$ (nm)
6	963	18.9
9	946	18.3
12	913	17.0
18	898	15.4
30	868	14.0
45	855	13.6
60	841	13.2
90	828	12.9

Table 5-2: Effect of the different seperation distance on the LSPR resonance peak position and sensitivity

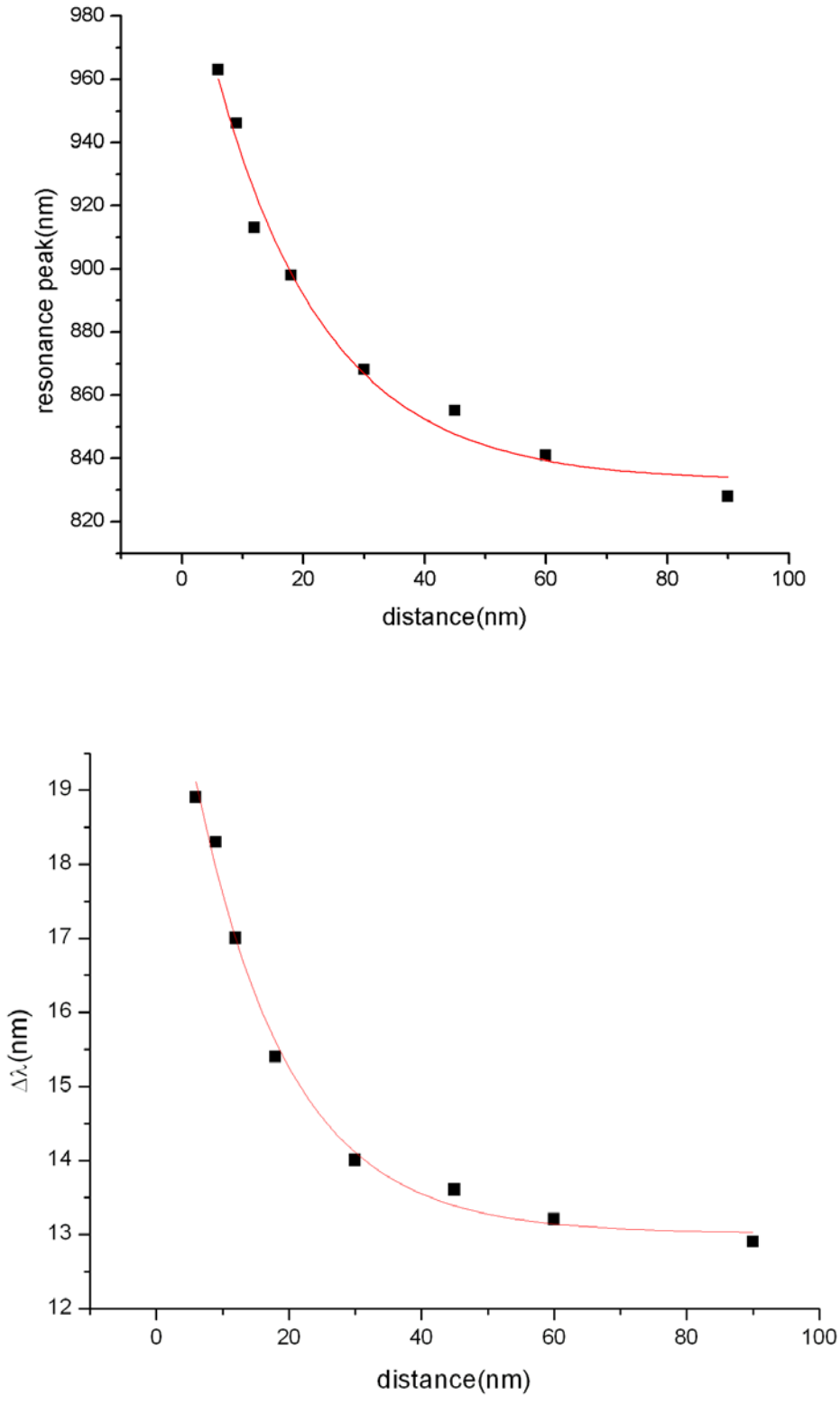

Figure 5.6: Exponential fit of the resonance peak position (Top) and the $\Delta\lambda$ (Bottom) vs. the separation distance of the nanocuboid pair

The liquid crystal molecule is several nanometers in length, so in this case the problem of nearly touching [133, 134] is ignored. Then, the smallest distance is set to be 6nm. From Figure 5.5, the e-field strength from the LSPR resonance increases as the separation distance becomes smaller. This results in the near-field electrical field enhancement where the impact from the coupling of the pair becomes much larger. As a result, from fig.5.6, the sensitivity has a near exponential increase with the decrease of the separation distance, which means that the medium has more influence on the LSPR in a strong coupling situation. One may think of this in another way: to increase the sensitivity, more coupling from the inter-particle is needed. In that case, the geometric resonance is considered and will be discussed in the next section.

Effect of aspect ratio:

Take the default value for the other factors: the separation distance is fixed at 9nm; the thickness of the LC is 30nm. And then take the aspect ratio as the variable:

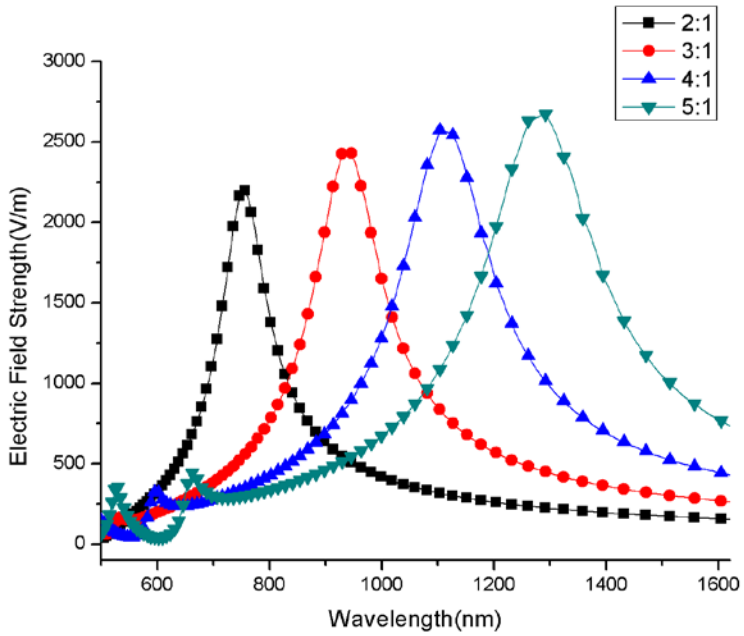

Figure 5.7: Change of the electrical field strength at the middle point of the gap due to the difference of the aspect ratio

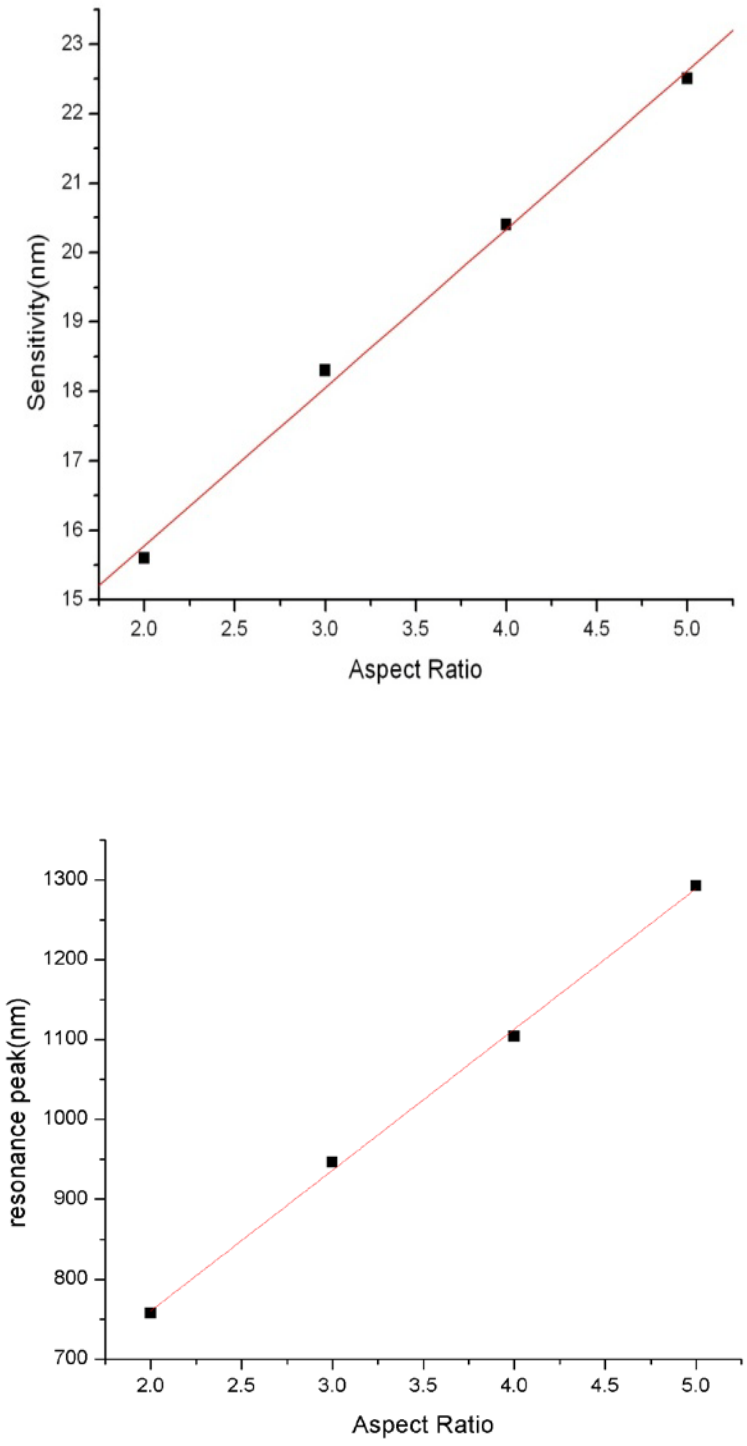

Figure 5.8: Top, linear curve fit of the sensitivity change vs aspect ratio. Bottom, linear curve fit of the resonance peak position change vs aspect ratio.

Aspect Ratio	λ_0 (nm)	$\Delta\lambda$ (nm)
2(60nm*30nm*30nm)	757	15.6
3(90nm*30nm*30nm)	946	18.3
4(120nm*30nm*30nm)	1104	20.4
5(150nm*30nm*30nm)	1292	22.5

Table 5-3: Effects of the different Aspect Ratios on the LSPR resonance peak position and sensitivity

From the results of Fig. 5.8, both the resonance peak position and the sensitivity are linearly increased with the increase of the aspect ratio. Simply, if a higher sensitivity is wanted, then the nanocuboids can be made larger in the longitudinal direction. However, when the nanostructure is larger, the spectrum of the LSPR will get broader (as in fig.5.7). That is a compensation to be considered.

Effect of cross section area:

The separation distance is set to be 9nm, and the thickness of the LC is 30nm, as before. Next, several different values of cross section area are considered.

Aspect Ratio	$\Delta\lambda$ (nm)	Aspect Ratio	$\Delta\lambda$ (nm)
2(30nm*15nm*15nm)	11.8	2(60nm*30nm*30nm)	15.6
3(45nm*15nm*15nm)	13.3	3(90nm*30nm*30nm)	18.3
4(60nm*15nm*15nm)	13.9	4(120nm*30nm*30nm)	20.4
5(75nm*15nm*15nm)	14.2	5(150nm*30nm*30nm)	22.5
6(90nm*15nm*15nm)	14.6		

Table 5-4: Effects of the different cross sections on the LSPR resonance peak position and sensitivity

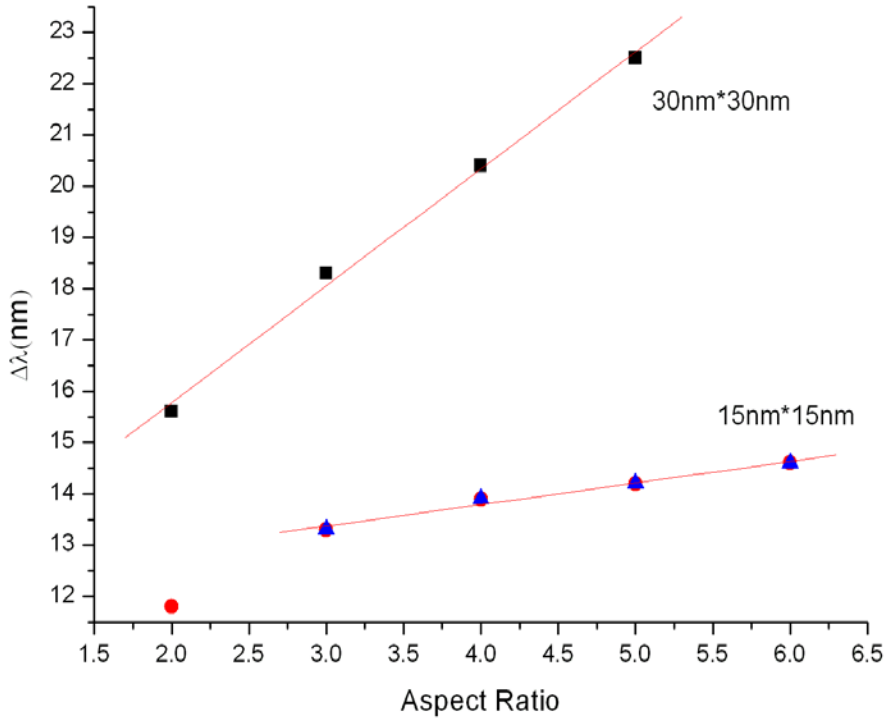

Figure 5.9: Linear curve fit of the sensitivity change vs aspect ratio and change of size.

As the area of the cross section decreases, the sensitivity value will decrease. For each cross section area, the effect is still linear, as discussed in figure. 5.8. Notice only the red point is off the line. That is because the value of the long axis (30nm) is not much greater than the value of the separation distance (9nm). In this case, for the shorter nanocuboid the so-called end cap effect [135] will need to be considered. In other words, a bigger sized (30nm or above) nanoparticle or nanostructure is preferred. A detailed summary of all the factors is given in section 5.4.

5.3 Liquid Crystal- SPP applications

In the previous section, I researched the properties of a LSPR- liquid crystal device. By using all of the analyzed relationships, researchers can design the SPP applications accordingly. Recently, I collaborated with two groups to do the design and experiments of the applications. In this section, I am going to review some of our published work in order to give a general idea about the liquid crystal-SPP devices.

1. High contrast modulation of plasmonic signals using nanoscale dual-frequency liquid crystals [136]

In ref. 136, we showed that by modification of the surface plasmon polariton wave, a novel design of a high contrast modulator can be achieved. The physical principle of the design is:

We have a groove-slit design of the geometry structure. The SPP wave is generated by diffraction through a slit on a silver film, and the SPP wave is travelling at the silver/dielectric boundary. Consider this dielectric environment is liquid crystal, and then the SPP wave propagates over a region embedded with LC whose phase is controlled by the LC molecules. At the output point of the SPP wave, let another beam (input beam with optical pump- 1 groove slit design or another SPP wave- 2 groove slit design) interfere with it, and we measured the interference signal's intensity at an observation point. By using the electro-optic effect of liquid crystal (as discussed in section 2.3), the phase of the SPP wave will be modulated, and then the interference can be constructive or destructive. The contrast between the output signals is achieved by varying the dielectric anisotropy of the LC, which is conveniently accomplished through an applied voltage [136].

In order to get a high contrast modulator, the change of the dielectric anisotropy should be larger. In this way, the Dual Frequency Liquid Crystal (DFLC) is considered (concepts of DFLC are expressed in section 2.2 in this dissertation).

Other work on SPP-liquid crystal applications using DFLC can be found in ref. 139,140.

Some simulation results are shown in Figure 5.10-5.12.

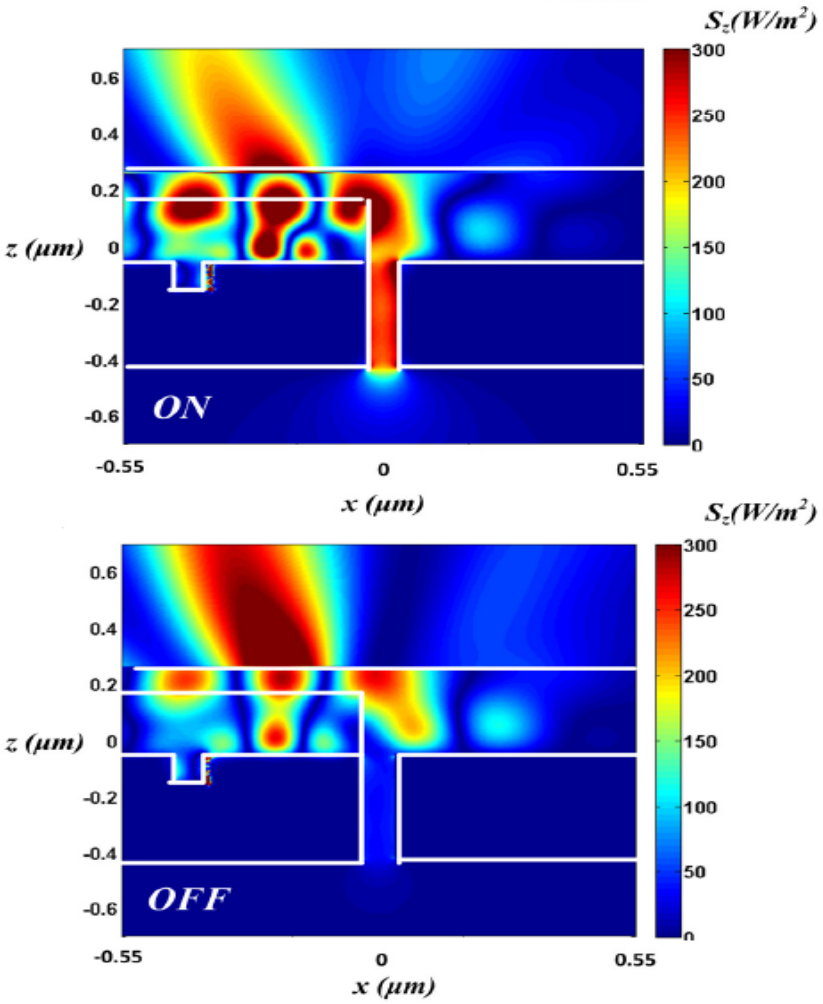

Figure 5.10: Field intensity plots for 1-groove, 1-slit device in the (Top) ON state and (Bottom) OFF state. The relative magnitude of the Poynting vector is shown against the two-dimensional geometry of the device. [136]

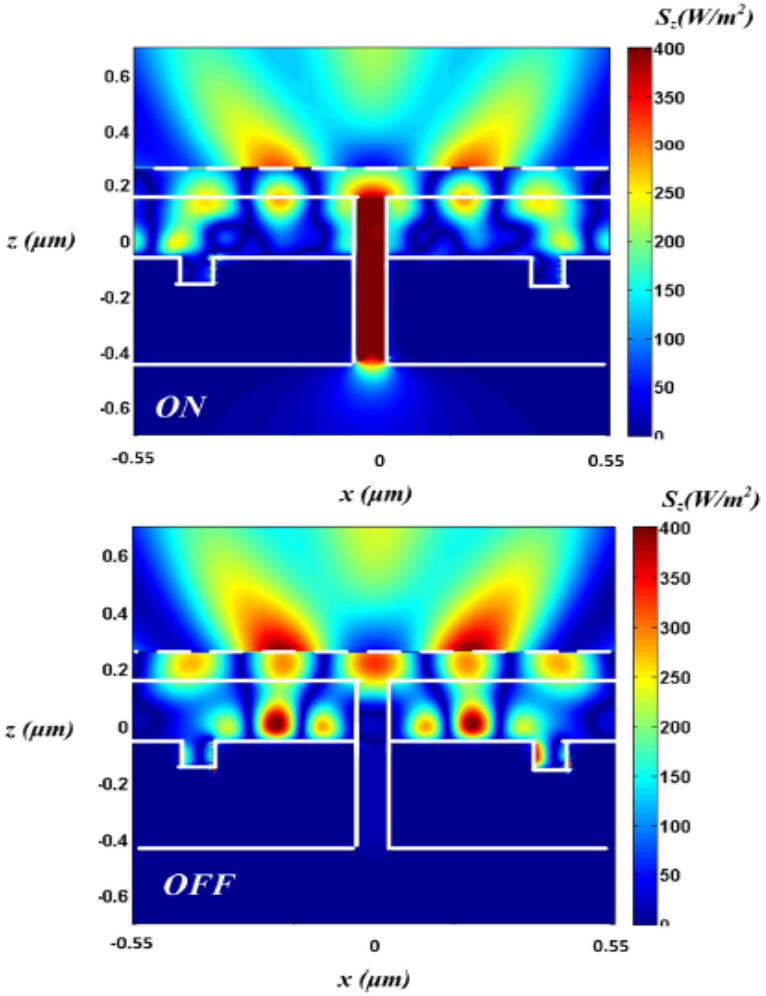

Figure 5.11: Field intensity plots for 2-grooves, 1-slit device in the (Top) ON state and (Bottom) OFF state. The relative magnitude of the Poynting vector is shown against the two-dimensional geometry of the device. [136]

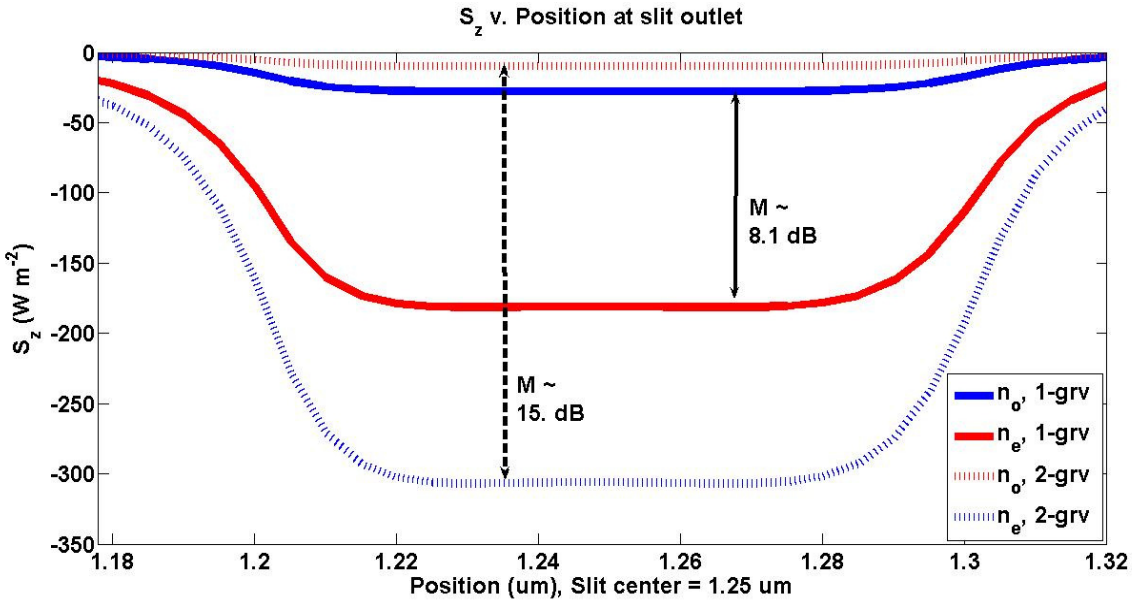

Figure 5.12: Intensity contrast for 1-groove and 2-groove devices. The contrast of the 2-groove device is ~15 dB whereas the 1-groove device exhibits contrast of ~8.1 dB. [136]

2. Light-driven tunable dual-band plasmonic absorber using liquid-crystal-coated asymmetric nanodisk array [137]

In our lab's previous work, we have already researched and experimentally showed [139,140] that liquid crystal's electro-optical effects are very useful in controlling the refractive index for SPP modulation. Also, liquid crystal can be modulated using laser light by doping certain dye, e.g. Methyl- red [17, 46].

In Ref. 137, our collaborator designed a nanodisk array pattern which has a unique property as a perfect absorber (a modified pattern is used for this work as in Figure 5.12) [137, 141]. Dye-doped nematic liquid crystal was put on top of the array. The laser induced reorientation effect of the liquid crystal is employed. Nematic liquid crystal 5CB [17] is used where n_e-1.63, n_o-1.50 and n_{iso}-1.54. In the experiment, a change in the amount $\Delta n \sim 0.06$ [from 1.61 to 1.56] was observed [137], which corresponded to about 30nm of the localized surface plasmon resonance peak position change in the simulation.

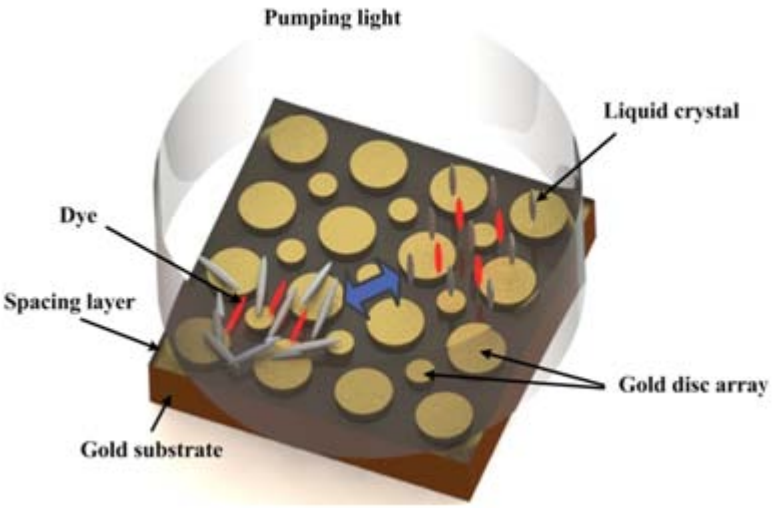

Figure 5.13: Schematic of light-driven tunable plasmonic absorber. Light-sensitive liquid crystals on top of the absorber can be modulated with light. [137]

Some experimental results are shown in Figure. 5.14.

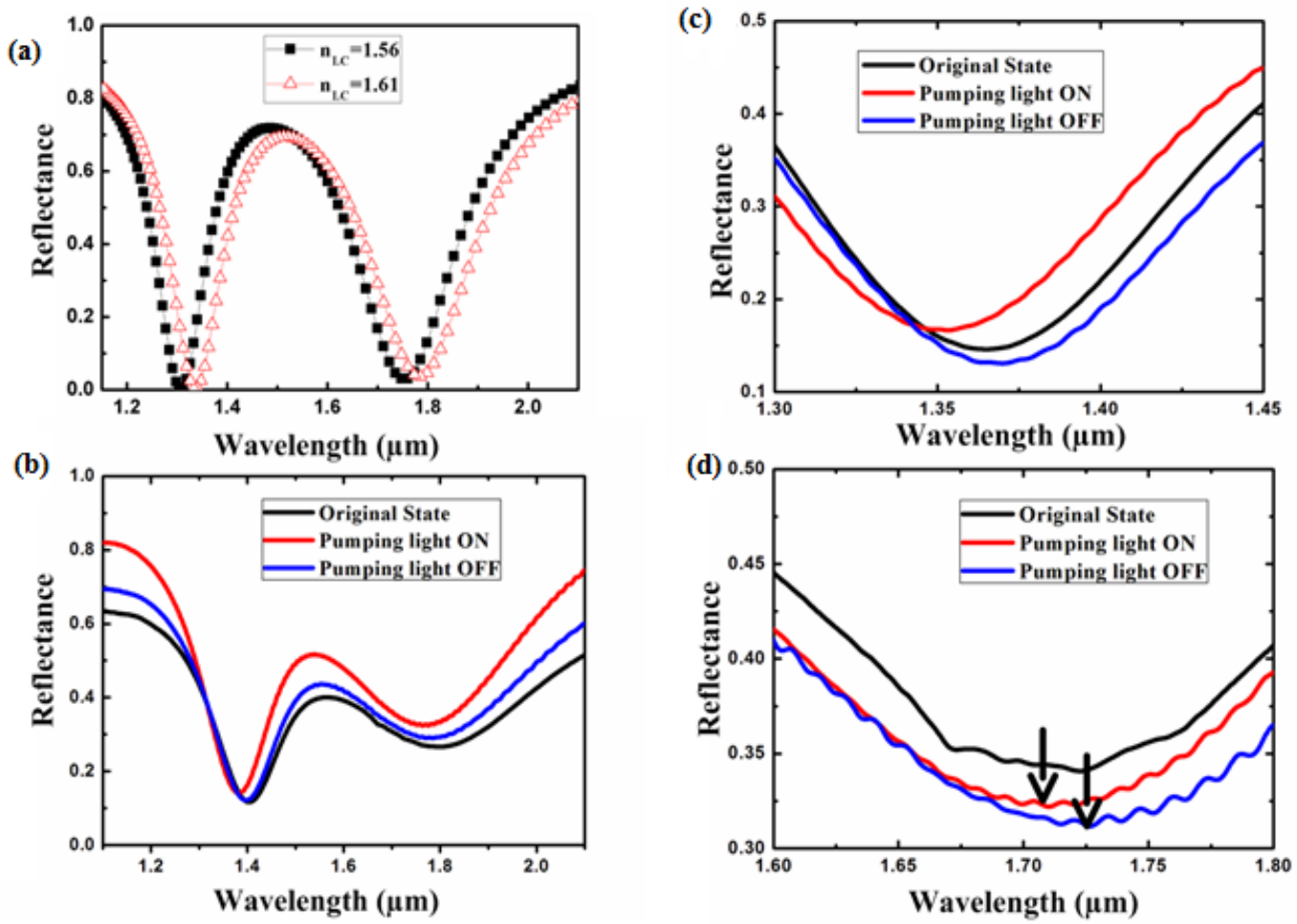

Figure 5.14: (a) FDTD-simulated results of the performance of the Liquid crystal-plasmonic absorber. Around 30 nm shift can be observed. (b) Measured absorption band shifts with the pumping light turning ON and OFF. (c) Zoom-in view of the left absorption dip. The shift is around 25 nm. (d) Zoom-in view of the second absorption dip. The shift is around 20 nm.[137]

The problem with this work is that the tuning range is not very big. To be more useful in practical applications, several factors should be considered for optimizing: the geometric structure, dye-concentration and other liquid crystals with larger refractive index birefringence [137].

3. Large spectral tunability of narrow geometric resonances of periodic arrays of metallic nanoparticles in a nematic liquid crystal

In section 3.2.3, I introduced the concept of geometric resonance. This special effect has some advantage over the LSPR effect, which I described before. Also, regarding the limited tuning range problem that happens for most of the LSPR-liquid crystal device, the geometric resonance- liquid crystal device has the largest tuning range among all of the designs up to now. “The resonance shifts can be as high as 100 nm, leading to higher sensitivity when the system is used for sensing or switching operations.” [138]

In this work, we have the following geometric design: [138]

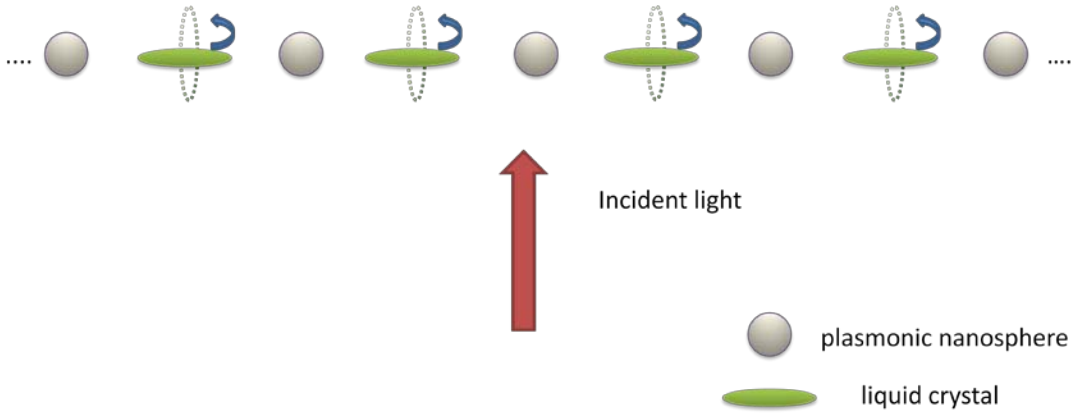

Figure 5.15: Illustration of a one dimensional periodic array of gold nanoparticles embedded in a nematic liquid crystal.

Compared with the nanocuboid pairs researched in section 5.2, the geometry of the design is similar, as shown in Figure 5.1. The only difference is that in this work the nanoparticles are in an array which contains only 400 particles in order to create the geometric resonance [90,138].

By using the same method as in section 5.2, the tuning range of the GR by liquid crystal can be calculated. In the paper Ref. 138, our collaborator used the “semi-analytical coupled dipole method”, which is also known as the DDA method mentioned in section 3.3. This method gives the calculation result with the precise line width of each resonance, which is very narrow. For other methods, such as FDTD,

due to the nature of the calculation software, it can be used to calculate the position of each GR resonance peak position. But, the band width for each resonance will have some errors. The main problem with DDA is, one needs to make an assumption that "the anisotropic LC is approximated as an isotropic medium with a fitted refractive index" [138]. So, to check the change of the calculation for the resonance peak position due to the assumption, I used the FDTD method, which can be used for the anisotropic medium liquid crystal. The result is shown in Figure 5.16:

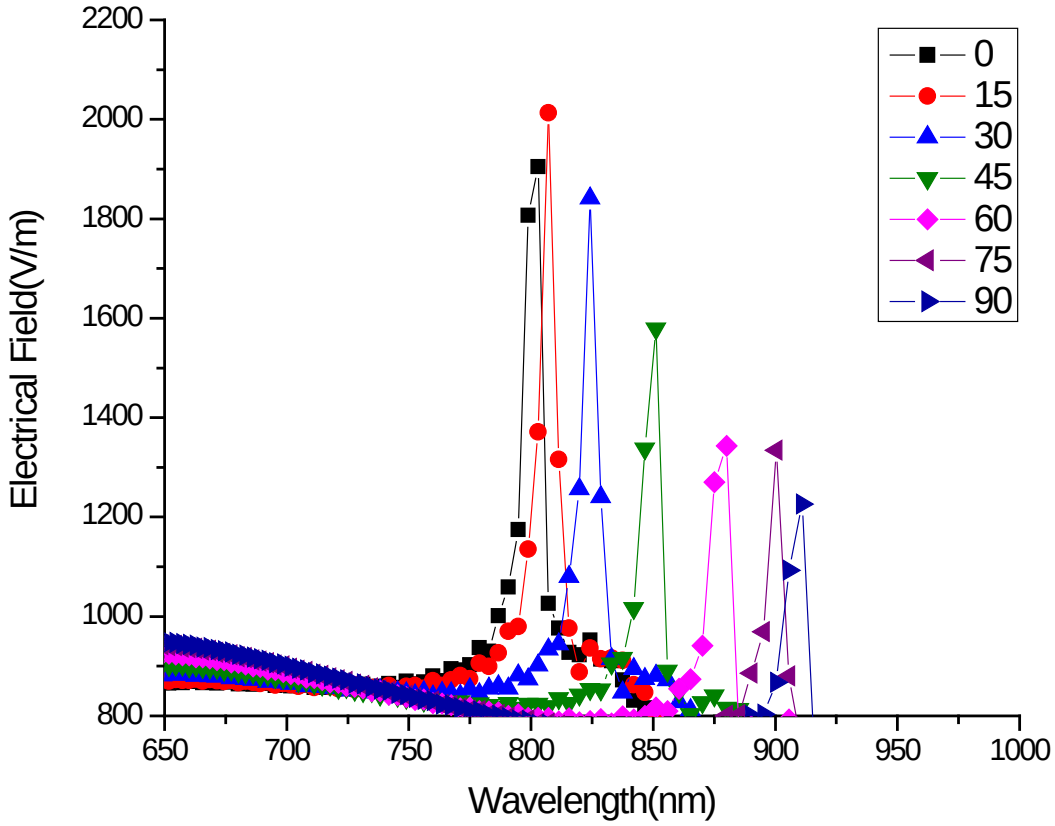

Figure 5.16: FDTD calculation of a periodic array of gold nanoparticles embedded in LC. The radius of the nanoparticle R=50nm; inter-particle spacing d=520nm. The configuration of the design is the same as in ref. 138.

The calculated peak position for each resonance is shown in Table 5.5.

Rotation (degree)	Wavelength(nm)
0	802.9
15	807.1
30	824.2
45	851.2
60	880.0
75	900.4
90	910.9

Table 5-5: GR resonance peak position vs. Rotation degrees of liquid crystal

Compared with the DDA calculation result shown in Figure 5.17 [138], clearly, the peak position is almost the same for both of the methods. In this way, we can have a conclusion that the assumption made in this paper is valid. Notice, this assumption is based on the fact that this design structure is a 1-dimention array. If one has a 2-dimention array, then the assumption should be further reviewed. Also, for the FDTD result, the major shortcoming is the limitation of the mesh size and calculation time. Due to the finite limitation of the computer's memory, the boundary condition of the FDTD program is set to be periodic. This condition varies based on what software is used, so the bandwidth result may not be the same as in Fig. 5.16. But, the position of each resonance peak should be the same.

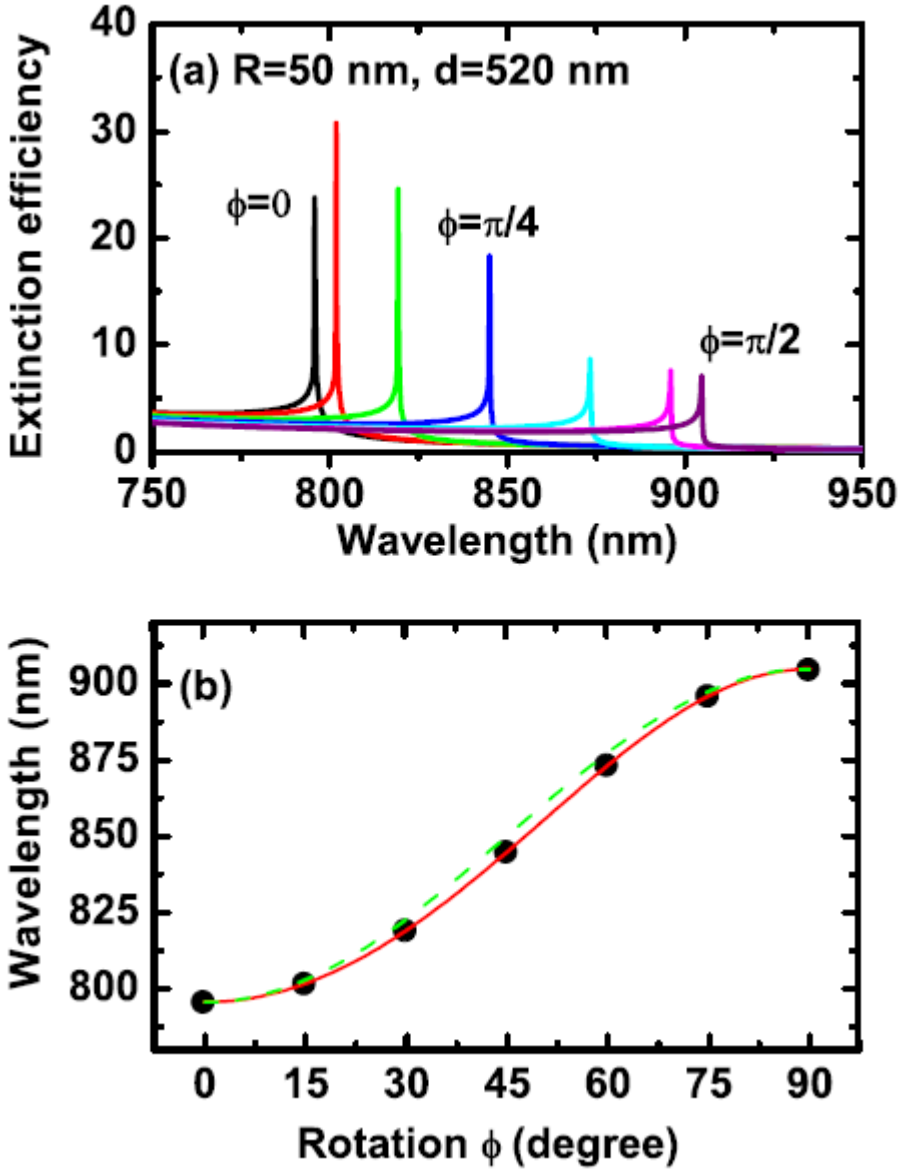

Figure 5.17: (a) Extinction spectra of the periodic arrays of gold nanoparticles embedded in LC. (b) The dots are GR wavelengths extracted from (a). The curves are the analytical models of the GR wavelengths.[138]

Also notice, this GR resonance peak position will not be influenced by the different materials of the metal, e.g. changing gold to silver. Figure 5.18 shows a calculation result using silver nanoparticles.

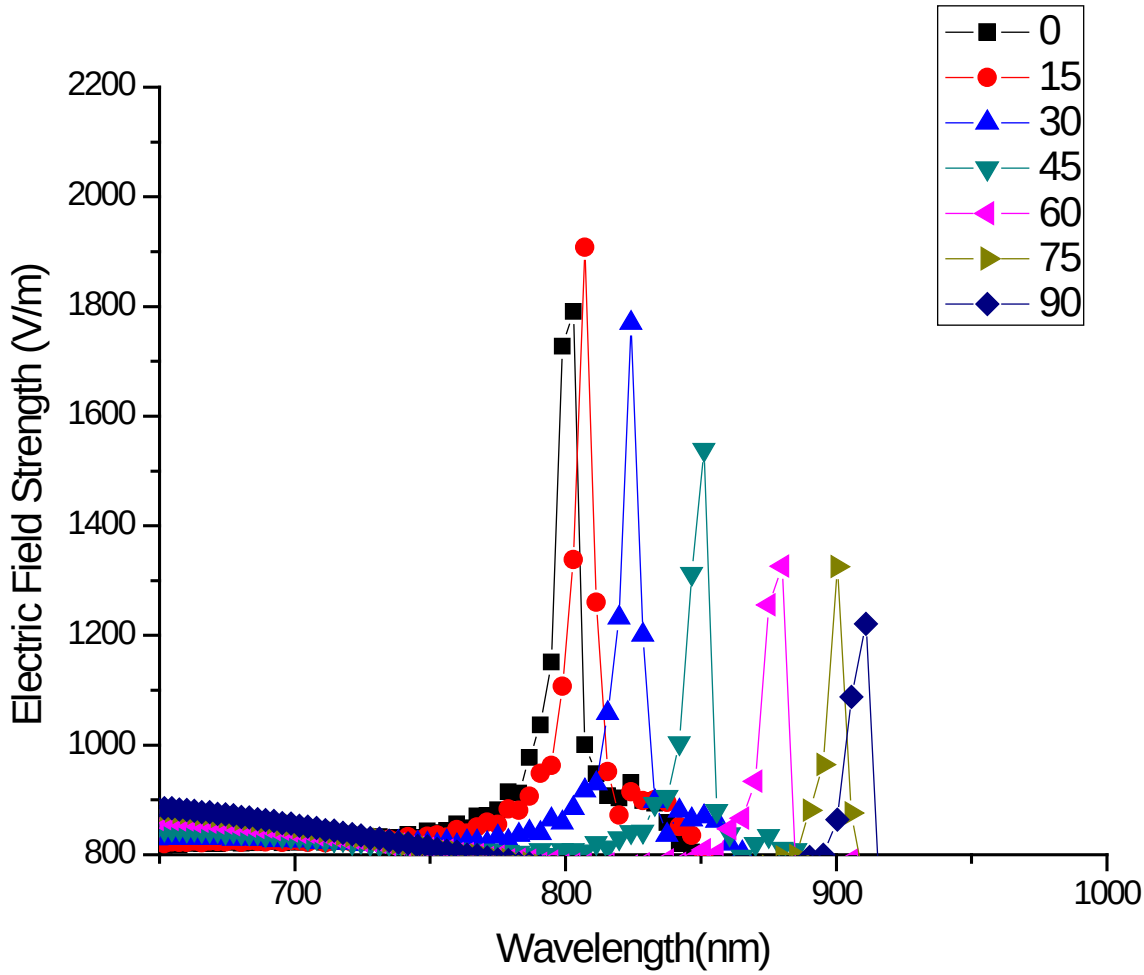

Figure 5.18: FDTD calculation of a periodic array of silver nanoparticles embedded in LC. The radius of the nanoparticle R=50nm; inter-particle spacing d=520nm.

The resonance peak position for silver in Fig. 5.18 is exactly the same as in Fig. 5.16 for gold nanoparticles. That is another difference between the GR and LSPR-liquid crystal effect. Basically, the spectral tunability is about 100 nm for GR. We believe that this simple 1-D periodic structure will have important applications for the fields of optical sensing and switching [138].

5.4 Conclusion

In this chapter, several key factors that affect the sensitivity of a coupled silver nanocuboid pair dispersed in a liquid crystal layer were examined: the separation distance between the nanocuboids, the aspect ratio and the size for the nanocuboid. The feasibility of using liquid crystal shows that one can easily tune the refractive index of the surrounding medium and achieve a tunable near field electrical field enhancement. This possibility is of particular interest for experiments such as the surface-enhanced Raman spectroscopy, as it may help the researcher get the best enhancement factor that they want [11]. Also, by using the relationship between the factors and the sensitivity, a way to modify the nanostructure for future experiments is provided.

Later, three of our collaborated works which involve the novel design of liquid crystal- plasmonic devices are listed. These applications contain all of the three aspects of the surface plasmon effect: surface plasmon polariton in application one, localized surface plasmon resonance in application two, and geometric resonance in application three. I focused on the liquid crystal part in which I was involved. Other aspects, e.g. the fabrication of the nanostructure and the experimental design are ignored. The purpose for introducing these applications is to show the importance of the liquid crystal- plasmonic study, and the bright possibilities for future use.

Chapter 6 Future Work and Summary

6.1 Future Work

6.1.1 Nanoparticle + Nonlinear liquid

In section 4.4, I already noted that the impact from the metal particle's nonlinear optical absorption is ignored. Further study about how to separate the impact from the absorption of the metal itself, and the enhanced absorption by nonlinear liquid, is needed.

Also, this work is based on the z-scan result from femto and pico-second lasers. For a longer pulse, e.g. a nano-second, this effect becomes very complicated, as demonstrated in Figure 6.1:

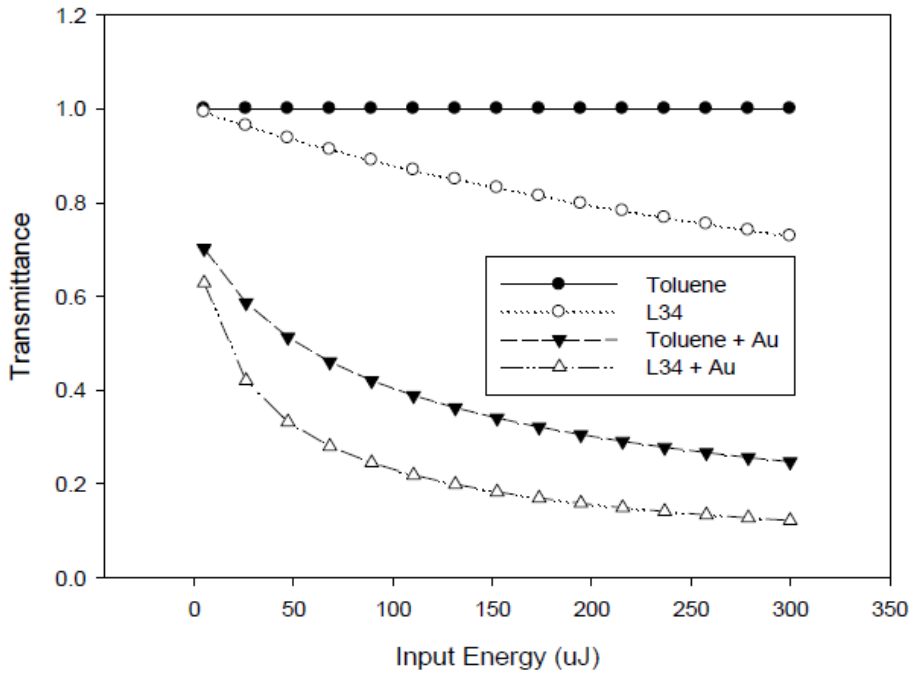

Figure 6.1: Laser parameters: λ= 532 nm, pulse duration: 1 ns; focused spot diameter: 0.5mm. Sample: 1 mm thick cell filled with 70 % linear transmission nm-Au doped L34 and toluene, pure toluene and L34.[114]

Notice: from the pure Toluene to the Toluene + Au curve, the transmittance drops a lot due to the limitation of the nanoparticles. It is still being researched whether this optical limiting effect is from the scattering of the nanoparticles or the nonlinear absorption. The role of the nanoparticles in this nano-second experimental result cannot simply use the same technique for analysis as I did in section 4.3. Further study of the nonlinear refractive index of the metal nanoparticle interaction with L34 should be conducted.

Moreover, in L34 there is not only the two photon absorption (TPA) effect, but also the excited state absorption (ESA) effect [113]. The ESA effect is enhanced due to the near field enhancement by the nanoparticles as well. I was able to ignore the ESA effect for the ultra-short pulse in section 4.3. However, future work involving longer pulse results (Fig.6.1) should also consider this factor.

6.1.2 Further Notes about Geometric Resonance

In section 5.3, I introduced our work on the geometric resonance tuning, the tuning range of which is as high as 100nm. This is the highest tuning range we could have among all of the designs using LSPR. But, the problem is that this design is only one-dimensional. Two-dimensional semi-analytical models, including the anisotropic liquid crystal medium, should be further developed. Also, other FDTD software may give better results for the line width for the 1-D or 2-D case. A two-dimensional tuning of the geometric resonance is expected, e.g. ref. 142. Also, in ref.142, the researchers listed the experimental observation results of the geometric resonance in water. The same measuring technique can be applied to liquid crystal. This may lead to the experimental results from using the electro-optics effect of liquid crystal to monitor the refractive index.

6.2 Summary

As mentioned in the first chapter of this dissertation, the interaction between the surface plasmon resonance effect and the liquid crystal material has been studied throughout the dissertation. The impacts from each side were expressed separately in chapter 4 and 5. The nanoparticle dispersed liquid crystal or nonlinear liquid, and the liquid crystal tunable localized surface plasmon resonance were the two main topics.

Regarding these topics, this dissertation is focused more on the concepts and the fundamental physical property aspects. The actual designs of the applications are discussed in section 5.3. Because of the difficulty of the nanofabrication technique, these applications may not be the same as the other liquid crystal devices, e.g. retarder or shutter, which can be mass manufactured. But the importance of the research does not need to be addressed. Every application I described here in this dissertation is just an example of the many ideas we have. Continued research on the liquid crystal-plasmonic field with my co-workers is still being conducted.

Reference

1. S. A, Maier, “Plasmonics Fundamentals and Applications”; Springer: New York, (2007)

2. S. A, Maier, M. L.,Brongersma, P. G, Kik, S.,Meltzer, A. A. G. Requicha and H. A. Atwater, “Plasmonics—A Route to Nanoscale Optical Devices” , AdV. Mater. 13, 1501 (2001)

3. A. J. Haes, W. P. Hall, L. Chang, W. L. Klein and R. P. Van Duyne, “A Localized Surface Plasmon Resonance Biosensor: First Steps toward an Assay for Alzheimer's Disease”, Nano Lett. 4, 1029 (2004)

4. Y.W.C. Cao, R.C. Jin, and C.A. Mirkin, “Nanoparticles with Raman Spectroscopic Fingerprints for DNA and RNA Detection”, Science 297, 1536 (2002)

5. C.F. Bohren, D.R. Huffman, “Absorption and Scattering of Light by Small Particles”, Wiley, New York, (1983)

6. U. Kreibig, M. Vollmer, “Optical Properties of Metal Clusters”, Springer, New York, (1995)

7. M. L. Brongersma, P. G. Kik,, “Surface Plasmon Nanophotonics”; Springer: New York, (2007)

8. S. Link, M. B. Mohamed, and M. A. El-Sayed, “Simulation of the optical absorption spectra of gold nanorods as a function of their aspect ratio and the effect of the medium dielectric constant”, J. Phys. Chem. B, 103, 3073 (1999)

9. K. L. Kelly, E. Coronado, L. L. Zhao and G. C. Schatz, “The Optical Properties of Metal Nanoparticles: The Influence of Size, Shape, and Dielectric Environment”, J. Phys. Chem. B 107, 668 (2003)

10. H. Ibn El Ahrach, R. Bachelot, A. Vial, G. Lerondel, J. Plain,P. Royer and O. Soppera, “Spectral degeneracy breaking of the plasmon resonance of single metal nanoparticles by nanoscale near-field photopolymerization”, Phys. Rev. Lett., 98, 107402 (2007)

11. S. Franzen, “Intrinsic Limitations on the |E|4 Dependence of the Enhancement Factor for Surface-Enhanced Raman Scattering”, J. Phys. Chem. C 113, 5912 (2009)

12. A. Diaz, Y. Ma, J. Huang, J. Liou, J. H. Park and I. C. Khoo, “Refractive index engineering of liquid crystals with nano-particulates”, Proc. of SPIE Vol. 7050 13-3 (2008)

13. F. Reinitzer, "Beiträge zur kenntniss des cholesterins," Monatshefte für Chemie, vol. 9, pp. 421-441 (1888)

14. I. C. Khoo, “Liquid Crystals: Physical Properties and Nonlinear Optical Phenomena”, Wiley-Interscience, New York, NY, (1995)

15. I. C. Khoo, and A. Diaz, “Nano-spheres dispersed liquid crystal supra-nonlinear negative-zero-positive index Metamaterials”, Proc.of SPIE, Vol.6470 (2007)

16. I. C. Khoo, and J. Ding, “All-optical cw laser polarization conversion at 1.55 micron by two beam coupling in nematic liquid crystal film”, Apply. Phys. Letters, 81, pp.2496-2498 (2002)

17. I.C. Khoo, “Liquid Crystals”, 2nd edition, Wiley, NJ (2007)

18. Figure is from Dissemination of IT for the Promotion of Materials Science, University of Cambridge, UK
http://www.doitpoms.ac.uk/tlplib/anisotropy/liquidcrystals.php

19. V.G. Chigrinov, “Liquid Crystal Devices: Physics and Applications”, Artech House Optoelectronics Library (1999)

20. V.I. Kopp, B. Fan, H. K. M. Vithana, and A. Z. Genack, "Low-threshold lasing at the edge of a photonic stop band in cholesteric liquid crystals", Optics Express 23 , 1707–1709 (1998)

21. K. Dolgaleva, S. K. H. Wei, S. G. Lukishova, S. H. Chen, K. Schwertz and R. W. Boyd "Enhanced laser performance of cholesteric liquid crystals doped with oligofluorene dye", Journal of the Optical Society of America, 25, 1496–1504, (2008)

22. N.V. Kukhtarev, "Cholesteric liquid crystal laser with distributed feedback". Soviet Journal of Quantum Electronics, 8, 774 (1978)

23. I.P. Ilchishin, E.A. Tikhonov, V.G. Tishchenko, and M.T. Shpak, "Generation of a tunable radiation by impurity cholesteric liquid crystals", Journal of Experimental

and Theoretical Physics Letters, 32, 24–27 (1980)

24. Figure from the Centre of Molecular Materials for Photonics and Electronics (CMMPE), University of Cambridge,
UK. http://www-g.eng.cam.ac.uk/CMMPE/lcintro2.html

25. Liquid Crystal Art Gallery:
http://www.mc2.chalmers.se/pl/lc/engelska/gallery/platelet.html

26. V.G. Chigrinov, “Liquid Crystal Devices: Physics and Applications”, Artech House Optoelectronics Library (1999)

27. S. Faetti, M. Gatti, V. Palleschi, and T. J. Sluckin, “Almost Critical Behavior of the Anchoring Energy at the Interface between a Nematic Liquid Crystal and a SiO Substrate”, Phys. Rev. Lett. 55, 1681 (1985)

28. H. Yokoyama and H. A. van Sprang, “A novel method for determining the anchoring energy function at a nematic liquid crystal-wall interface from director distortions at high fields”, J. Appl. Phys.,57, 4520 (1985)

29. S. M. Kelly and M. O’Neill, “LIQUID CRYSTALS FOR ELECTRO-OPTIC APPLICATIONS”, Handbook of Advanced Electronic and Photonic Materials and Devices, Volume 7: Liquid Crystals, Display and Laser Materials (2000)

30. D.K. Yang and S.T. Wu, “Fundamentals of Liquid Crystal Devices”, Wiley, NJ, (2006)

31. E. Hecht, “Optics”, 4th edition, , Addison Wesley (2002)

32. P. G. de Gennes and J. Prost, “the physics of liquid crystals”, Oxford University Press, New York (1993)

33. S. Chandrasekhar, “Liquid Crystals”, 2nd edition, Cambridge University Press, New York (1997)

34. A. Strigazzi, “Freedericksz transition”, Chapter X in “liquid crystal materials”, editor I.C.Khoo, Gordon and Breach, Amsterdam, (1991)

35. Figure is from Institut für Theoretische Physik, TU Berlin http://wwwitp.physik.tu-berlin.de/muschik/liquid_crystals/lc_intro.html

36. http://www.lci.kent.edu/boslab/modeling/index.html

37. P. A. Franken, A. E. Hill, C. W. Peters, and G. Weinreich, “Generation of Optical Harmonics”, Phys. Rev. Lett. 7, 118, (1961)

38. G. P. Agrawal, “Nonlinear fiber optics: its history and recent progress”, J. Opt. Soc. Am. B, 28, A1–A10 (2011)

39. J. C. Travers, W. Chang, J. Nold, N. Y. Joly, and P. St. J. Russell, “Ultrafast nonlinear optics in gas-filled hollow-core photonic crystal fibers”, J. Opt. Soc. Am. B, 28, A11–A26 (2011)

40. O. A. Aktsipetrov, “Surface nonlinear optics and nonlinear magneto-optics at Moscow State University”, J. Opt. Soc. Am. B, 28, A27–A37 (2011)

41. R. W. Boyd, “Material slow light and structural slow light: similarities and differences for nonlinear optics”, J. Opt. Soc. Am. B, 28, A38–A44 (2011)

42. I. C. Khoo, “Extreme nonlinear optics of nematic liquid crystals”, J. Opt. Soc. Am. B, 28, A45–A55 (2011)

43. Y. R. Shen, “Surface nonlinear optics”, J. Opt. Soc. Am. B, 28, A56–A66 (2011)

44. L. Caspani, D. Duchesne, K. Dolgaleva, S. J. Wagner, M. Ferrera, L. Razzari, A. Pasquazi, M. Peccianti, D. J. Moss, J. S. Aitchison, and R. Morandotti, “Optical frequency conversion in integrated devices”, J. Opt. Soc. Am. B, 28, A67–A82 (2011)

45. A. Yariv, “The beginning of quantum nonlinear optics”, J. Opt. Soc. Am. B, 28, A83–A87 (2011)

46. I. C. Khoo, “Nonlinear optics of liquid crystalline materials,” Phys. Rep. 471, 221–267 (2009)

47. I. C. Khoo, “Optically induced molecular reorientation and third order nonlinear optical processes in nematic liquid crystals,” Phys. Rev. A 23, 2077–2081 (1981)

48. I. C. Khoo, “Re-examination of the theory and experimental results of optically induced molecular reorientation and nonlinear diffractions in nematic liquid crystals: spatial frequency and temperature dependence,” Phys. Rev. A 27, 2747–2750 (1983)

49. I. C. Khoo and R. Normandin, “The mechanism and dynamics of transient thermal grating diffraction in nematic liquid crystal films,” IEEE J. Quantum Electron. 21, 329–335 (1985)

50. I. C. Khoo, H. Li, and Y. Liang, “Observation of orientational photorefractive effects in nematic liquid crystals,” Opt. Lett. 19, 1723–1725 (1994).

51. I. C. Khoo, M. V. Wood, M. Y. Shih, and P. H. Chen, “Extremely nonlinear photosensitive liquid crystals for image sensing and sensor protection,” Opt. Express 4, 432–442 (1999)

52. I. C. Khoo, J. H. Park, and J. D. Liou, “Theory and experimental studies of all-optical transmission switching in a twist-alignment dye-doped nematic liquid crystal,” J. Opt. Soc. Am. B 25, 1931–1937 (2008)

53. I. C. Khoo and J. Ding, “All-optical cw laser polarization conversion at 1.55 micron by two beam coupling in nematic liquid crystal film,” Appl. Phys. Lett. 81, 2496–2498 (2002)

54. I. C. Khoo, J. Ding, Y. Zhang, K. Chen, and A. Diaz, “Supra nonlinear photorefractive response of single-wall carbon nanotube- and C60-doped nematic liquid crystals,” Appl. Phys. Lett. 82, 3587–3589 (2003)

55. I. C. Khoo, D. H. Werner, X. Liang, A. Diaz, and B. Weiner, “Nanosphere dispersed liquid crystals for tunable negative-zeropositive index of refraction in the optical and Terahertz regimes,” Opt. Lett. 31, 2592–2594 (2006)

56. I. C. Khoo, A. Diaz, J. Liou, D. Werner, J.H. Park, Y. Ma, J. Huang, “Liquid Crystal Nonlinear Optical Meta-Materials”, Molecular Crystals and Liquid Crystals, v 502, p 109-120 (2009)

57. I.C. Khoo, A. Diaz, J. Liou, M. Stinger, J. Huang, Y. Ma, “Extremely nonlinear nano-dispersed organic liquids for multiple time scale passive optical switching applications”, LEOS 2009 -22nd Annuall Meeting of the IEEE Lasers and Electro-Optics Society, p 391-2, (2009)

58. I.C. Khoo, J. Huang, J. Liou, Y. Ma, S. Zhao, “Liquid crystals nonlinear optics CW to femtoseconds all-optical signal processing”, Conference on Lasers and

Electro-Optics: Laser Science to Photonic Applications, (2011)

59. I. C. Khoo, A. Diaz, J. Liou, M. V. Stinger, J. Huang, and Y. Ma, “Liquid crystals tunable optical metamaterials,” IEEE J. Sel. Top. Quantum Electron. 16, 410–417 (2010)

60. R. W. Boyd, “Nonlinear Optics”, Third Edition, Academic Press, (2008)

61. R. del Coso and J. Solis “Relation between nonlinear refractive index and third-order susceptibility in absorbing media” J. Opt. Soc. Am. B, 21, (2004)

62. J.R. Sambles, G.W. Bradbery, F. Yang, “Optical excitation of surface plasmons: an introduction”, Contemporary Physics, 32, p 173-83 (1991)

63. S. A. Maier and H,A. Atwater, “Plasmonics: Localization and guiding of electromagnetic energy in metal/dielectric”, Journal of Applied Physics, 98, 011101 (2005)

64. R. W. Wood, “On a remarkable case of uneven distribution of light in a diffraction grating spectrum” Proc Phys Soc. 18,269, (1902)

65. G. Mie, “Beitrage zur Optik truber Medien, speziell kolloidaler Metallosungen”, Ann Phys. ,330, 377–445, (1908)

66. J. Zenneck, “Uber die Fortpflanzung ebener electromagnetische Wellen langs einer ebenen Leiterflche und ihre Beziehung zur drachtlosen Telegraphie”, Ann der Physik, 23, 846–866 (1907)

67. A. Sommerfeld, “Uber die Ausbreitlung derWellen in der drahtlosen Telegraphie”, Ann der Physik, 507, 665–736 (1909)

68. U. Fano, “The Theory of Anomalous Diffraction Gratings and of Quasi-Stationary Waves on Metallic Surfaces (Sommerfeld’ s Waves)”, J Opt Soc Am. 31, 213–222 (1941)

69. R. H. Ritchie, “Plasma losses by fast electrons in thin films”, Phys Rev., 106, 874–881 (1957)

70. E. A. Stern. , Bull Am Phys Soc. 4, 235 (1959)

71. E. A. Stern, R. A. Ferrell, “Surface plasma oscillations of a degenerate electron gas”, Phys Rev. 120, 130–136 (1960)

72. C. J. Powell, J. B. Swan, “Effect of oxidation on the characteristic loss spectra of aluminum and magnesium”, Phys Rev. ,118, 640–643 (1960)

73. A. Otto, “Excitation of nonradiative surface plasma waves in silver by the method of frustrated total reflection”, Z Phys. 216, 398–410 (1968)

74. E. Kretschmann, H. Raether, “Radiative decay of non-radiative surface plasmons excited by light”, Z Naturf. 23A, 2135–2135 (1968)

75. T. W. Ebbesen, H. J. Lezec, H. F. Ghaemi, T. Thio, P. A. Wolff, “Extaordinary optical transmission through sub-wavelength holes”, Nature, 391, 667–669 (1998)

76. Y. Sun and Y. Xia, “Shape-Controlled Synthesis of Gold and Silver Nanoparticles”, Science, 76,298 (2002)

77. Nicholas Fang, HyesogLee, Cheng Sun, XiangZhang, “Sub–Diffraction-Limited Optical Imaging with a Silver Superlens”, Science, 308, 534 (2005)

78. O. J. F. Martin, B. Hecht, “Resonant optical antennas”, Science, 308, 1607 (2005)

79. S. I. Bozhevolnyi, V. S. Volkov, E. Devaux, J. Y. Laluet and T. W. Ebbesen, “Channel plasmon subwavelength waveguide components including interferometers and ring resonators”, Nature, 440, 508-511 (2006)

80. Z. Liu, H. Lee, Y. Xiong, C. Sun and X. Zhang, “Far-Field Optical Hyperlens Magnifying Sub-Diffraction-Limited Objects”, Science, 315, 1686 (2007)

81. P. Zijlstra, J. W. M. Chon & M. Gu, “Five-dimensional optical recording mediated by surface plasmons in gold nanorods”, Nature 459, 410-413 (2009)

82. M. A. Noginov, G. Zhu, A. M. Belgrave, R. Bakker, V. M. Shalaev, E. E. Narimanov, S. Stout, E. Herz, T. Suteewong & U. Wiesner, “Demonstration of a spaser-based nanolaser”, Nature 460, 1110-1112 (2009)

83. R. F. Oulton, V. J. Sorger, T. Zentgraf, R. Ma, C. Gladden, L. Dai, G. Bartal & X. Zhang, “Plasmon lasers at deep subwavelength scale”, Nature 461, 629-632 (2009)

84. C. Kittel, “Introduction to solid state physics”, Chapter 10, Eighth Edition, (2004)

85. H. Raether, “Surface plasmonson smooth and rough surfaces and on gratings”, Chapter 2, (1988)

86. W. L. Barnes, A. Dereux and T. W. Ebbesen, “Surface plasmon subwavelength optics”，Nature, 424, 824-830 (2003)

87. A.V. Zayats, I.I. Smolyaninov, A.A. Maradudin, “Nano-optics of surface plasmon polaritons”, Physics Reports 408, 131–314 (2005)

88. S. Lal, S. Link, N. J. Halas, “Nano-optics from sensing to waveguiding”, Nature photonics, 1, 641 (2007)

89. K. T. Carron, W. Fluhr, M. Meier, A. Wokaun, H. W. Lehmann, “Resonances of twodimensional particle gratings in surface-enhanced Raman scattering”, J Opt Soc Am B., 3, 430–440 (1986)

90. S. Zou, N. Janel, G. C. Schatz, “Silver nanoparticle array structures that produce remarkably narrow plasmon lineshapes”, J Chem Phys. 120, 10871–10875 (2004)

91. S. Zou, G. C. Schatz, “Narrow plasmonic/hotonic extinction and scattering line shapes for one and two dimensional silver nanoparticle arrays”, J Chem Phys. 121,12606–12612 (2004)

92. V. A. Markel, “Divergence of dipole sums and the nature of non-Lorentzian exponentially narrow resonances in one-dimensional periodic arrays of nanospheres”, J Phys B. ,38, 115–121 (2005)

93. B. Auguie, W. L. Barnes, “Collective resonances in gold nanoparticle arrays”, Phys Rev Lett., 101, 143902 (2008)

94. S. Zou, G. C. Schatz, “Theoretical studies of plasmonresonances in one-dimensional nanoparticle chains: narrow lineshapes with tunable widths”, Nanotechnology, 17,2813 (2006)

95. B. T. Draine, P.J. Flatau, “Discrete-dipole approximation for scattering calculations”, J. Opt. Soc. Am. A，11，1491 (1994)

96. B.J. Wiley , Y. Chen, J.M. McLellan , Y. Xiong Y, Z.Y. Li , D. Ginger, Y. Xia, “Synthesis and Optical Properties of Silver Nanobar sand Nanorice”，NanoLett，7,1032 (2007)

97. M. I. Mishchenko, L. A. Travis, A. A. Lacis, “Scattering, Absorption, and Emission of light by small particles”, Cambridge University Press (2002)

98. O. J. F. Martin, C. Girard, A. Dereux, “Generalized field propagator for electromagnetic scattering and light confinement”, Phys. Rev. Lett. 74, 526 (1995)

99. K. S. Yee, “Numerical solution of initial boundary value problems involving maxwell’s equations in isotropic media” IEEE Trans Antennas Propagat. AP-14, 302 (1966)

100. K. S. Kunz, R. J. Luebbers, “Finite difference time domain method for electromagnetics”, CRC- press, (1993)

101. XFDTD: http://www.remcom.com/xf7

102. FDTD Solutions: http://www.lumerical.com/tcad-products/fdtd/

103. M. S. Wheeler, J. S. Aitchison, and M. Mojahedi, “Three-dimensional array of dielectric spheres with an isotropic negative permeability at infrared frequencies,” Physical Review B 72,193103 (2005)

104. J. D. Jackson, “Classical Electrodynamics”, 3rd ed. Wiley, New York, (1999)

105. M. S. Wheeler, J. S. Aitchison, and M. Mojahedi, “Coated nonmagnetic spheres with a negative index of refraction at infrared frequencies”, Phys.Rev. B 73, 045105 (2006)

106. R. Brendel and D. Bormann, “An infrared dielectric function model for amorphous solids,” J. Appl. Phys. 71, 1–6 (1992)

107. A. D. Rakic, A. B. Djurisic, J. M. Elazar and M. L. Majewski, “Optical properties of metallic films for vertical-cavity optoelectronic devices”, Applied Optics 37, 5271–5283 (1998)

108. A. Diaz, S. Kubo, Y. Tang, J. Liou, T. S. Mayer, I. C. Khoo, and T. E. Mallouk, "Tunable refractive index materials with metallic nano-spheres dispersed in organic liquids," Proc. SPIE 6654(Liquid Crystals XI), 1-66540V/8 (2007)

109. U. Kreibig, "Kramers Kronig Analysis of Optical Properties of Small Silver Particles," Zeitschrift Fur Physik 234, 307 (1970)

110. H. Hovel, S. Fritz, A. Hilger, U. Kreibig, and M. Vollmer, "Width of cluster plasmon resonances: Bulk dielectric functions and chemical interface damping," Physical Review B, 48, 18178 - 18188 (1993)

111. A. Diaz, J. H. Park and I. C. Khoo, “Design and transmission-reflection properties of liquid crystalline optical Metamaterials with large birefringence and sub-unity or negative-refractive index”, Journal of Nonlinear Optical Phys. & Mat., vol.16, 533-549 (2007)

112. R.M. Walser, in: W.S. Weiglhofer and A. Lakhtakia (Eds.), “Introduction to Complex Mediums for Electromagnetics and Optics”, SPIE Press, Bellingham, WA, USA (2003)

113. I. C. Khoo, S. Webster, S. Kubo, W. J. Youngblood, J. D. Liou, T. E. Mallouk, P. Lin, D. J. Haganb, E. W. V. Stryland, “Synthesis and characterization of the multi-photon absorption and excited state properties of a neat liquid 4-propyl 40-butyl diphenyl acetylene”, J. Mater. Chem., 19, 7525–7531 (2009)

114. I. C. Khoo, J. Huang, S. Zhou, J. Liou, K. L. Hong, Y. Ma, “Liquid-crystals-plasmonics for ultrafast broadband all-optical switching”, Mater. Res. Soc. Symp. Proc., 1293, (2011)

115. J. E. Sipe, R. W. Boyd, “Nonlinear susceptibility of composite optical materials in the Maxwell Garnett model”, Phys. Rev. A., 46, 1614 (1992)

116. E. W. V. Stryland, M. Sheik-Bahae, “Z-Scan Measurements of Optical Nonlinearities”, Characterization Techniques and Tabulations for Organic Nonlinear Materials, M. G. Kuzyk and C. W. Dirk, Eds., 655-692, Marcel Dekker, Inc., (1998)

117. D. C. Kohlgraf-Owens, P. G. Kik, “Numerical study of surface plasmon enhanced nonlinear absorption and refraction” Opt. Exp., 16, 16823 (2008)

118. J. Muller, C. Sonnichsen, H. von Poschinger, G. von Plessen, T. A. Klar and J. Feldmann, “Electrically controlled light scatterring with single metal nanoparticles”, Appl. Phys. Lett., 81, 171-173 (2002)

119. S.Y. Park, D. Stroud, “Splitting of surface plasmon frequencies of metal particles in a nematic liquid crystal” Appl. Phys. Lett. vol.85, 2920 (2004)

120. P. A. Kossyrev, A. Yin, S. G. Cloutier, and D. A. Cardimona, “Electric Field Tuning of Plasmonic Response of Nanodot Array in Liquid Crystal Matrix” Nano Lett., 5, 1978. (2005)

121. K. C. Chu, C. Y. Chao, Y. F. Chen, Y. C. Wu and C. C. Chen, “Electrically controlled surface plasmon resonance frequency of gold nanorods” Appl. Phys. Lett. 89, 103107 (2006)

122. V. Hsiao, Y. Zheng, B. Juluri, and T. Huang, “Light-Driven Plasmonic Switches Based on Au Nanodisk Arrays and Photoresponsive Liquid Crystals” AdV. Mater., 20, 3528 (2008)

123. L. Gunnarsson, T. Rindzevicius, J. Prikulis, B. Kasemo, M. Ka¨ll, S. Zou and G. C. Schatz, “Confined Plasmons in Nanofabricated Single Silver Particle Pairs: Experimental Observations of Strong Interparticle Interactions” J. Phys. Chem. B, 109, 1079 (2005)

124. L. Wang, Y. Nishijima, K. Ueno, H. Misawa and N. Tamai, “Near-IR vibrational dynamics of periodic gold single and pair nanocuboids” Appl. Phys. Lett. 95, 053116 (2009)

125. A. Dhawan, S. J. Norton, M. D. Gerhold and T. Vo-Dinh, “Comparison of FDTD numerical computations and analytical multipole expansion method for plasmonics-active nanosphere dimers” Opt. Exp.,17,9688 (2009)

126. P. K. Jain, M. A, El-Sayed, “Noble Metal Nanoparticle Pairs: Effect of

Medium for Enhanced Nanosensing" Nano Lett.,8,4347 (2008)

127. C. Pecharromán, J. Pérez-Juste, G. Mata-Osoro,L. M. Liz-Marzán, and P. Mulvaney, "Redshift of surface plasmon modes of small gold rods due to their atomic roughness and end-cap geometry" Phys. Rev. B 77, 035418 (2008)

128. K.S. Lee, M. A, El-Sayed, "Dependence of the Enhanced Optical Scattering Efficiency Relative to That of Absorption for Gold Metal Nanorods on Aspect Ratio, Size, End-Cap Shape, and Medium Refractive Index" J. Phys. Chem. B, 109, 20331 (2005)

129. M. Dridi, A. Vial, "Modeling of metallic nanostructures embedded in liquid crystals: application to the tuning of their plasmon resonance" Opt. Lett., 34, 2652 (2009)

130. M. Dridi, A. Vial, "FDTD Modeling of Gold Nanoparticles in a Nematic Liquid Crystal: Quantitative and Qualitative Analysis of the Spectral Tunability" J. Phys. Chem. C ,114, 9541 (2010)

131. E. E. Kriezis , S. J. Elston, "Finite-difference time domain method for light wave propagation within liquid crystal devices" Opt. Comm., 165,99 (1999)

132. H. Gai, J. Wang, and Q. Tian, "Modified Debye model parameters of metals applicable for broadband calculations." Appl. Opt., 46, 2229 (2007)

133. I. Romero, J. Aizpurua, G. W. Bryant and F. J. García de Abaj, "Plasmons in nearly touching metallic nanoparticles: singular response in the limit of touching dimers" Opt. Exp.14, 9988 (2006)

134. A. M. Funston, C. Novo, T. J. Davis and P. Mulvaney, "Plasmon Coupling of Gold Nanorods at Short Distances and in Different Geometries" Nano Lett 9.1651 (2009)

135. J. Aizpurua, G. W. Bryant, L. J. Richter, F. J. Garcia de Abajo, B. K. Kelley, and T. Mallouk, "Optical properties of coupled metallic nanorods for field-enhanced spectroscopy" Phys. Rev. B 71, 235420, (2005)

136. J. Smalley, Y. Zhao, A. Nawaz, Q. Hao, Y. Ma, I.C. Khoo, T. Huang, “High contrast modulation of plasmonic signals using nanoscale dual-frequency liquid crystals”, Optics Express, 19, 15265-15274 (2011)

137. Y. Zhao, Q. Hao, Y. Ma, M. Lu, B. Zhang, M. Lapsley, I.C. Khoo, T. Huang, “Light-driven tunable dual-band plasmonic absorber using liquid-crystal-coated asymmetric nanodisk array ”, Applied Physics Letters, 100, 053119 (2012)

138. J. Li, Y. Ma, Y. Gu, I.C. Khoo, Q. Gong, “Large spectral tunability of narrow geometric resonances of periodic arrays of metallic nanoparticles in a nematic liquid crystal”, Applied Physics Letters, 98, 213101 (2011)

139. Y. Liu, Q. Hao, J. Smalley, J. Liou, I. Khoo, and T. Huang, “A frequency-addressed plasmonic switch using dual-frequency liquid crystals,” Appl. Phys. Lett. 97, 9 (2010)

140. Q. Hao, Y. Zhao, B. K. Juluri, B. Kiraly, J. Liou, I. C. Khoo, and T. J. Huang, “Frequency-addressed tunable transmission in optically thin metallic nanohole arrays with dual-frequency liquid crystals,” J. Appl. Phys. 109, 084340 (2011)

141. B. Zhang, Y. Zhao, Q. Hao, B. Kiraly, I. Khoo, S. Chen, and T. J. Huang, “Polarization-independent dual-band infrared perfect absorber based on a metal-dielectric-metal elliptical nanodisk array”, Opt. Express 19, 15221 (2011)

142. Y. Chu, E. Schonbrun, T. Yang, K. B. Croziera, “Experimental observation of narrow surface plasmon resonances in gold nanoparticle arrays”, Appl. Phys. Lett., 93, 181108 (2008)

VITA

Yi Ma

Yi Ma was born in Beijing, People's Republic of China in 1984. He received his B.S. degree in Electronics from Peking University in 2006. Then he began his study in the Department of Electrical Engineering at Pennsylvania State University. In 2008, he completed his M.S. degree in Electrical Engineering at Pennsylvania State University and enrolled in the Ph.D. program in the same department. He worked as a Research Assistant under the direction of Dr. Iam-Choon Khoo in the laboratory of Liquid Crystals and Nonlinear Optics Lab. He is a member of Institute of Electrical and Electronics Engineers (IEEE), Optical Society of America (OSA), International society of for Optical Engineering (SPIE) and Golden Key International Honor Society.